INFRARED OPTICAL STUDIES OF HgTe-CdTe SUPERLATTICES AND GaAs

Thesis by

Steven Robert Hetzler

In Partial Fulfillment of the Requirements

for the Degree of

Doctor of Philosophy

California Institute of Technology

Pasadena, California

1986

(Submitted October 28, 1985)

To Roselynn

Acknowledgments

I would like to thank Dr. T. C. McGill for his support and assitance during my years of graduate study at Caltech. It has been both a pleasure and a privilege to work with him.

I am indebted to Dr. A. T. Hunter of the Hughes Research Laboratories for his continuing help on my various projects, and for setting a high standard of experimental excellence. I have also profited from my many interactions with Dr. D. L. Smith of the Los Alamos National Laboratories.

I owe a special debt of gratitude to O. J. Marsh, J. P. Baukus, R. Baron and M. H. Young of the Semiconductor Crystal Physics Group at the Hughes Research Laboratories for making their FTIR available for the experiment in Chapter 2 and for providing the GaAs samples used for Chapter 3. I would especially like to thank A. T. Hunter and J. P. Baukus for their ingenuity in helping devise the FTIR experiment described in Appendix A. I would also like to thank Dr. J. P. Faurie of the University of Illinois and Dr. P. P. Chow of Honeywell for providing the HgTe-CdTe superlattice samples for the study in Chapter 2.

I have also profited from many discussions with Drs. C. Mailhoit, R. M. Feenstra, A. Zur and R. T. Collins, as well as with R. J. Hauenstein, G. Y. Wu, T. E. Schlesinger, M. B. Johnson and R. H. Miles. I would also like to express my thanks to Vere Snell, for her excellent secretarial work, and her always cheerful disposition.

I would like to thank the following for financial support: the California Institute of Technology, International Business Machines corporation, the Army Research Office and the Office of Naval Research.

Above all, I am grateful to my wife, Roselynn Hươ̄ng, for her patience, support and encouragement during my years of graduate study.

Abstract

This thesis presents two different studies of the infrared optical properties of two different semiconductors. Chapter 2 describes the results of the first infrared photoluminescence (IRPL) measurements of a HgTe-CdTe superlattice. IRPL spectra of two different HgTe-CdTe superlattices from two different sources were measured from 100 to 270 K. Sample 1 was grown on (111) $Cd_{0.96}Zn_{0.04}Te$, and was grown to have 250 repeats of 38 – 40 Å of HgTe followed by 18 – 20 Å of CdTe. Sample 2 was grown on (111) CdTe and was grown to have 75 repeats of 50 Å of HgTe followed by 50 Å of CdTe. Sample 1 exhibited a single asymmetrical luminescence line at all temperatures studied. (Low signal-to-noise ratio from sample 2 prevented detailed analysis of the lineshape.) The luminescence from both samples occured at significantly lower energies than that from $Hg_{1-x}Cd_xTe$ alloys with the same Cd concentrations as the average Cd concentrations of the superlattices. At 240 K, the luminescence peak from sample 1 was near 148 meV, with a full width at half-maximum intensity of 42 meV, while the peak from sample 2 was near 242 meV, with a full width at half-maximum intensity of 69 meV. Analysis of the luminescence lineshape from sample 1 showed it to be consistent with wave-vector conserving band-to-band recombination. In this case, the band-gap energy of the superlattice would be near the low energy threshold of the luminescence peak. This study therefore represents the first direct determination of the band gap of an HgTe-CdTe superlattice. A comparison of the lineshapes from both samples with those measured in GaAs-$Ga_{1-x}Al_xAs$ superlattices showed evidence for fluctuations in the layer thicknesses of both the HgTe-CdTe superlattice samples. A comparison was made between the data and a simple theory of the band gaps of HgTe-CdTe superlattices. The theory was shown to be consistent with the experiments, if there were small errors in the measurements of the superlattice layer thicknesses of each sample. The differences in the luminescence properties of the two samples show that it is possible to tailor the band gaps of HgTe-CdTe superlattices.

Chapter 3 describes the first observation of *s*-like excited states of a double acceptor in a semiconductor. Two experiments were performed to study the *s*-like excited states of the 78-meV acceptor in GaAs. The techniques used, selective excitation scattering (SEL) and electronic Raman scattering (ERS), are both sensitive to the detection of *s*-like excited states of single acceptors in semiconductors. Measurements on two different liquid encapsulated Czochralski GaAs samples showed two *s*-like excited state transitions of equal magnitude, separated by 4.0 meV. Only one *s*-like transition is expected in the energy range measured for a single acceptor. A simple effective mass-like model of a double acceptor was developed to account for the two *s*-like excited states. This model predicted a splitting of the $1s^1 2s^1$ excited state of a double acceptor to be 2.6 meV, in good agreement with the observed value of 4.0 meV. This proved that the 78-meV acceptor in GaAs is due to the first ionization of a double acceptor, the first such identification to be made based on the *s*-like excited state spectrum. It is therefore possible to identify the valency of an acceptor in a semiconductor by measuring the *s*-like excited state spectrum.

Appendix A describes a novel technique for performing infrared photoluminescence measurements using a Fourier transform infrared spectrophotometer. This technique was developed to perform the experiments described in Chapter 2.

Parts of this thesis have been or will be published under the following titles:

Chapter 2:

Infrared Photoluminescence Spectra from HgTe-CdTe Superlattices,

S. R. Hetzler, J. P. Baukus, A. T. Hunter, J. P. Faurie, P. P. Chow and T. C. McGill, *Applied Physics Letters* **47**, 260 (1985).

Infrared Photoluminescence Measurments of a HgTe-CdTe Superlattice,

S. R. Hetzler, T. C. McGill, J. P. Baukus, A. T. Hunter and J. P. Faurie, presented at the *1985 Electronic Materials Conference*, Boulder, June 19–21, 1985.

Infrared Photoluminescence Spectra from HgTe-CdTe Superlattices,

S. R. Hetzler, J. P. Baukus, A. T. Hunter, J. P. Faurie, P. P. Chow and T. C. McGill, presented at the *Yamada (2nd International) Conference on Modulated Semiconductor Structures*, Kyoto, Japan, September, 1985.

Experimental and Theoretical Comparison of Optical Properties of HgTe-CdTe Superlattices,

J. P. Baukus, A. T. Hunter, C. Jones, G. Y. Wu, S. R. Hetzler, T. C. McGill and J. P. Faurie, to be presented at the *1985 U.S. Workshop on the Physics and Chemistry of Mercury Cadmium Telluride*, San Diego, October 8–10, 1985, and to be published in the *Journal of Vacuum Science and Technology*, July/August, 1986.

Chapter 3:

S-like Excited States of the 78-meV Acceptor in GaAs,

S. R. Hetzler, T. C. Mcgill and A. T. Hunter, *Proceedings of the 17th International Conference on the Physics of Semiconductors*, San Francisco, August 6–10, 1984.

Selective Excitation Luminescence and Electronic Raman Scattering Study of the 78-meV Acceptor in GaAs,

S. R. Hetzler, T. C. McGill and A. T. Hunter, *Applied Physics Letters* **44**, 793 (1984).

Selective Excitation Luminescence and Electronic Raman Scattering Study of the 78-meV Acceptor in GaAs,

S. R. Hetzler, T. C. McGill and A. T. Hunter, *Bulletin of the American Physical Society* **29**, 290 (1984).

Contents

List of Figures

List of Tables

Chapter 1

Introduction

1.1 Background

This thesis deals with infrared optical studies of semiconductors. The interest in optical studies of semiconductors stems from the desire to understand both the optical and electrical behavior of such materials. Semiconductors are useful for fabricating both electrical and optical devices. An understanding of the properties of such materials, and how to control them, is necessary for the successful design of useful devices. One of the studies in this thesis involves determining the basic intrinsic properties of a new material, the HgTe-CdTe superlattice, which, it is hoped, will be useful for fabricating infrared detectors. (The intrinsic properties are defined here to be those material properties which are basic to the ideal material, such as the band structure, lattice constant, effective masses and phonon frequencies.) The other study involves extrinsic properties of GaAs, a material used for the fabrication of high-speed devices. (The extrinsic properties are defined to be those properties which arise from non-ideality, such as the presence of impurities, defects, and the crystal quality, all of which can be influenced by external factors.) Optical studies are useful for these studies since they can provide a wide variety of information about both the intrinsic and extrinsic properties of semiconductors, and do not involve contacting the material.

The majority of infrared detectors today are based upon semiconductors as the light-sensitive elements. In order to successfully fabricate a detector, it is important to understand how the material interacts with light. This interaction can be affected not only by the intrinsic properties of the material, but by extrinsic factors as well, such as the presence of impurities. Much effort has been spent in trying improve the performance of infrared detectors by controling the extrinsic properties of materials used, since most materials have few adjustable intrinsic parameters. Alloy semiconductors, such as $Hg_{1-x}Cd_xTe$, are extensively used since it is possible to tailor the band gap of these materials (an intrinsic property) by varying the concentrations of the constituents. However, once the desired band gap is chosen, the only remaining adjustable parameters are extrinsic. Recently it has become possible to tailor the intrinsic properties of semiconductors by controlling the structure of the material at near inter-atomic dimensions. This has opened up a whole new field of materials characterization, since the properties of many of these structures have only been investigated theoretically. Optical studies, such as photoluminescence, can provide useful information on the important intrinsic properties of these materials, such as determining the band-gap energies.

Most semiconductor devices are fabricated by doping selective regions of material on an insulating substrate to isolate the various regions. The production of devices using certain materials is limited by the availablility of suitable substrate material. It is important for the substrate to remain insulating during the entire fabrication process. This requires good control of the electrical properties of the substrate. For most semiconductor materials, it is the impurities that determine the electrical properties. Therefore it is important to understand how impurities behave in the material, and the mechanisms for their introduction into the material. Optical studies provide a means for both identifying and studying the behavior of impurities in semiconductors.

1.2 Superlattices

Recently it has become possible to fabricate layered semiconductor materials whose structure is controlled at near interatomic dimensions. Such structures can have properties which differ dramatically from those of bulk materials. One such structure, first proposed by Esaki and Tsu in 1969,[1] is composed of a series of alternating thin layers of two different materials. Such a structure is called a superlattice, since the period of the lattice along the direction normal to the plane of layers is many atomic spacings long. Figure 1.1 shows the general structure of a superlattice. The substrate is usually bulk material of one of the constituents, although alternate materials are sometimes used. The superlattice layers may be grown by a number of techniques, with molecular beam epitaxy (MBE) and metalorganic chemical vapor deposition (MOCVD) being the most prevalent techniques. Both of these methods grow superlattices by depositing a number of monolayers of each material onto a substrate. A buffer layer of one of the materials is sometimes grown before the superlattice, usually to guarantee a high quality surface for growing the superlattice. The layer thicknesses are typically anywhere from 20 – 500 Å.

Figure 1.2 shows the spatial dependence of the constituent material band edges for three different types of superlattices.[2] In each case, the upper line represents the energy of the conduction band minimum as a function of position, and the lower line represents the energy of the valence band maximum. The different superlattice types reflect the differences in the relative alignments of

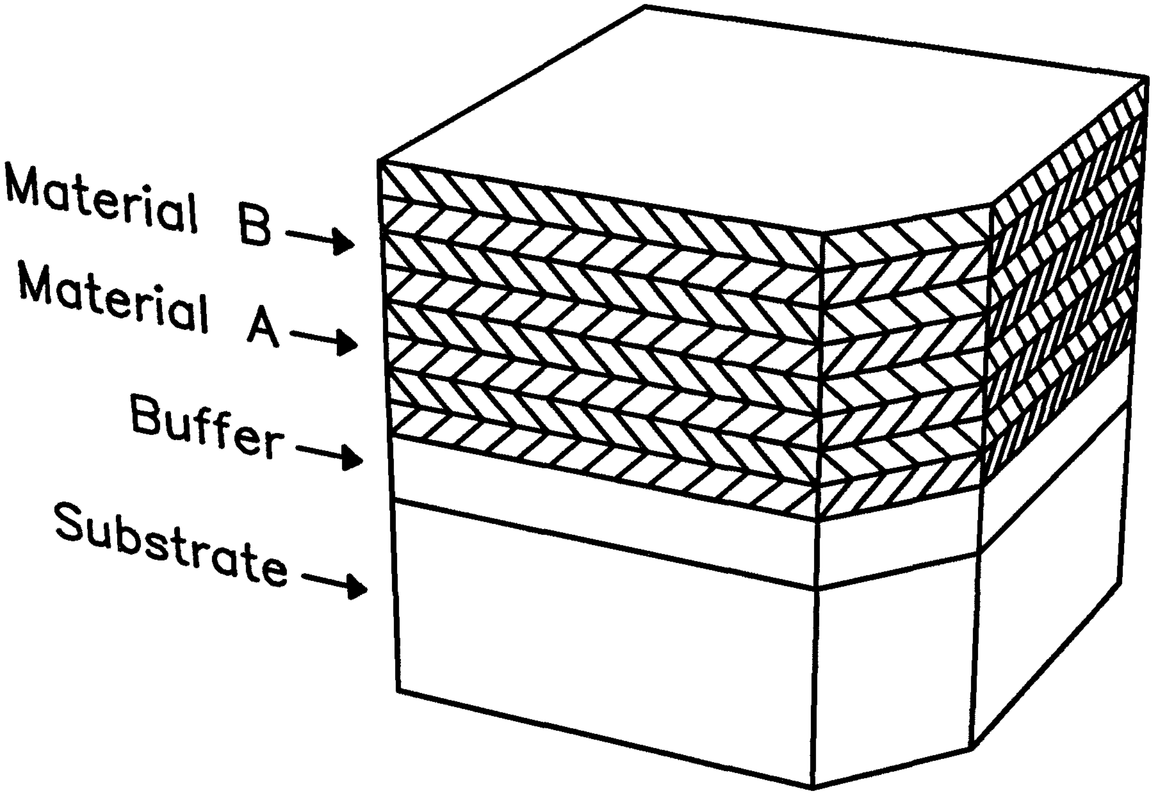

Figure 1.1: Structure of a semiconductor superlattice. The superlattice itself is composed of alternating thin layers of two different semiconductor materials. The layer thicknesses are typically in the range of 20 – 500 Å.

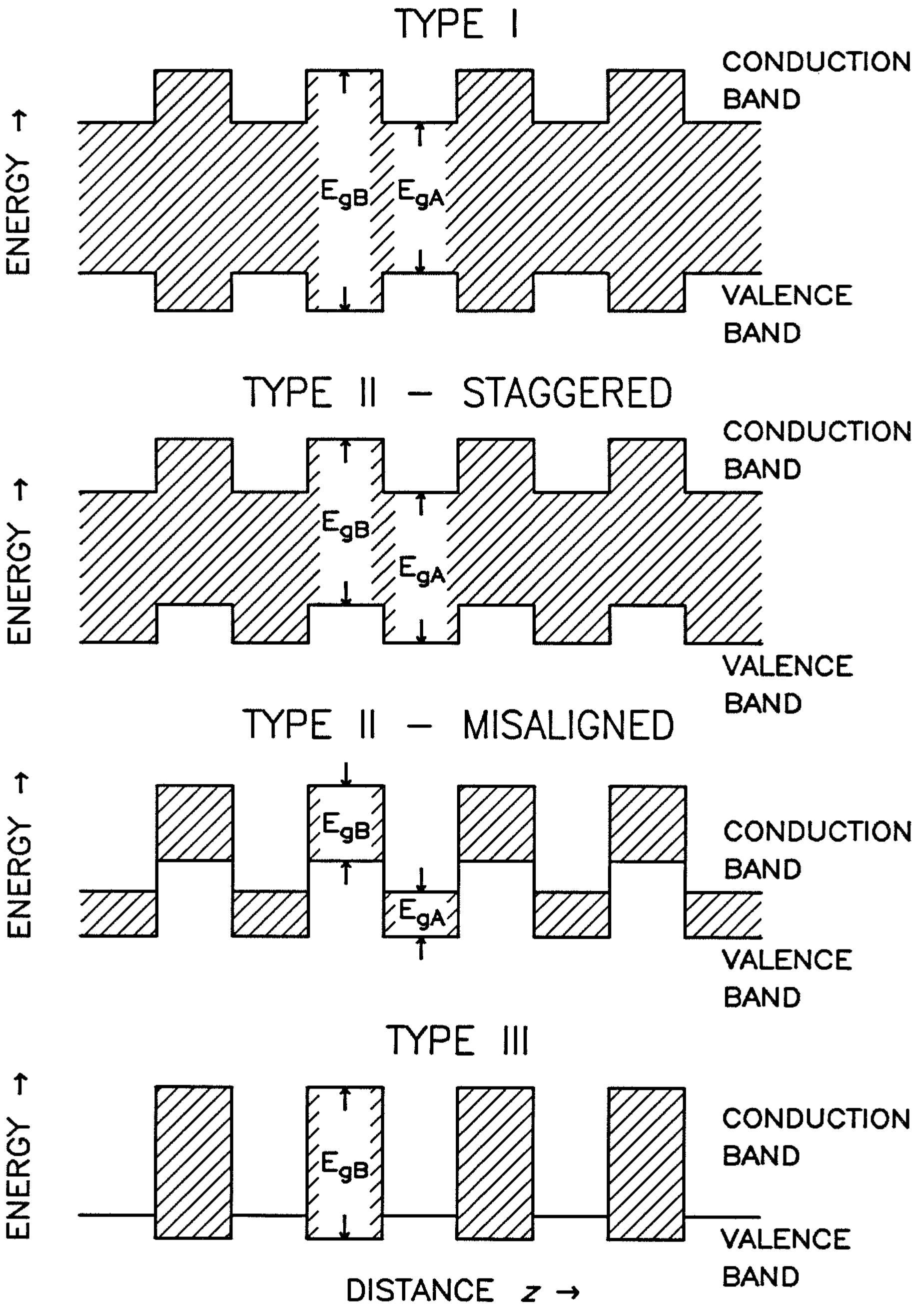

Figure 1.2: Spatial variations of the band edges for three types of superlattices. The horizontal direction is perpendicular to the plane of the layers, and the vertical direction is energy. In each case, material A has a smaller band gap than material B. The shaded regions indicate the band gaps of the consituent materials. (Taken from Ref. 2.)

the band edges of the two materials. The energy offset between the valence band maxima of the two materials is called the band offset. Type I superlattices are characterized by having a band offset such that the electrons and holes are both confined in the same layers. GaAs-$Ga_{1-x}Al_xAs$ is an example of a type I superlattice. Type II superlattices have band offsets such that the electrons are confined to the layers adjacent to the holes. This category has been subdivided into two cases. In the staggered case, there is some overlap between the bands, while in the misaligned case there is no overlap. InAs-GaSb is an example of a type II superlattice. The type III superlattice is similar to the type I superlattice, except one of the materials has zero band gap. HgTe-CdTe is an example of a type III superlattice, since HgTe is a zero band gap semiconductor.

Type I and type III superlattices posess a number of advantages over bulk semiconductor materials for certain applications. In such superlattices, as shown in Section 1.2.1, the band gaps depend on the thicknesses of layers, as well as on the band gaps of the constituent materials. The band-gap energies can be adjusted to values between the band gaps of the constituent materials, and a given band-gap energy can be obtained by a number of combinations of layer thicknesses. Thus the superlattice system has two adjustable parameters. This is an improvement over ternary semiconductor alloys, where the choice of a desired band-gap energy determines all the other material properties. These and other unique properties can be exploited for devices.[2] (The GaAs-$Ga_{1-x}Al_xAs$ superlattice system has been very successful for fabricating lasers.[3]) For some superlattices, it is possible to determine the effects of the compositional modulation on the band structure using a simple model.

1.2.1 The Kronig-Penney model

For some materials, it is possible to determine the band structure of a super-

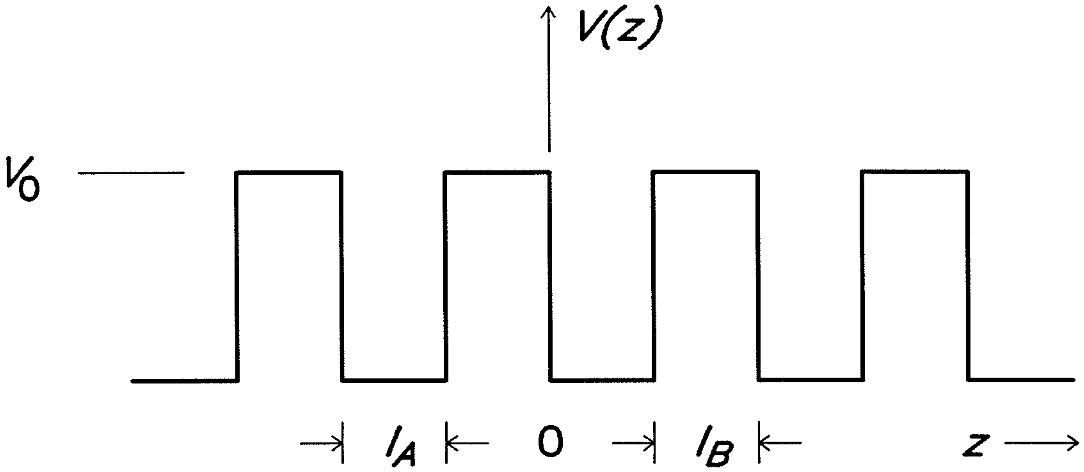

Figure 1.3: Periodic square-well potential for conduction band electrons in a superlattice. The horizontal axis is distance perpendicular to the plane of the layers. The vertical axis is energy. l_A and l_B are the thicknesses of the layers of materials A and B, respectively.

lattice by considering the behavior of the conduction and valence bands separately. (This study will be limited to the band structure in the direction normal to the layers.) In this case, an electron in the conduction band would see a potential like that in Fig. 1.3. Material B is assumed to have a larger band gap than material A. The regions of material B present barriers to the electrons in material A. The potential therefore looks like a periodic array of finite square wells. The band structure for such a potential was solved by Kronig and Penney in 1931.[4] (A good description of the Kronig-Penney model is given in Ref. 5.) In this model, the Schrödinger equation

$$-\frac{\hbar^2}{2m}\frac{d^2\Psi}{d^2z}+V(z)\Psi=E\Psi, \tag{1.1}$$

is solved for one electron in the potential

$$V(z)=\left\{\begin{array}{ll} 0 & n(l_A+l_B)<z<n(l_A+l_B)+l_A \\ V_0 & n(l_A+l_B)+l_A<z<(n+1)(l_A+l_B) \end{array}\right\} n=\text{integer}, \tag{1.2}$$

where l_A and l_B are the thicknesses of the layers of materials A and B, respectively. In the regions of material A, where the potential is zero, the solution will be a linear combination of traveling waves,

$$\Psi = Ae^{ik_A z} + Be^{-ik_A z}, \tag{1.3}$$

where

$$E = \frac{\hbar^2 {k_A}^2}{2m}. \tag{1.4}$$

In the regions of material B, where the potential is V_0, the solution is

$$\Psi = Ce^{k_B z} + De^{-k_B z}, \tag{1.5}$$

where

$$E = V_0 - \frac{\hbar^2 {k_B}^2}{2m}. \tag{1.6}$$

The boundary conditions are the continuity of Ψ and $d\Psi/dz$ at $z = 0$ and $z = l_A$, as well as the Bloch condition. The solution is then given by

$$\frac{{k_B}^2 - {k_A}^2}{2k_B k_A} \sinh k_B l_B \sin k_A l_A + \cosh k_B l_B \cos k_A l_A = \cos qd, \tag{1.7}$$

where q is the electron momentum perpendicular to the layers, and $d = l_A + l_B$ is the superlattice period. A similar anaylsis can be performed for the valence band.

Equation 1.7 gives the band structure of the superlattice normal to the plane of the layers. The band gap will be given by the $q = 0$ solutions of the conduction and valence band equations. This analysis is well suited to type I superlattices when the two constituent materials have similar band structures. The GaAs-$\mathrm{Ga}_{1-x}\mathrm{Al}_x\mathrm{As}$ superlattice is an example of a type I superlattice where the Kronig-Penney model can be used to describe the band structure. However, it may not be appropriate for other types of superlattices. The Kronig-Penney model is not well suited to type II or III structures since the interactions between the conduction and valence bands of the two materials is important. However, it does provide a basis for understanding the properties of superlattices.

1.2.2 Optical studies of superlattices

New superlattice materials are being proposed and grown at a rapid rate. Optical techniques provide a non-destructive means for determining important properties of superlattice materials. For example, photoluminescence experiments can provide information about the band gap of a superlattice. Non-destructive measurements are required during the early stages of development of a particular system, since the number of samples may be quite limited.

1.3 Impurities and defects

In bulk semiconductors, the presence of impurities or defects can have a profound effect on the electrical properties. The most well known types of impurities are the shallow donors and acceptors. For the majority of semiconductor devices, the electrical characteristics are governed by controlling the concentrations of shallow impurities. An important step in learning how to control the properties of a semiconductor is the identification of the centers responsible for the shallow levels. Optical measurements can be very useful here, since they can provide positive identification of the presence of many specific impurities. One method for identifying acceptors in semiconductors is by measuring the excited state spectra.

1.3.1 Effective mass theory

One method for calculating the binding energy of an acceptor in a semiconductor is the effective mass theory. Here the acceptor is treated as a negative point charge in a uniform dielectric medium. The hole is treated as a positive particle with mass equal to the heavy-hole effective mass. The resulting binding energies for the acceptor ground state and excited states are then given by scaling the energies given by the Bohr model of the hydrogen atom by $m_h/m\epsilon^2$, where m_h is the hole effective mass and ϵ is the static dielectric constant for the material. (Baldersechi and Lipari have modified the effective mass theory to include the effects of crystal symmetry and interactions with the light-hole and split-off hole valence bands.[6,7])

The effective mass theory predicts that all acceptors will have the same binding energy, since only the coulombic part of the acceptor potential is considered. This is typically a poor assumption for acceptors.As can be seen from Table 1.1, the binding energy of an acceptor in GaAs depends upon the actual impurity. The difference between the effective mass acceptor binding energy and the actual binding energy is called the central cell shift. A measurement of the central cell shift provides a means of identifying the impurity producing an acceptor in GaAs. The most accurate method for measuring the central cell shift of an acceptor is to determine the energies of the excited states of the acceptor. The *p*-like excited states of a semiconductor are not sensitive to the central cell shift since they have little probability of being near the impurity center, so they experience only the average coulombic potential. Therefore, the *p*-like excited states for all acceptors will be bound with the same energy with respect to the valence band edge. (The excited state spectrum for effective mass acceptors in GaAs has been calculated in Ref. 7.) The central cell shift is then given by the difference between the measured binding energies of the *p*-like excited states relative to the acceptor and those predicted by the theory. The *s*-like excited are also useful, since they experience the non-coulombic part of the acceptor potential to a lesser extent than the ground state does. This is useful for determining the behavior of the central part of the potential, which can provide insight into the structure of the acceptor. Since the relative amount of the central cell shift for the *s*-like excited states has been calculated, thay are also useful for determining the central

Table 1.1: Binding energies of some shallow acceptors in GaAs.[a]

Acceptor	C	Be	Mg	Zn	Si	Cd	Ge	Sn
Energy (meV)	26.0	28.0	28.4	30.7	34.5	34.7	40.4	171
Lattice site	As	Ga	Ga	Ga	As	Ga	As	As

a. These values were obtained from D. J. Ashen, P. J. Dean D. T. J. Hurle, J. B. Mullin, A. M. White and P. D. Greene, *J. Phys. Chem. Solids* **36**, 1041 (1975).

cell shift. There are a number of methods for measuring the binding energies of acceptor excited states optically. Chapter 3 discusses two such techniques which are useful for studying the *s*-like excited states of acceptors.

1.4 Outline of thesis

This thesis is divided into three parts, two devoted to the description of optical studies of semiconductors, and the third to a description of a novel technique for performing infrared photoluminescence measurements.

1.4.1 IRPL from HgTe-CdTe superlattices

Chapter 2 describes the first photoluminescence results from HgTe-CdTe superlattices. This study is important because it represents the first direct determination of the band gap of a HgTe-CdTe superlattice. The HgTe-CdTe superlattice system was first proposed as an interesting infrared material in 1979. Since this system is a type III superlattice, infrared band gaps should be easily attainable for reasonable layer thicknesses. (Ignoring effects due to the discrete nature of the layer thicknesses, it should be possible to obtain band gaps anywhere from near 0 meV to near the band gap of the barrier material in type III superlattices.) There has been a great deal of interest in this system for use in infrared detectors, since the superlattice structure should allow for the tailoring of some properties at a chosen band-gap energy. It is hoped that the HgTe-CdTe superlattice would therefore be superior to the $Hg_{1-x}Cd_xTe$ alloy system, where all the material properties are fixed for a given choice of the band gap.

The first HgTe-CdTe superlattices were grown in 1982. However, these samples were grown with very thick HgTe layers due to difficulties in controlling the layer thicknesses. According to the theories, these first samples should have had band-gap energies very near 0 meV, and would not be suitable for optical studies or as detector material. The degree of growth control has improved since then, and the first samples with HgTe layers thin enough to have infrared band gaps were grown in 1984. The photoluminescence study reported in Chapter 2 was performed using two of these samples.

The results of this study showed that the HgTe-CdTe superlattice system is a promising infrared material. Two superlattices with different layer thicknesses and from different sources were shown to luminesce in the infrared. The luminescence was shown to be consistent with wave-vector conserving band-to-band recombination, allowing the first direct determination of the band gap of a HgTe-CdTe superlattice. Analysis of the luminescence lineshapes showed evidence for the existence of fluctuations in the layer thicknesses. In each case the luminescence was shown to occur at significantly lower energies than that of $Hg_{1-x}Cd_xTe$ alloys with the same Cd concentrations as the average Cd concentrations of the superlattices. The temperature dependence of the luminescence was compared with theoretical predictions. The theory predicted the band gaps of the two structures fairly well, if allowance was made for fluctuations and small errors in the measurements of the sample layer thicknesses. The differences in the behavior of the two superlattices prove that it is possible to tailor the properties of HgTe-CdTe superlattices.

1.4.2 The 78-meV acceptor in GaAs

Chapter 3 reports the first observation of the s-like excited states of a double acceptor in a semiconductor. The center being studied was the 78-meV acceptor in GaAs. It has been found that the presence of the 78-meV acceptor in liquid encapsulated Czochralski (LEC) GaAs indicates the material is p-type, and not suitable for use as a semi-insulating substrate material. It was suspected that this level was due to a double acceptor, possibly involving the Ga_{As} anti-site defect. A determination of the nature of this acceptor will be necessary for controlling the properties of LEC GaAs. The purpose of this study was to measure the s-like excited state spectrum of this level, which should provide information on the potential of this acceptor.

Two experiments were performed, and each showed a splitting of the first s-like excited state of the 78-meV acceptor. The techniques used, selective excitation luminescence (SEL) and electronic Raman scattering (ERS), were chosen for their ability to measure the s-like excited states of single acceptors in semiconductors. An effective mass-like description for a double acceptor in a semiconductor was proposed to explain the observed splitting. This theory was the first to predict a splitting of the $1s^1 2s^1$ state a double acceptor in a semiconductor. A comparison of the data with the theoretical predictions for single acceptors and the double acceptor model led to the conclusion that the 78-meV level in GaAs is due to the first ionization of a double acceptor. The techniques used for this study should be useful for identifying double acceptors in other materials.

1.4.3 Photoluminescence using an FTIR

Appendix A describes the method used to adapt an FTIR to infrared photoluminescence measurements in the presence of a thermal background. The experiment in Chapter 2 required the ability to detect a weak infrared signal whose wavelength was unknown. Initial attempts to use a standard grating spectrometer were unsuccessful due to the poor signal-to-noise ratio inherent in such a system. The grating spectrometer was then replaced with a Fourier-transform infrared spectrophotometer (FTIR). The FTIR had the ability to scan a large wavelength region in a short time with a greater signal-to-noise ratio than that achievable with the grating instrument. However, the small signal strength and the presence of a 300 K blackbody radiation background prevented the observation of the signal. This led to the development of a novel technique for eliminating the background signal when using an FTIR.

References

1. L. Esaki and R. Tsu, IBM Research Note RC-2418 (1969).
2. L. Esaki, in *Proceedings of the 17th International Conference on the Physics of Semiconductors* (Springer Veralg, Berlin, 1985) pp. 473–483.
3. The experiment in Chapter 2 was performed using a commercially available GaAs-$Ga_{1-x}Al_xAs$ multi-quantum well laser diode. The experiment would not have been possible with conventional laser diodes due to the high optical power requirements.
4. R. De L. Kronig and W. J. Penney, *Proc. Roy. Soc. (London)* **A130**, 499 (1931).
5. C. Kittel, *Introduction to Solid State Physics, 5th edition* (John Wiley and Sons, New York, 1976) pp. 191–193.
6. A. Baldereschi and N. O. Lipari, *Phys. Rev.* **B8**, 2679 (1973).
7. A. Baldereschi and N. O. Lipari, *Phys. Rev.* **B9**, 1525 (1974).

Chapter 2

IRPL from HgTe-CdTe Superlattices

2.1 Introduction

2.1.1 Background

The $Hg_{1-x}Cd_xTe$ alloy system has been an important material for use in infrared detectors for many years. The usefulness of this system arises from the basic properties of HgTe and CdTe. HgTe is a zero band gap semiconductor, while CdTe has a band gap near 1.6 eV.[1] As an alloy system, the band-gap energy of $Hg_{1-x}Cd_xTe$ can be tailored to any value between 0 and 1.6 eV. This allows the tailoring of detectors for specific regions in the infrared. $Hg_{1-x}Cd_xTe$ detectors have been used mostly in the regions where the atmosphere is transparent, usually in the 3 – 5 and 8 – 13 μm ranges,[2] although there has been recent interest in using $Hg_{1-x}Cd_xTe$ detectors with fiber optics in the 1.3 – 1.5 μm range. There are a number of material-dependent parameters which can affect the performance of an infrared detector.[3] In the alloy system, once the desired band-gap energy has been chosen, all the other parameters, such as the carrier effective masses, are determined. Given such fundamental limitations to $Hg_{1-x}Cd_xTe$ detectors, new infrared materials are needed to improve device performance.

The HgTe-CdTe superlattice system was proposed as an alternative to the $Hg_{1-x}Cd_xTe$ alloy system.[4,5] A HgTe-CdTe superlattice consists of alternating thin layers of HgTe and CdTe. It is predicted that such a superlattice would have markedly different properties from a HgCdTe alloy of the same average composition.[4,5] With this system, it is possible to obtain a given band-gap energy with a number of different combinations of HgTe and CdTe layer thicknesses (ignoring for the moment the discrete nature of the layer thicknesses). The choice of the layer thicknesses used can then be made to optimize other material properties such as effective masses. These properties might be exploited to improve the performance of devices.[6]

A number of groups have reported the successful fabrication of HgTe-CdTe superlattices.[7–9] The samples have been characterized by Auger-electron spectroscopy, transmission-electron microscopy, secondary-ion-mass spectroscopy and reflectance, all of which indicate the existence of spatial variations of the Hg to Cd ratios. However, until this study, no direct determination of the band gaps has been made. Infrared transmission measurements have been made on some superlattices.[8,10] However, in each case the samples consist of a rather thin layer of superlattice on a substrate. The small change in transmission along with Fabry-Perot resonances make the interpretation of the data rather difficult, leading to some question as to the precise value of the band gap. In contrast, photoluminescence measurements are expected to give a less ambiguous value for the band gap. The advantage here is that photoluminescence should produce a peak near the band gap. Infrared transmission experiments usually involve fitting the transmission curve to a theoretical model, and extrapolating to find the band-gap energy. This can produce ambiguous results with thin samples since the absorption may not become significant until the energy is well above the band gap.

2.1.2 Results of this study

This chapter reports on the first measurements of photoluminescence from HgTe-CdTe superlattices. Two superlattice samples of differing composition, and from different sources, were shown to luminesce in the infrared. Analysis of the luminescence lineshapes showed the luminescence to be consistent with that expected for wave-vector conserving band-to-band recombination. These measurements then represent the first direct determination of the band gaps of HgTe-CdTe superlattices. The dependence of the luminescence on the sample temperatures was also studied, from 100 to 270 K. In each case, the luminescence was shown to occur at significantly lower energies than that of $Hg_{1-x}Cd_xTe$ alloys with Cd concentrations equivalent to the average Cd concentrations of the respective superlattices. This result is consistent with the current theories, which predict such an effect.[4,5,11] A comparison of the data with a simple temperature-dependent model of HgTe-CdTe superlattices was made, showing good qualitative agreement. This study proves that HgTe-CdTe superlattices have different optical properties than $Hg_{1-x}Cd_xTe$ alloys. The photoluminescence data seemed to show a lack of impurity luminescence, indicating that the electrical properties of the HgTe-CdTe superlattices may be superior to those of $Hg_{1-x}Cd_xTe$ alloys. The difference in the luminescence from the two samples shows that it is possible to tailor the properties of HgTe-CdTe superlattices, an important requirement for device fabrication.

2.2 Sample descriptions

Two different HgTe-CdTe superlattice samples from two different sources were used for this experiment. Both samples were grown in molecular-beam epitaxy (MBE) machines specially tailored to handle Hg. Sample 1 was grown to have 250 repeats of 38 to 40 Å of HgTe followed by 18 to 20 Å of CdTe.[7] The layer thicknesses were obtained from the calibrated growth rates for the source fluxes used. The total superlattice thickness was measured by a surface profilometer, and confirmed by analysis of the interference fringes in the infrared transmission data.[10] The total superlattice thickness obtained by these methods ($\sim 1.5\,\mu$m) is approximately equal to that obtained by using the source fluxes. The substrate material for sample 1 was (111)-oriented $Cd_{0.96}Zn_{0.04}Te$. The zinc concentration was chosen such that the lattice constant of the substrate would be between that of CdTe and that of HgTe. It has been shown that higher quality crystal growth of both HgTe-CdTe superlattices and $Hg_{1-x}Cd_xTe$ alloys can be obtained by using such CdZnTe substrates.[7] Sample 2 was grown to have 75 repeats of 50 Å HgTe followed by 50 Å CdTe.[8] The total thickness as measured by a mechanical stylus was $\sim 0.75\,\mu$m, in approximate agreement with the sum of the layer thicknesses. The substrate material for sample 2 was (111)-oriented CdTe. A 2500 Å CdTe buffer layer was grown before the superlattice. (No buffer layer was grown on the substrate for sample 1 since the MBE machine was not equipped to grow CdZnTe.) No direct measurement of the individual layer thicknesses of either superlattice was made, therefore the accuracy of the quoted thicknesses is not easily determined.

A HgCdTe alloy sample was used for comparison with the superlattice photoluminescence spectra. The sample was $Hg_{0.71}Cd_{0.29}Te$, grown by the solid state recrystallization method, and was annealed in Hg vapor to reduce the number of Hg vacancies.[12]

2.3 Description of experiment

2.3.1 General

The photoluminescence experiment for this study required good response over a wide range of infrared wavelengths. Early theoretical predictions for the band gap values of the samples used in this study ranged from 5 to 12 μm at 0 K. Thus there was no way of knowing where to expect the luminescence. Scanning this large a wavelength region presents a few problems. First, the detectors available for this range have rather limited detectivities (see Table 2.1). This necessitates long integration times to observe even moderately strong sources. The type of optics to be used is another important consideration (see Table 2.2). Many of the materials which are transparent in the infrared have drawbacks such as water solubility or large thermal expansion coefficients which limit their usefulness. The experiment is further complicated by the large background of 300 K blackbody radiation, which peaks at 10 μm. All of these factors must be carefully considered when designing the experiment.

2.3.2 Dispersive spectrometer experiment

The initial experimental setup used was based on a SPEX 1404 double grating spectrometer (see Fig. 2.1). This setup was used for all the substrate luminescence studies, as well as the initial search for the superlattice photoluminescence. The spectrometer could cover a range of 0.4 – 12 μm by using a series of gratings, each blazed for a particular wavelength (see Table 2.3). The gratings had to be changed to reach the various ranges, which added to the time required for the experiment.

Three detectors were used to cover the region being studied. The detector used for the 0.4 – 1.2 μm range was an S-1 curve photomultiplier tube cooled

Table 2.1: Properties of selected infrared detectors.[a]

Material	Useful range[b] (μm)	$D^*(\lambda_{max})$[c] (cmHz$^{1/2}$/W)	λ_{max}[d] (μm)	Temp[e] (K)
InAs	1 – 3.3	5×10^{11}	3	77
InSb	1 – 5.5	8×10^{10}	5	77
Ge:Cu	2 – 27	1.5×10^{10}	20	4.2
Ge:Zn	2 – 43	1×10^{10}	33	4.2
HgCdTe[f]	3 – 15	2×10^{10}	10 – 14	77
	5 – 20	3×10^{9}	14 – 16	

a. The values used in this table are from the SBRC Inc. Infrared Components Brochure.

b. This range represents typical wavelengths where the detector may be used, although the performance can be much lower than the peak performance when used far from λ_{max}.

c. This value represents the maximum detectivity of the detector.

d. The wavelength where the detectivity is greatest.

e. The temperature at which the detector is operated.

f. The parameters for HgCdTe detectors depend on the alloy composition used, which determines λ_{max}.

Table 2.2: Properties of selected infrared optical materials.[a]

Material	Useful range[b] (μm)	Transmission[c] %	Other Properties
Quartz	.2 – 3	94	hard, will temperature cycle
Sapphire	.2 – 5.5	94	hard, will temperature cycle
BaF_2	.2 – 11	94	cleaves, hygroscopic
IRTRAN2	.5 – 12	70	hard, will temperature cycle
KCl	.2 – 17	94	soft, water soluble
ZnSe	.6 – 20	70	hard, good for CO_2 laser optics
KRS5	.6 – 40	70	toxic, soft, cold flows under pressure
CsI	.3 – 50	85	soft, highly water soluble

a. The values used in this table are from the Janos Technology Inc. Precision Optics and Components Catalogue.

b. This range represents the wavelengths where the material is transparent, although the transmission can be much lower than the peak value near the ends of the range.

c. This value represents the maximum transmission of the material. The behavior away from the maximum depends on the material.

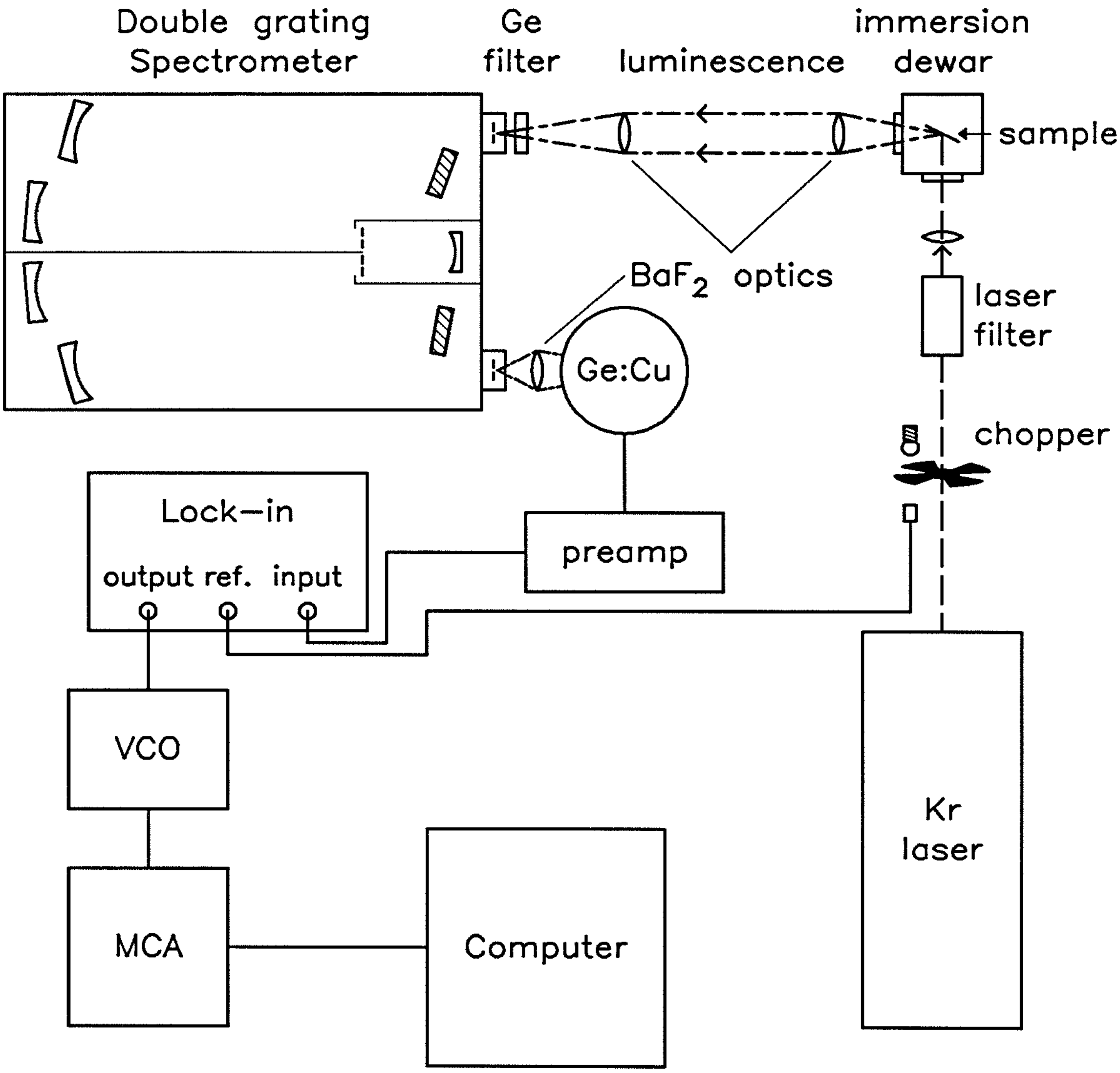

Figure 2.1: Dispersive spectrometer experimental setup. The output windows on the dewar were IRTRAN2 and ZnSe. The transfer lenses were BaF_2. A Ge filter was placed before the spectrometer entrance slit to prevent higher order light from hitting the detector. The detector was Ge:Cu at 4.2 K. The chopping frequency was 1 kHz.

Table 2.3: Available gratings for spectrometer.

blaze wavelength (μm)	grooves/mm	wavelength range (μm)
1.6	600	0.4 – 1.2 (second order)
1.6	600	1.2 – 2.4 (first order)
3.0	300	2.4 – 4.0
6.0	150	4.0 – 8.0
10.0	75	8.0 – 12.0

to 77K. This was used to study the photoluminescence properties of the superlattice substrates. The 1.2 – 3.0 μm range was covered by an InAs photovoltaic detector cooled to 77K. A copper-doped germanium detector (Ge:Cu) was used to cover the remaining 3 – 12 μm range. All the external optics used were BaF_2, which is transparent from 0.3 – 13 μm and only slightly hygroscopic. The samples were mounted in a Janis DT-8 variable temperature immersion dewar. The use of an immersion dewar presents a problem in the infrared. There are few infrared materials which can be cemented to the aluminum sample chamber and cycle from room temperature to 1.8 K. IRTRAN2 was the best compromise for this application, since it could tolerate the temperature range, and has a similar coefficient of thermal expansion to that of aluminum. This choice limited the long wavelength transmission to about 12 μm (see Table 2.2). The dewar also had an internal cold shield between the sample chamber and the outer wall, but no window was used here (the transmission of the available windows is not very high, and their effectiveness as a cold shield is limited by their transparency to infrared radiation) The outer window was ZnSe, used mainly due to its availablity (BaF_2 would have been preferable). The window was not anti-reflection coated, which would have limited its range of usefulness. The tradeoff was 70% transmission over the extended range. A Ge band-pass filter was placed in front of the spectrometer entrance slit to filter out the laser light, as well as to prevent higher order light from hitting the detector.

A Coherent CR-3000K krypton ion laser was used as the optical pump source. Either the 6471 Å or the 6764 Å line was used, and was chosen by using a SPEX 1460 grating spectrometer to filter the beam. To minimize the effects of the 300 K blackbody radiation background, the standard method of synchronous detection was employed. When using the Ge:Cu detector, the laser light was chopped at a frequency of 1.02 kHz, chosen to maximize the signal-to-noise ratio of the detector. The Ge:Cu detector used was an SBRC 9145-2, with a matching model A130 preamplifier. The ouput of the preamplifier was fed into a PAR model 124A lock-in amplifier using a model 117 preamplifier. The input filter on the lock-in was set at band-pass mode at the chopping frequency, and the Q was set to 100 (the maximum setting). This was designed to filter noise, since the signal would be a slowly varying modulation at the chopping frequency. The output time constant was typically $1 - 3$ seconds with a 12 db/octave slope. This output filtering was necessary due to the weak signal strength. The output from the lock-in amplifier was sent to a VCO based on an Analog Devices 458J chip. The VCO provided an output pulse rate proportional to the input signal, and had a dynamic range of 10^5, since the full scale output voltage of the lock-in matched the full scale voltage of the VCO (10 volts). The gain setting on the lock-in amplifier could then be chosen such that the RMS noise level corresponded to about 100 counts out of the VCO. In practice, this meant the lock-in was always set for the lowest gain (× 20). By using this technique, the maximum benefit of the VCO dynamic range could be obtained, and it was possible to avoid overloading the input amplifier of the lock-in with a strong signal. The ouput pulses from the VCO were then fed to a multichannel analyzer for storage, and on to a computer for analysis.

2.3.3 Limitations of the dispersive approach

A photoluminescence scan of the HgCdTe alloy sample is shown in Fig. 2.2. The signal-to-noise ratio in this spectrum is not very good, considering that it required an integration time of 15 minutes. Luminescence from this sample could be detected only at temperatures below 20 K using this setup. Using this setup, no luminescence signal was seen from either superlattice in the 1.6 – 12 μm range. All the luminescence at wavelengths shorter than 1.6 μm could be attributed to the substrates. The low signal-to-noise ratio observed here can be traced to limitations in the setup. In a double grating spectrometer, the grating efficiency drops very rapidly as it is tuned away from the blaze angle. For the spectrometer used here, the throughput for gratings blazed at wavelength λ will be down to 25% of the maximum at $2\lambda/3$ and 2λ. The gratings must be changed frequently when scanning large wavelength ranges to achieve maximum throughput, and there are still regions where the efficiency is quite low. Atmospheric absorptions are quite strong in some regions in the infrared, therefore it is important to limit the optical path length in air for the signal. Unfortunately, even though the spectrometer was nitrogen purged, the flow rate was not great enough to lower the absorption significantly (the optical path length within the spectrometer is nearly 8 meters, making it by far the longest path in the system). Further, the BaF_2 optics used were not optimized for either the detector or the spectrometer. The field of view of the detector was 60°, which corresponds to f/0.58, and was not matched by the optics. All of these factors lead to a lowering of the signal-to-noise ratio.

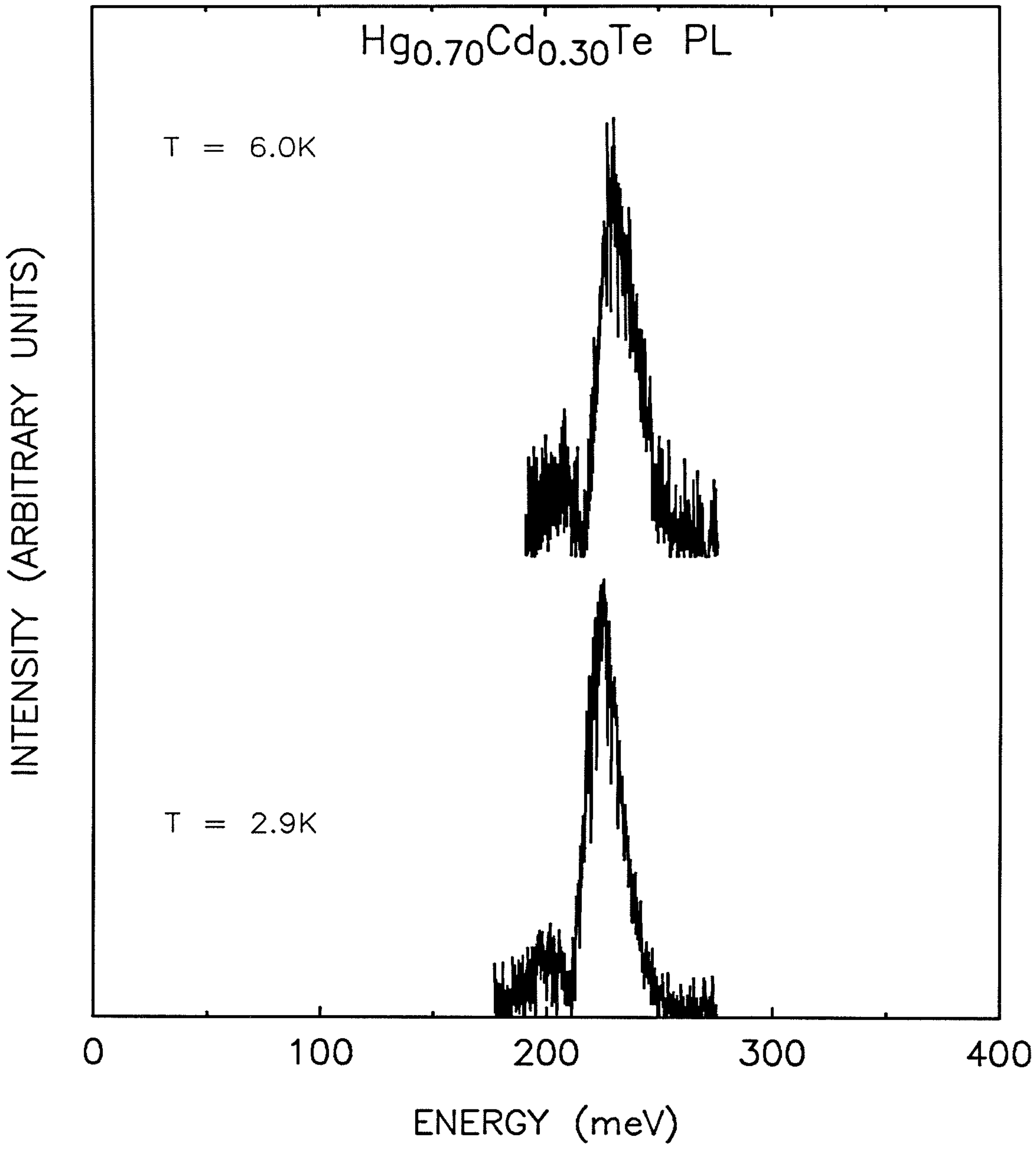

Figure 2.2: Photoluminescence spectra of a $Hg_{0.70}Cd_{0.30}Te$ alloy, taken with the grating spectrometer setup. The gratings used were blazed for 6 μm (see Table 2.3). A Ge:Cu detector was used, and the total scanning times were 15 minutes in each case. These scans represent the maximum signal-to-noise ratio attainable in this wavelength range due to their proximity to the blaze wavelength.

It was then necessary to devise a photoluminescence experiment with a greater signal-to-noise ratio. The main disadvantage of the above setup is the use of a grating spectrometer. Dispersive instruments are poorly suited to infrared work since any increase in resolution is accompanied by a decrease in the signal-to-noise ratio. Only a small fraction of the total luminescence intensity is incident on the detector at any given time, and as the resolution increases, this fraction decreases. In many photodetectors, the signal-to-noise ratio increases as the intensity of light falling on the detector increases.[13] This is true of the photoconductive detectors used for this study. A better signal-to-noise ratio would be achieved if all the light could fall on the detector during the scan. This is precisely the situation in a Fourier transform infrared spectrophotometer.

A Fourier transform infrared spectrophotometer (FTIR) is basically a Michelson interferometer with a moving mirror for scanning in wavelength (see Appendix A for a more complete description). Such a spectrometer posesses two major advantages over the dispersive instrument: the ability to have a large percentage of the sample luminescence incident on the detector throughout the scan, and the ability to scan large wavelength regions without the need to change gratings. The end result is a much greater signal-to-noise ratio than that achieved by dispersive instruments. An FTIR also doesn't suffer from the loss of throughput inherent in grating spectrometers off the blaze wavelength, however there are losses due to the efficiency of the beamsplitter.

An FTIR is not a solution in itself, however. Appendix A discusses the problems associated with doing infrared photoluminescence with an FTIR, and presents a unique solution for overcoming them.

2.3.4 FTIR experiment

The final experimental setup was based on a Bomem DA3.01 Fourier transform infrared spectrophotometer (see Fig. 2.3). This particular instrument offered the advantages of an external viewport and easy access to the signal from the detector before it entered the Fourier transform computer. The detector used was zinc-doped germanium (Ge:Zn), cooled to 4.2 K. The internal beamsplitter and the external viewport were KCl (see Table 2.2). The entire spectrometer was evacuated to 17 mTorr during the measurements. The external infrared optics were all KCl, and matched to the f/numbers of the spectrometer input (f/4) and the dewar exit window (f/2). A long-pass Ge filter with a 2 μm cutoff wavelength was placed before the FTIR external viewport to filter out stray laser light.

The optical pump source was an SDL 2410-C multi-quantum well laser diode operated at 77 K, with a typical average power of 200 mW.[14] The laser diode was powered by an HP 214B pulser, operating at a frequency of 40 kHz, with a 50% duty cycle. The signal from the Ge:Zn detector was sent to an Ithaco 1211 current mode preamplifier. The high frequency response limit of the 1211 was 56 kHz; therefore, the pulsing frequency was limited to 40 kHz to prevent attenuation and phase shifting of the signal. The output from the preamplifier was sent to a PAR 124A lock-in amplifier for demodulation. The lock-in preamplifier was a PAR 116 operated in direct mode. The lock-in gain was typically 10^4. The 116 preamp was not optimized for this configuration, since the output impedance of the 1211 preamplifier was 600 Ω, and the input impedance of the 116 was 10 MΩ. The noise figure for this arrangment was 6 db (the amplifier added 6 db to the thermal noise at the input). The input filter on the lock-in was set to 20 kHz, high pass, with a Q of 1. The output time constant on the lock-in was set to minimum, which corresponded to a value of about 600 μs. The slope was set to 6 db/octave. The ouput from the lock-in was sent to the Fourier transform computer. Appendix A describes the motivation behind the settings chosen.

The samples were mounted in a Janis Supertran variable temperature dewar,

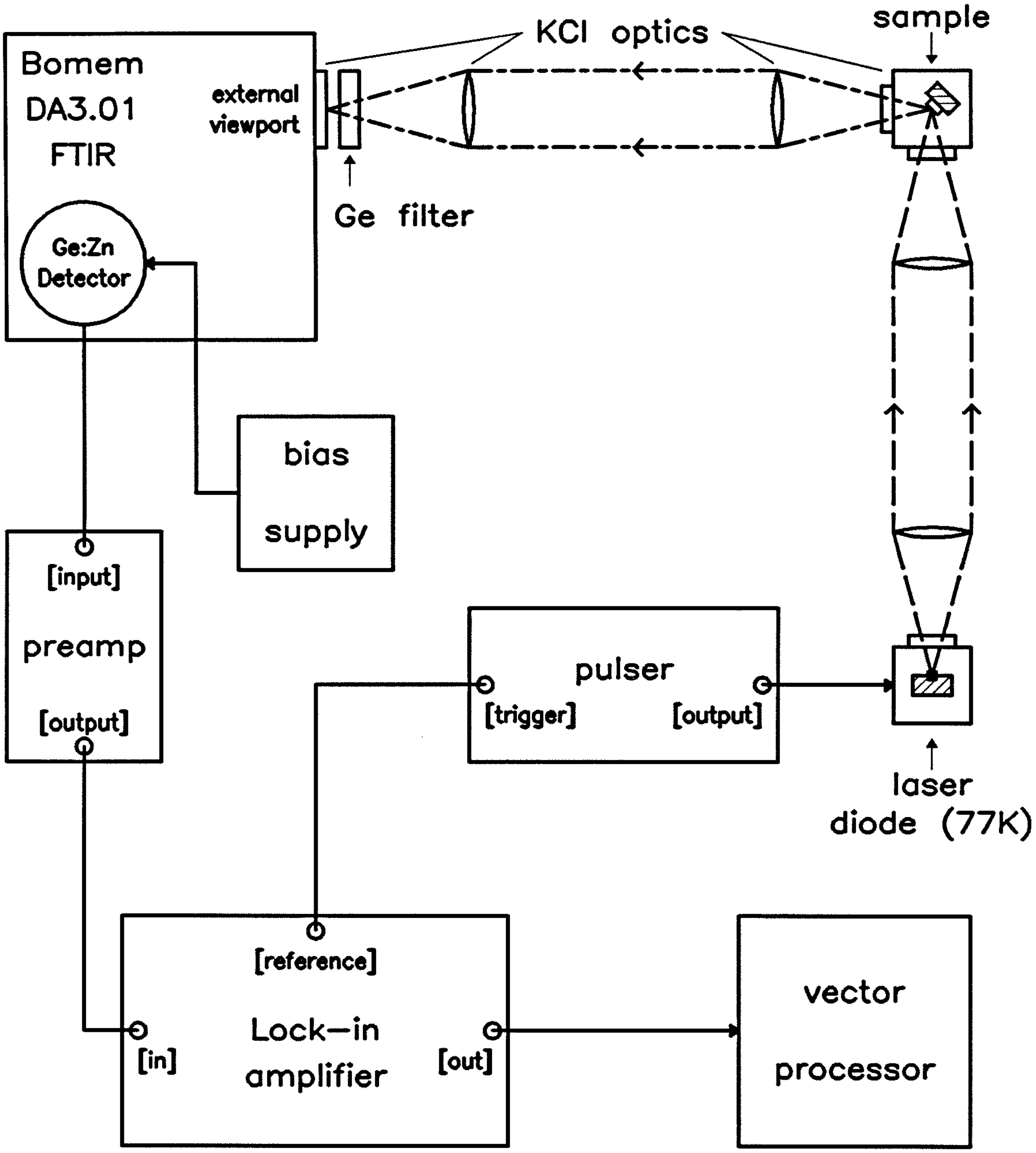

Figure 2.3: FTIR experimental setup. The infrared optics were all KCl, including the FTIR beamsplitter. A Ge filter was placed before the spectrometer viewport to filter out stray laser light. The detector was Ge:Zn cooled to 4.2 K. The laser frequency was 40 kHz.

with a KCl exit window. This dewar consists of a liquid-helium-cooled cold finger which is mounted in a vacuum. This arrangement posed a sample heating problem. The samples were originally mounted by the method used in immersion dewars — masking tape was used to hold the samples to the cold finger. While this is sufficient for immersion dewars, it did not work well in a vacuum; when the samples were illuminated with 200 mW average laser power, the samples were observed to heat up from 12 K to over room temperature in a few minutes. The mounting procedure was changed to the following: the samples were placed on indium foil on the copper cold finger. A corner of the foil was folded over to the front of the sample, and used as the contact point for a metal spring clamp. This method worked fairly well for heat sinking the sample, but had the disadvantage of straining the sample slightly. However, there was no indication that the strain had any effect on the luminescence.

The wavelength range covered by this system was roughly $2 - 17\,\mu$m. A system response curve was not obtained since there was no broadband infrared source available which could be modulated at 40 kHz. Given the degree of electronic filtering of the system, a meaningful response curve would require the source to be modulated at the frequency used for the measurements. Given the output time constant of the lock-in amplifier, and the 6 db/octave slope, the 3 db signal strength point occured at 265 Hz. Thus the signals from wavelengths modulated by the FTIR to frequencies higher than 265 Hz would be attenuated by the lock-in amplifier. Figure 2.4 shows the theoretical response curve of this filter is plotted against the energy of the luminescence signal. All the spectra were corrected for this filter response. The effect of the correction is not large, but it is readily visible in the noise amplitude. Without the correction, the noise amplitude decreases toward higher energy (higher frequency), while after the correction the noise amplitude is fairly independent of the frequency.

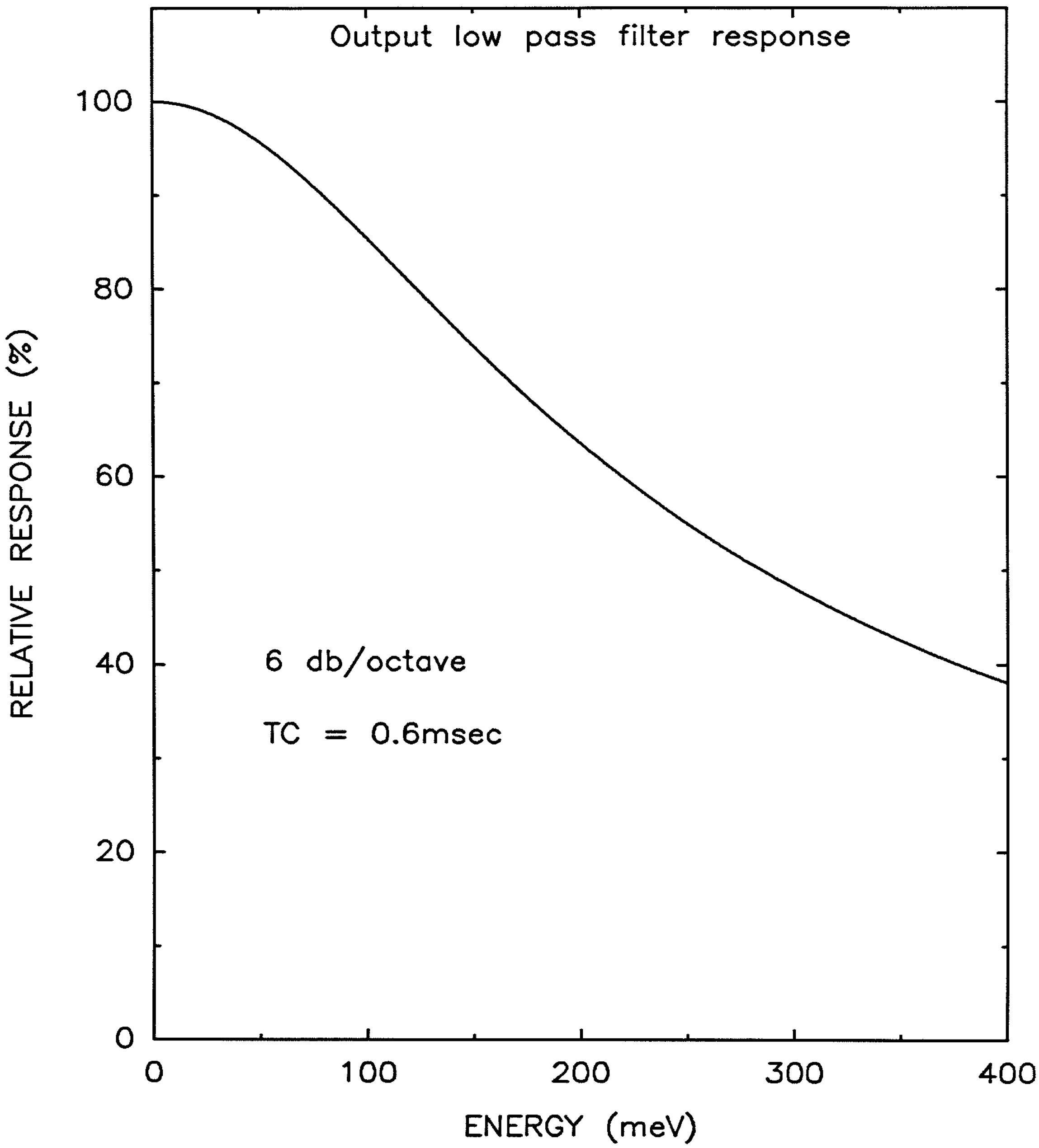

Figure 2.4: Theoretical response curve for the output low-pass filter, plotted against the energy of the luminescence entering the spectrometer. The curve was determined from the filter response and the wavenumber-to-frequency conversion for the mirror speed used in the experiments.

The improvement in the signal-to-noise ratio gained by using this technique was impressive. Compare the signal-to-noise ratio of the 30 K curve in Fig. 2.5 with that of Fig. 2.2. It was possible to measure the photoluminescence from the alloy sample up to room temperature with this setup, whereas the upper limit for the original setup was 20 K. The broad feature in the upper two curves centered at 120 meV is thought to be due to room temperature blackbody radiation reflected off the sample.

2.3.5 Modulated reflectivity

If the reflectivity of the sample were modulated at the laser frequency, then the detector would see specularly reflected raditation from the room temperature entrance window on the dewar. This would produce a broad spectrum, peaking at 120 meV. Such an effect has been seen in $Hg_{1-x}Cd_xTe$ alloys.[15] In this case, above band-gap radiation creates free carriers in the bands, which behave as an electron-hole plasma. At sufficiently high carrier densities, the dielectric function can be appreciably altered, changing the reflectivity. This effect is most pronounced at long wavelengths.

An experiment was performed to test for modulated reflectivity of the alloy sample used here. The setup is shown in Fig. 2.6. The sample was mounted on an aluminum block at room temperature to provide some degree of heat sinking. The 6471 Å line of a krypton ion laser was used as the pump source. The plasma lines were filtered by a Spex 1460 grating spectrometer. The illuminating laser power density was chosen to be 12 W/cm^2, to match that used in the IRPL experiment. The laser beam was chopped at 1 kHz, and was incident normal to the sample surface. A blackbody source at 1470 K was placed at 45° to the sample surface, such that the specularly reflected blackbody radiation was incident on a $Hg_{1-x}Cd_xTe$ detector. A long-wavelength pass Ge filter was placed

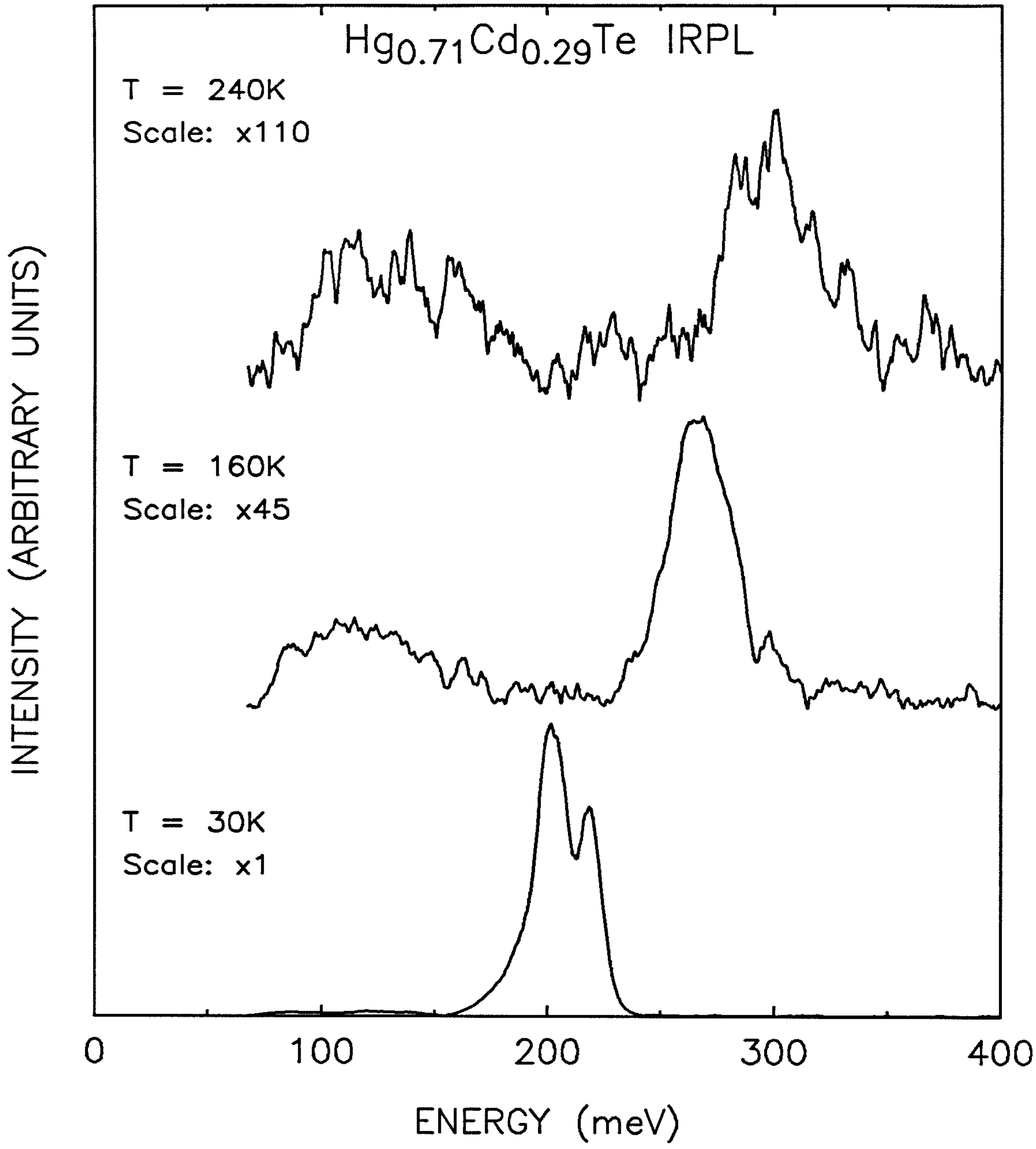

Figure 2.5: This figure shows IRPL from a $Hg_{0.71}Cd_{0.29}Te$ alloy sample. The temperature for each curve is given at the left, along with a relative vertical scale indication. The optical pump density was $12 W/cm^2$. Note the improved signal-to-noise over the dispersive spectrum. The broad feature centered at 120 meV is due to room temperature blackbody radiation, and is explained in the text.

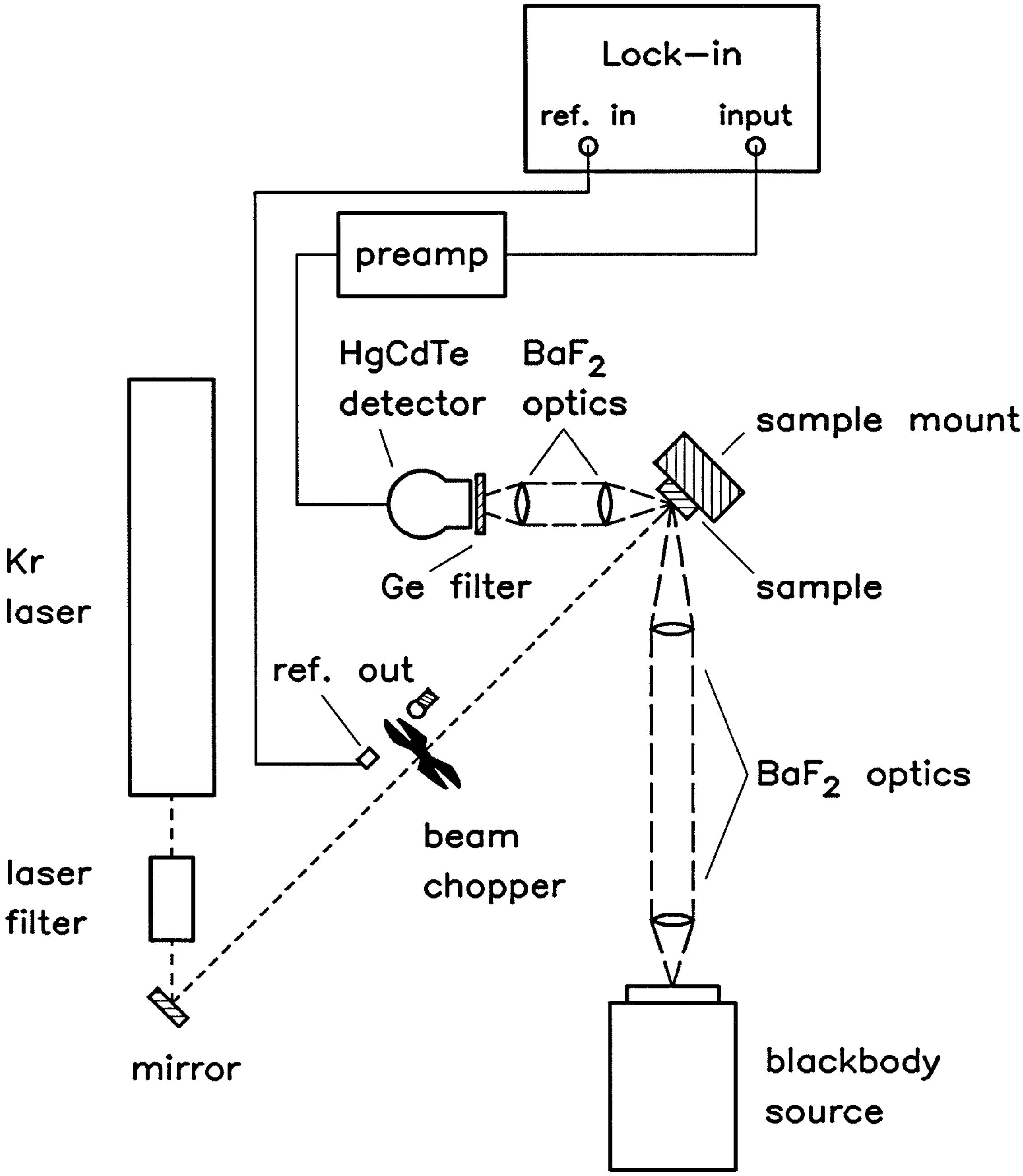

Figure 2.6: Modulated reflectivity experimental setup. A Kr ion laser was used as the pump source. The specularly reflected blackbody radiation was directed onto a HgCdTe detector, cooled to 77K. A Ge filter was used to block stray laser light. The infrared optics were all BaF_2. The signal was observed visually on the lock-in amplifier. The sample was at room temperature.

before the detector to prevent scattered laser light from hitting the detector. The output from the detector was synchronously demodulated at the chopping frequency with a lock-in amplifier. If either the laser or the blackbody were blocked, no signal was seen at the detector. This proved that the signal was not due to the laser or blackbody alone. With the laser on, a small signal could be seen at the lock-in. This signal was due to the reflectivity of the sample being modulated at the laser frequency. When the laser power was increased by a factor of 5, a very small signal was observed at 180° out of phase with the stronger signal. This signal was interpreted to be due to modulating the temperature of the sample at the chopping frequency.

A final test for modulated reflectivity was performed using the FTIR experiment by placing a glass window on the cold shield input port. This would ensure that the specular reflection off the sample would be from a surface with a temperature between room temperature and the sample temperature. The signal strength of the $10\,\mu$m feature was observed to decrease in this case. The distinguishing features of this signal are that it is very broad, relatively weak, and the peak position is independent of the sample temperature. It seemed to show up more dramatically at high temperatures, due to the lower luminescence signal strength, and hence the expanded vertical scale. The luminescence signal strength is expected to decrease with increasing temperature, and the output low-pass filter rolloff will decrease the observed intensity of signals as they shift to higher energies. Another factor is that the ambient temperature of the dewar is higher; thus, the cold shield will be closer to room temperature.

In the subsequent experiments, care was taken to ensure that the FTIR viewed a cold surface in the specular reflection off the samples. This was accomplished either by placing a glass window on the cold shield input port, or turning the sample such that the specular reflection along the line of sight of the FTIR came from the cold shield wall. The FTIR experiment made it possible to observe the photoluminescence from the two superlattice samples.

2.4 Results

2.4.1 $Hg_{1-x}Cd_xTe$ alloy IRPL

Infrared photoluminescence measurements were made on a $Hg_{0.71}Cd_{0.29}Te$ sample to test the FTIR system and for comparison with the superlattice results. Figure 2.7 shows four IRPL spectra from the $Hg_{0.71}Cd_{0.29}Te$ alloy sample, each taken at a different temperature. Alloy spectra were taken at a range of temperatures, from 20 – 185 K, although alloy luminescence was detected even at room temperature. The lower scan in Fig. 2.7 shows a distinct peak at 199 meV, a shoulder on the high energy side at 213 meV, and a shoulder on the low energy side at roughly 7 meV. As the temperature increases to 50 K, the low energy shoulder disappears, and the high energy shoulder becomes a pronounced peak. By 100 K, the original peak is merely a slight shoulder on the high energy line, and has completely vanished by 185 K. The dip in the 185 K spectrum at 290 meV corresponds to the 4.2 – 4.3 μm atmospheric CO_2 absorption line. The broad feature in the 185 K spectrum near 120 meV is thought to be due to reflected room temperature blackbody radiation, as described in Section 2.3.5. This sample was included for comparison with HgTe-CdTe superlattice sample 1. If the superlattice layers grown in sample 1 had completely interdiffused into a uniform alloy, then the resulting Cd concentration would have been 33%. Thus the band gap would be greater than that for the $Hg_{0.71}Cd_{0.29}Te$ alloy sample.

2.4.2 HgTe-CdTe superlattice sample 1 IRPL

Figure 2.8 shows infrared photoluminescence data from HgTe-CdTe superlat-

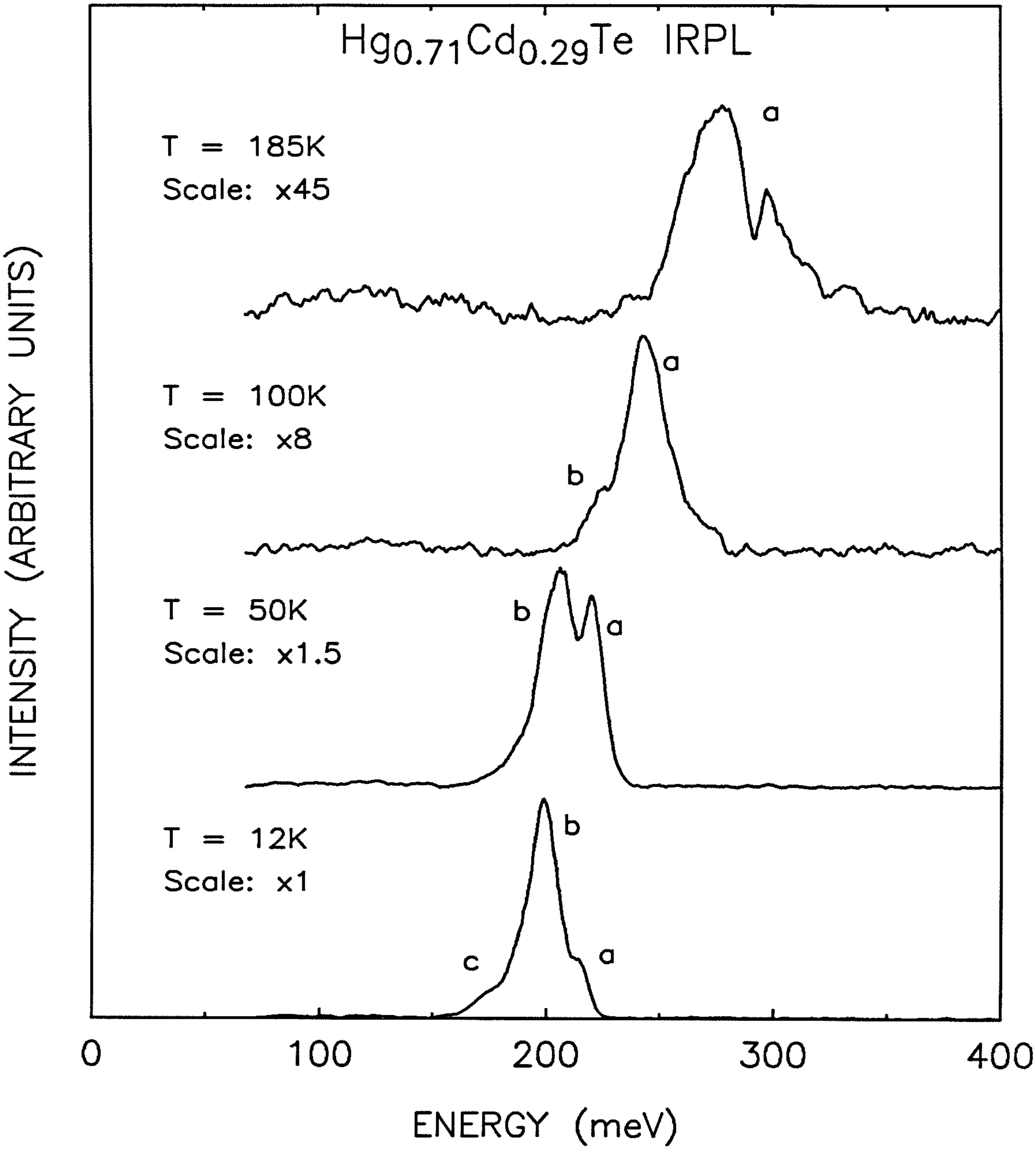

Figure 2.7: Infrared photoluminescence spectra from a $Hg_{0.71}Cd_{0.29}Te$ alloy. The sample temperature for each spectrum is indicated at the left. The scale reference is used to indicate the relative magnification on the vertical axis for each spectrum, with the bottom spectrum taken as 1.

tice sample 1, taken at four different temperatures. At 180 K, the peak position of sample 1 is at 122 meV, with a full width at half-maximum intensity of 48 meV. Contrast this with the $Hg_{0.71}Cd_{0.29}Te$ sample at 185 K, where the peak position is at 276 meV. The luminescence peak from sample 1 occured at lower energy than the peak from the alloy sample at all temperatures, consistent with the theoretical predictions for superlattices. The signal intensity seen from sample 1 was less intense than that of the alloy sample at all temperatures. No luminescence signal was detected from sample 1 at temperatures below 80 K. This is probably due to the luminescence peak position shifting to a wavelength beyond the cutoff of the optical system at 17 μm (73 meV).

2.4.3 HgTe-CdTe superlattice sample 2 IRPL

Figure 2.9 shows infrared photoluminescence data from HgTe-CdTe superlattice sample 2, taken at four different temperatures. At 170 K, the peak position is near 205 meV, with a full width at half-maximum intensity of 74 meV, considerably broader than the peak from sample 1. There is a second less-intense peak near 87 meV, which is present only at temperatures 170 K and below. It is not certain whether this signal is due to a luminescence process in the sample, or has some other origin. There is a possibility that it is due to modulated reflectivity of the sample, but this is not likely. First, the signal goes away as the temperature is increased, contrary to the alloy case, and second, the peak position is too low in energy to correspond to room temperature blackbody radiation. No luminescence signal was seen from sample 2 at temperatures below 110 K. The peak intensity from sample 2 over most of the temperature range was lower than that from sample 1 by a factor of approximately 3 at a pump power of 1.7 times that used for sample 1. This intensity difference accounts for the additional noise seen in the spectra from sample 2.

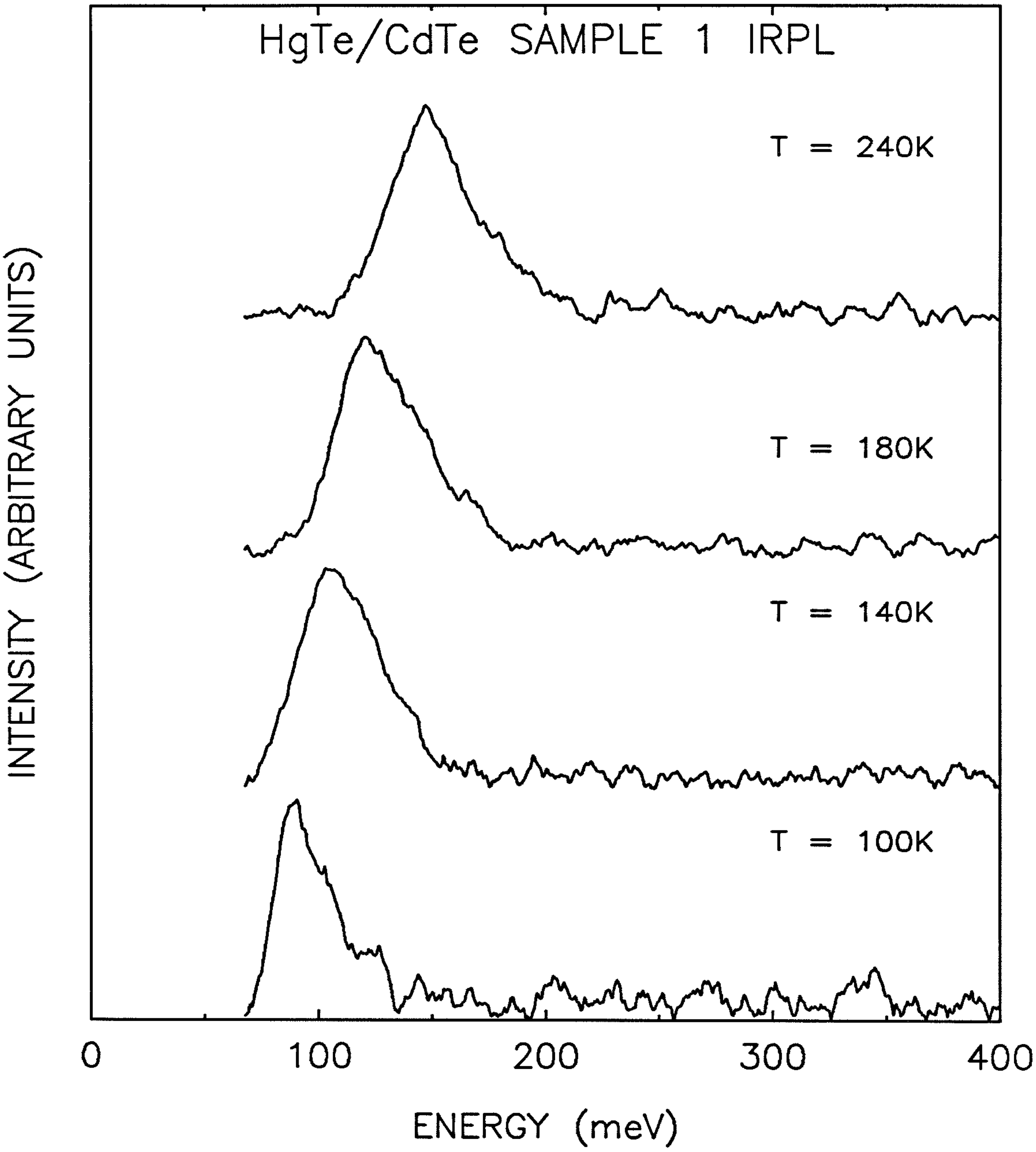

Figure 2.8: Infrared photoluminescence spectra from HgTe-CdTe superlattice sample 1. The sample temperature for each spectrum is at the right. The long wavelength cutoff of the optical response of the system is near 73 meV (17 μm). Each spectrum is plotted on a different vertical scale.

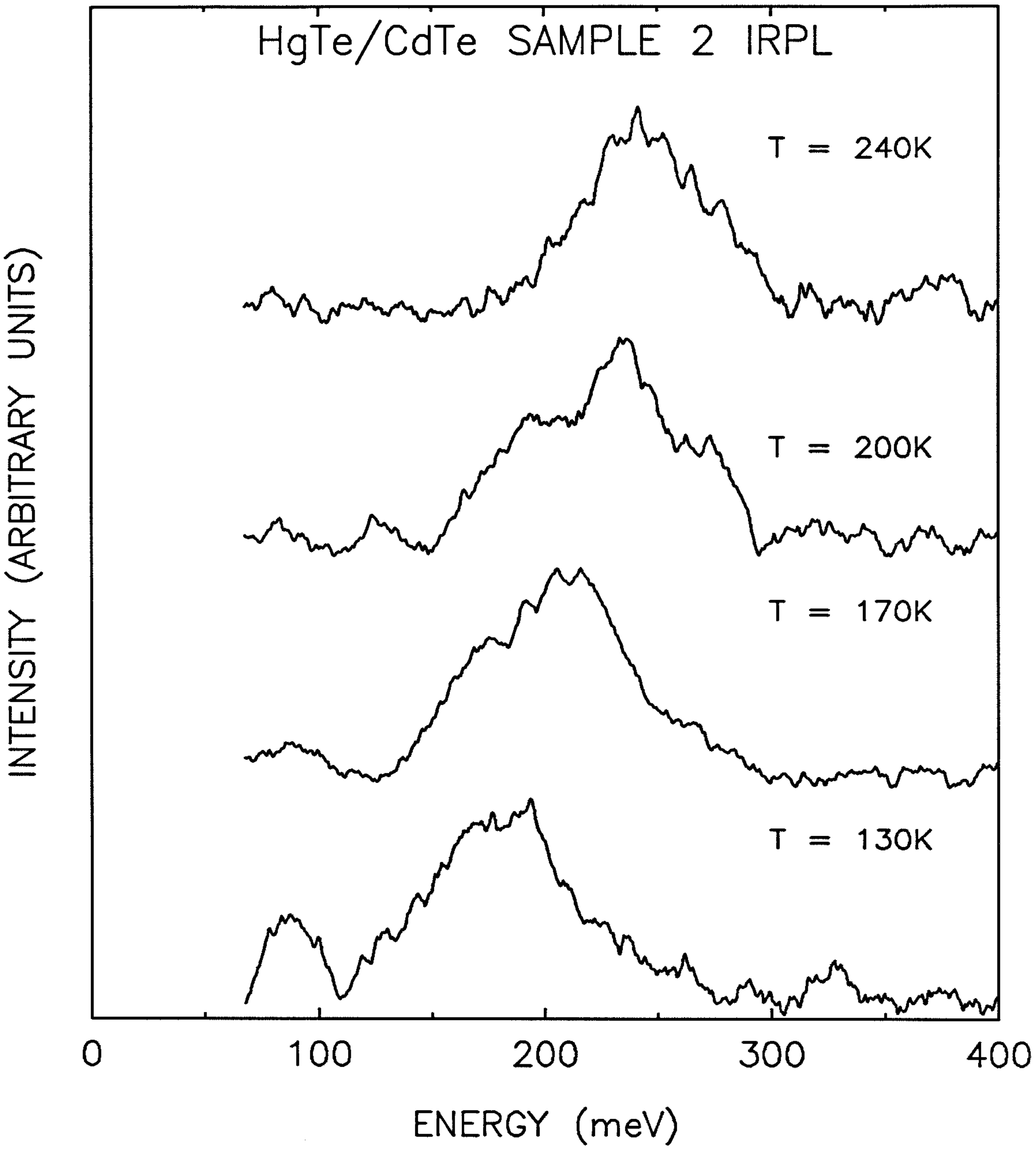

Figure 2.9: Infrared photoluminescence spectra from HgTe-CdTe superlattice sample 2. The sample temperature for each spectrum is at the right. The long wavelength cutoff of the optical response of the system is near 73 meV (17 μm). Each spectrum is plotted on a different vertical scale.

2.4.4 HgTe-CdTe sample 1 temperature dependence

Figure 2.10 shows the temperature dependence of the IRPL from HgTe-CdTe superlattice sample 1. The circles indicate the energy of the peak in the photoluminescence intensity, while the bars indicate the energies of the points where the luminescence intensity is one-half the peak intensity. We were unable to observe luminescence at temperatures lower than 80 K since the peak wavelength shifted beyond the cutoff of the optical system at 73 meV (17 μm). The solid line gives the band-gap energy for a $Hg_{0.67}Cd_{0.33}Te$ alloy,[16] which would have the same average Cd concentration as sample 1. It is clearly evident that the peak energy for the luminescence from the superlattice is lower than that for the alloy. This difference is strong evidence for sample 1 being a superlattice. A limited study of the pump power dependence of the luminescence was made at high sample temperatures, and no change in the lineshape was observed. However, given the narrow range of pump powers available and the signal-to-noise ratio, a small change might not have been discernible.

2.4.5 HgTe-CdTe sample 2 temperature dependence

Figure 2.11 is a similar plot of the temperature dependence of the luminescence from HgTe-CdTe superlattice sample 2. Also included is a curve showing the band-gap energy for a $Hg_{0.50}Cd_{0.50}Te$ alloy,[16] which would have the same average Cd concentration as sample 2. The luminescence peak from sample 2 is clearly at lower energy than that for the alloy band gap. There is also a considerable difference in the temperature dependences — the band gap of a 50% Cd $Hg_{1-x}Cd_xTe$ alloy shows almost no temperature dependence. This is evidence that sample 2 is a superlattice. The position of the low energy peak is not plotted here, nor did its peak position show any temperature dependence. It was not possible to determine whether this peak was related to the superlattice. No

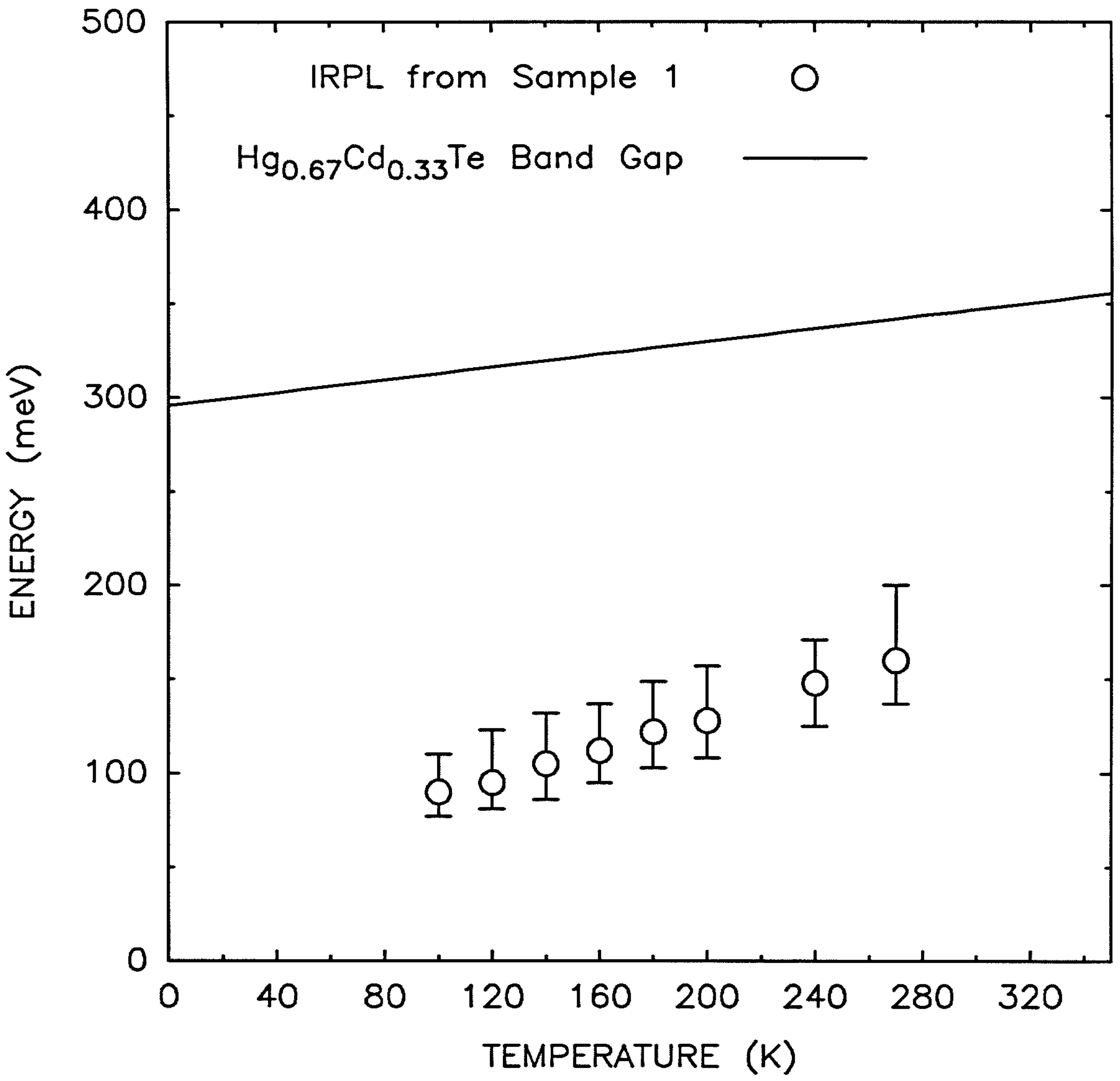

Figure 2.10: Temperature dependence of the infrared photoluminescence signal from HgTe-CdTe superlattice sample 1. The circles indicate the energy of the peak signal, while the bars indicate the energies of the half-intensity points. The solid line gives the band-gap energy for a $Hg_{0.67}Cd_{0.33}Te$, which has the same average Cd concentration as sample 1.

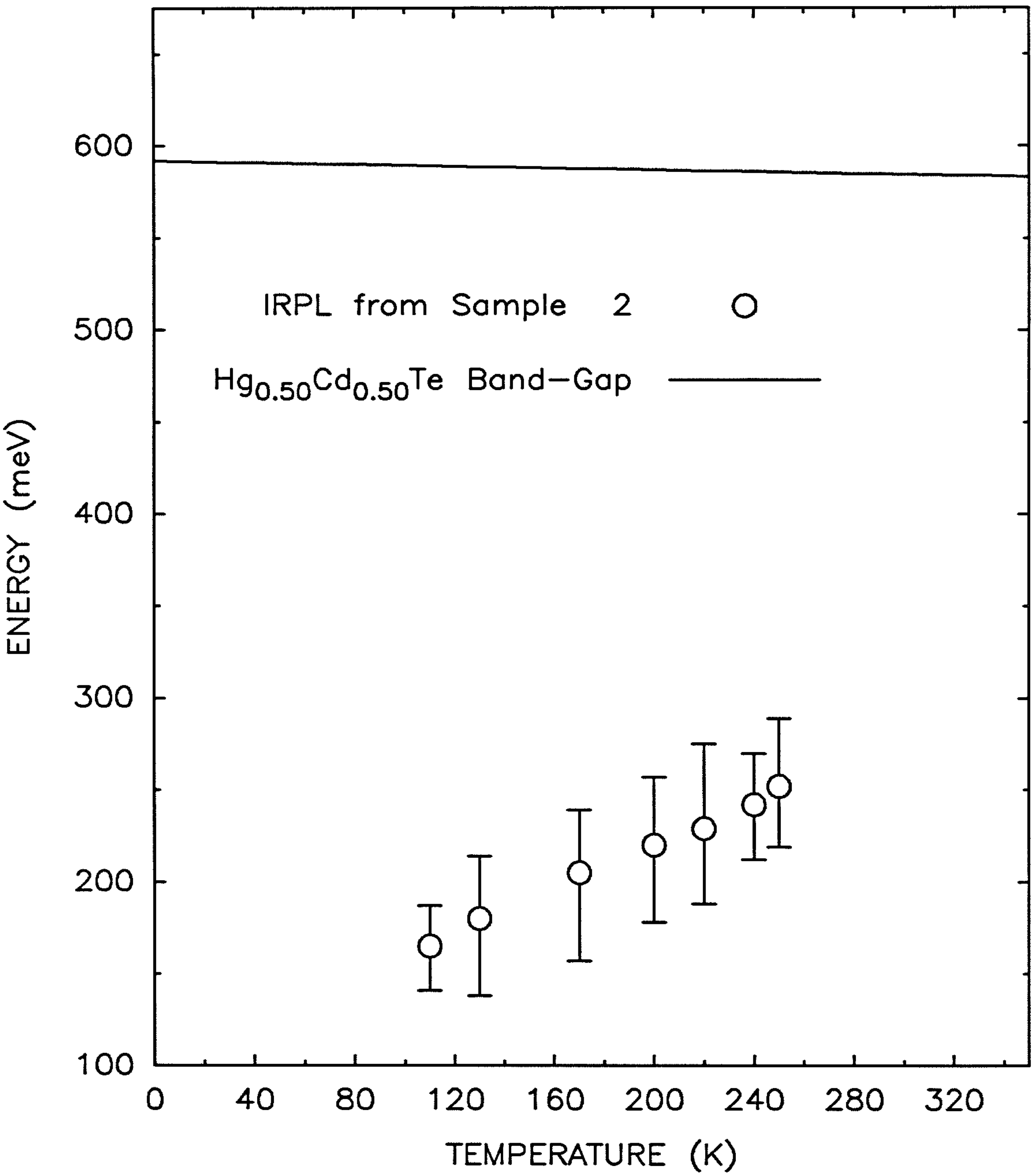

Figure 2.11: Temperature dependence of the infrared photoluminescence signal from HgTe-CdTe superlattice sample 2. The circles indicate the energy of the peak signal, while the bars indicate the energies of the half-intensity points. The solid line gives the band-gap energy for a $Hg_{0.50}Cd_{0.50}Te$, which has the same average Cd concentration as sample 2.

study of the pump power dependence of the luminescence was made due to the low signal strength from the sample (the spectra were taken at the high power limit of the laser).

2.4.6 Signal origins

To insure that the peaks in the IRPL spectra from the superlattices originated from the superlattices and not the substrates, both samples were turned over and the substrates irradiated with the same laser. The laser wavelength was greater than the band-gap energies of either of the substrates, ensuring that the superlattices would not be illuminated. Neither substrate showed a peak in the 73 – 500 meV energy range. The luminescence observed at energies above 500 meV could all be attributed to the substrates. Another way to be sure that the signals are from the superlattices and not the substrates is via the temperature dependence. The band-gap energies of both substrates decrease with increasing temperature, while the luminescence peak energies from the superlattices increase with increasing temperature.

2.4.7 Substrate luminescence

The luminescence from both substrates was measured to identify the signals related to the substrates. The experimental setup used was similar to that in Fig. 2.1, except an S-1 curve photomultiplier with the usual photon counting electronics was used for the 0.5 – 1.2 μm range, instead of the solid-state detector using synchronous detection. In each case, the substrate side of the samples was illuminated with the 6471 Å line of a Kr ion laser. The absorption depth for this wavelength of light in the substrates was less than 1 μm in both cases, avoiding the possibility of exciting the superlattices (the substrates were both roughly 1 mm thick). The substrate for sample 1 was $Cd_{1-x}Zn_xTe$, with a stated

Zn concentration of roughly 4%. The substrate for sample 2 was CdTe. The luminescence data in the near-band gap range for both substrates is shown in Fig. 2.12.

Both samples exhibit strong acceptor-bound exciton lines near their respective band gaps. The weak lines toward the high energy side of the large peaks represent the free exciton lines and excited states of bound excitons. The luminescence from the substrate of sample 2 is typical of bulk-grown CdTe. The main bound exciton peak occurs at 1589 meV. The peaks on the low energy side of the main bound exciton peak have all been observed before, and include LO phonon replicas of the main bound exciton line, donor-acceptor luminescence and phonon replicas of to donor-acceptor lines. The large peak near 1473 meV has been seen before in CdTe,[17,18] and has been attributed recombination of an exciton at an isoelectronic oxygen trap.[18] This line is usually accompanied by a series of LO phonon replicas to lower energy, due to the strong LO phonon coupling of defects in CdTe. This series is evident in the spectrum, showing 3 replicas.

The luminescence from the substrate of sample 1 is shown in the lower trace of Fig. 2.12. The band gap for CdTe at 6 K is 1605 meV, while the gap for ZnTe at 6 K is 2380 meV. As expected, the band gap of the CdZnTe substrate is greater than that of CdTe. The main bound exciton peak occurs at 1613 meV, 24 meV higher in energy than that for the CdTe substrate. All the lines present in this spectrum appear to be analogs of lines previously observed in CdTe. There is a common series of photoluminescence lines in CdTe, with the no-phonon line occurring att 1449 meV, and up to seven phonon replicas to lower energy, commonly referred to as the 1.42 eV band.[19] The periodic structure in the 1470 – 1550 meV range corresponds to this 1.42 eV band in CdTe. The difference in the energies of the lines may be attributed to the larger band gap of $Cd_{1-x}Zn_xTe$, and the accompanying change in the binding energies of the impurities involved.

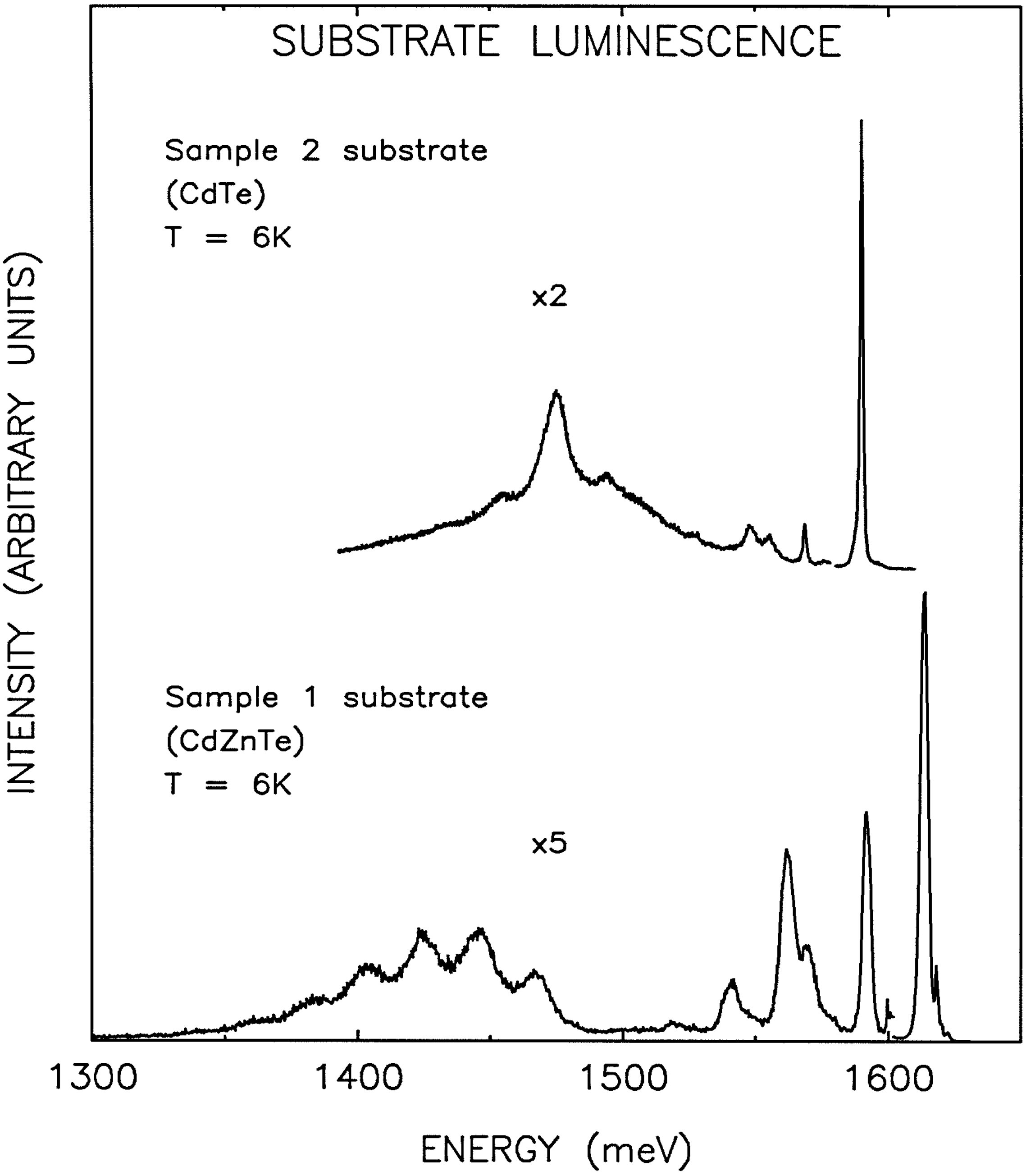

Figure 2.12: Luminescence from the superlattice substrates. The substrates were illuminated directly with the 6471 Å line of a Kr ion laser. The upper curve is from the substrate of sample 2, and shows typical CdTe luminescence. The lower curve is from the substrate of sample 1, and shows luminescence typical of low-Zn concentration CdZnTe.

The luminescence from this substrate was compared with a $Cd_{1-x}Zn_xTe$ sample with a 4.5% Zn concentration. The luminescence was very similar, and the differences could all be attributed to differences in the band-gap energies (caused by differences in the Zn concentration), or to the presence of different defects. Luminescence from this substrate was also observed through through the superlattice as well, and no difference was observed. For both samples, the luminescence in the 1.65 – 3 μm range was all attributed to the substrates.

2.5 Interpretation

2.5.1 Luminescence processes

In order to gain a better understanding of the properties of the superlattices, it is important to determine the process or processes producing the luminescence. The luminescence spectra from sample 1 (see Fig. 2.9) exhibit asymmetrical lineshapes which are narrower at lower sample temperatures. This behavior is suggestive of a process involving a thermal distribution of the charge carriers before recombination. One possibility for the superlattice luminescence signal is the recombination of electrons and holes near the respective band edges. In this case, it is possible to describe the resulting luminescence lineshapes theoretically, and compare them to the superlattice luminescence. Two possible schemes for band-to-band and near band-gap recombination are discussed below, and the lineshapes are compared with spectra from HgTe-CdTe sample 1. The signal-to-noise ratios of the spectra from sample 2 are considerably lower than those from sample 1, limiting the usefulness of such fits in this case.

Wave-vector conserving recombination

In most semiconductors, the recombination of electrons and holes proceeds via wave-vector conserving transitions. There are a number of possible sources for such luminescence in a semiconductor at high temperatures. The two most likely sources are band-to-band recombination and free exciton recombination. In band-to-band recombination, an electron in the conduction band may recombine with a hole in the valence band. When carriers are excited into the conduction and valence bands, the coulomb attraction between the electron and hole can give rise to a free exciton. The electron and hole in the exciton recombine by conserving wave-vector. The HgTe-CdTe superlattice luminescence is expected to be due to one of these processes. In GaAs-$Ga_{1-x}Al_xAs$ superlattices, free exciton recombination is the dominant source of luminescence at low temperatures,[20,21] while at higher temperatures band-to-band luminescence is the dominant process.[22] In either case, the luminescence lineshape will be similar.

The lineshape for such wave-vector conserving transitions is described below. Since a photon has negligible wave-vector, the energy of the electron and the hole are both fixed for a given emitted photon energy (see Fig. 2.13). Thus the density of states at a given photon energy may be expressed as a joint density of states for both bands, $g(h\nu)$. The intensity of emitted radiation at an energy $h\nu$ is given by

$$I(h\nu) = \begin{cases} P_e(E_c)P_h(E_v)g(h\nu) & E \geq E_g \\ 0 & E < E_g, \end{cases} \tag{2.1}$$

where $P_e(E_c)$ is the probability of an electron occupying a state with energy E_c, and $P_h(E_v)$ is the probability of a hole occupying a state with energy E_v. If the bands are assumed to be parabolic, then the joint density of states is given by

$$g(h\nu) = A(h\nu - E_g)^{1/2}, \tag{2.2}$$

where A is independent of the photon energy.[23] $g(h\nu)$ behaves like the density of states for a band whose effective mass is the reduced mass of the electron and

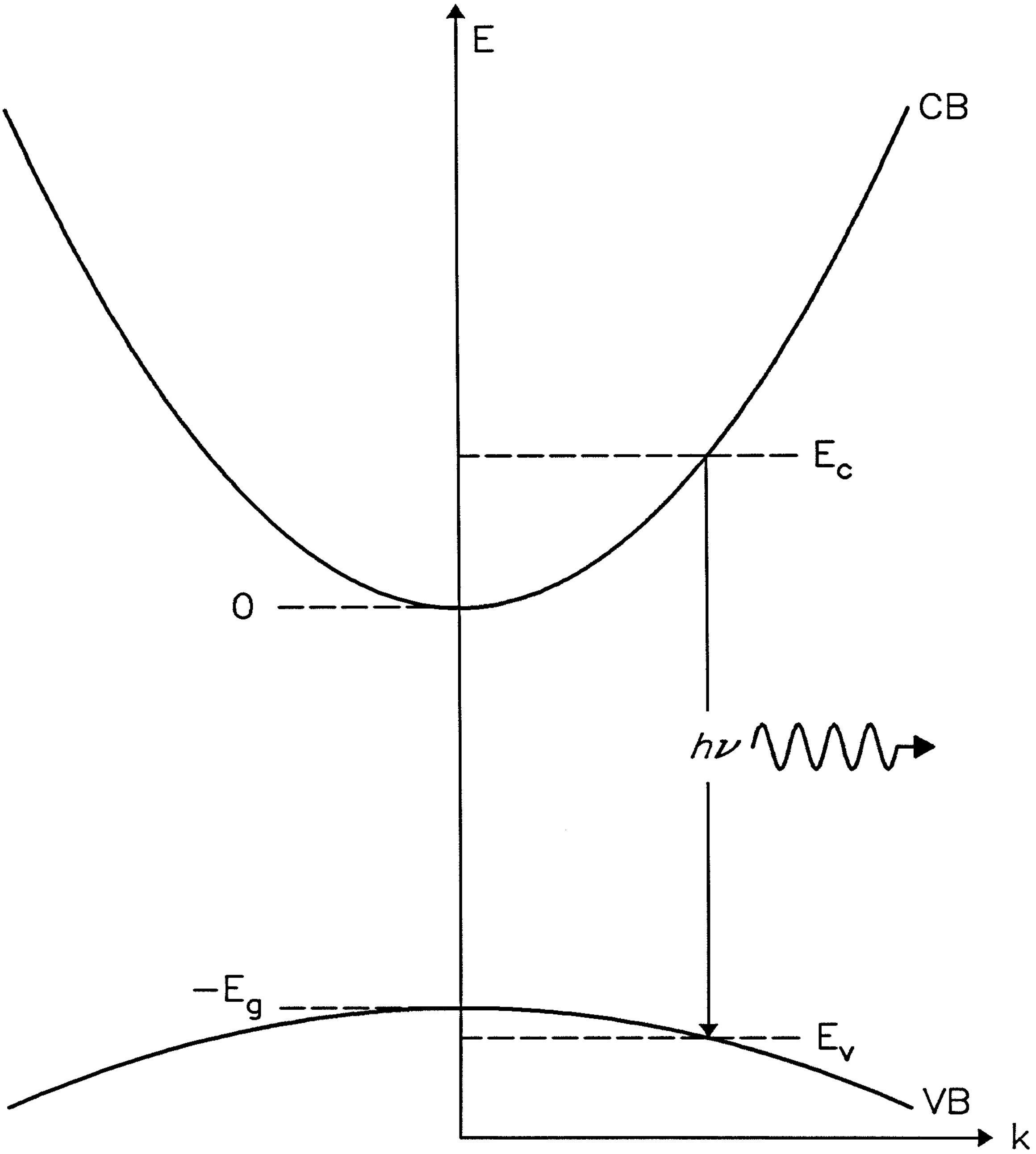

Figure 2.13: Band-to-band photoluminescence diagram. $h\nu$ is the energy of the photon emitted by the recombination. The energy is measured using the conduction band minimum as the origin.

hole effective masses. The occupation probabilities are given by the Fermi-Dirac functions

$$\begin{aligned} P_e(E_c) &= \frac{1}{1+e^{(E_c-\mu_e)/k_BT}} \\ P_h(E_v) &= \frac{1}{1+e^{(-E_v+\mu_h)/k_BT}}, \end{aligned} \tag{2.3}$$

where μ_e and μ_h are the electron and hole chemical potentials, respectively. k_B is the Boltzmann constant, and T is the sample temperature. The electron and hole energies are known functions of the photon energy

$$\begin{aligned} E_c &= \frac{m_r}{m_e}(h\nu - E_g) \\ E_v &= \frac{m_r}{m_h}(E_g - h\nu), \end{aligned} \tag{2.4}$$

where m_e and m_h are the electron and hole effective masses respectively, and m_r is the reduced mass of m_e and m_h.

This distribution is fairly complicated, but it has two interesting limits. In the limit of low carrier concentration and high temperature (non-degenerate limit), the occupation probabilites can be replaced by simple Boltzmann factors, leaving

$$I(h\nu) = C(h\nu - E_g)^{1/2}e^{(E_g-h\nu)/k_BT}. \tag{2.5}$$

The constant C will be a function of the carrier concentration, but it will only affect the amplitude, not the lineshape. The peak position as a function of temperature is given by

$$h\nu_{peak}(T) = E_g(T) + \frac{1}{2}k_BT, \tag{2.6}$$

where $E_g(T)$ is band-gap energy at the temperature T. Thus the peak position of such luminescence will shift to higher energy at a rate of $\frac{1}{2}k_B$ faster than the band gap. If the carrier concentration generated by the laser is small compared to the thermal occupation of the bands, then this approximation will hold. In this limit, changing the laser power by a small amount will not affect the lineshape. The other limit where the intensity expression simplifies is in the limit of high carrier concentration (degenerate limit). In this limit, the electron and hole chemical potentials can be treated as a free-electron fermi gas, and are proportional to $n^{2/3}$. The luminescence lineshape is then a strong function of the carrier concentration. Thus a small change in the laser power will result in a significant change in the lineshape. In the intermediate region, the chemical potentials are described by Fermi integrals, complicating the analysis.

Figure 2.14 shows the least-squares fit of the non-degenerate limit of wave-vector conserving recombination (long-dashed line) to the 270 K spectrum from HgTe-CdTe sample 1. The temperature was fixed for the fit, and the free parameters used were the band-gap energy, E_g, and the amplitude. Thus the amplitude and the width are coupled at a given temperature. The band-gap value determined from this fit was 143 meV. The use of the non-degenerate limit is justified by the lack of pump-power dependence of the luminescence lineshape, and the high sample temperatures. Such fits were made to the spectra at other temperatures, and the results were similar in each case. The general shape of the luminescence is suggestive of a wave-vector conserving process, however the luminescence linewidth is wider than that predicted by this model. This width may be attributable to fluctuations in the superlattice layer thicknesses. The result of such fluctuations would be a superposition of a range of band gaps, broadening the observed luminescence line width.

Superlattice layer fluctuations

It is quite likely that there are fluctuations in the superlattice layer thicknesses, across the sample horizontally or vertically. There has been much research into this phenomenon in GaAs-$Ga_{1-x}Al_xAs$ superlattices, where the luminescence linewidths have been ascribed to fluctuations in the layer thicknesses.[20-22,24] Each of these references attributes the widths to thickness fluctuations within

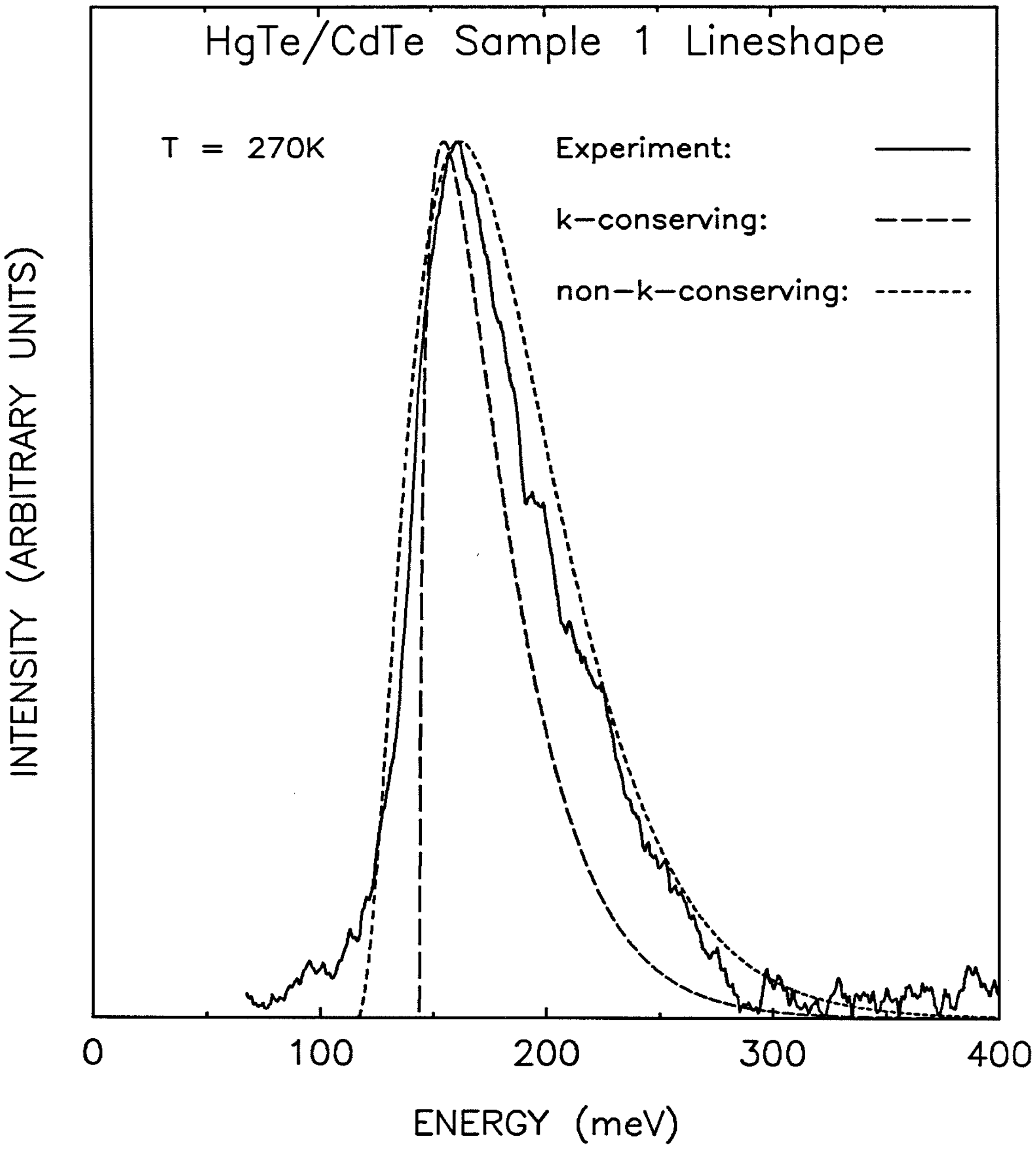

Figure 2.14: IRPL spectrum from HgTe-CdTe sample 1, with two luminescence lineshape fits. The solid curve is a 270 K IRPL spectrum from HgTe-CdTe sample 1. The long-dashed curve is the least-squares fit to the case of wave-vector conserving recombination in the non-degenerate limit. The short-dashed curve is the least-squares fit to the case of non-wave-vector conserving recombination in the non-degenerate limit.

the layers, as opposed to thickness fluctuations along the direction of growth. This conclusion was based on the degree of control of the layer-to-layer growth rates, and the lack of control over the growth in the plane of the layers, as well as by analysis of the resulting linewidths. In the high temperature photoluminescence study, the luminescence linewidths were observed to be larger for the samples with thinner layer thicknesses.[22] This increase was attributed to the increased effect of small layer thickness fluctuations for such samples. The width was shown to be up to a factor of four wider than that due to the thermal distribution of the carriers.

The observed linewidth of sample 1 at 270 K is a 1.5 times as wide as that predicted for wave-vector conserving recombination. This compares favorably with the GaAs-$Ga_{1-x}Al_xAs$ results. Thus it seems quite likely that the luminescence from sample 1 is due to wave-vector conserving recombination, and that there is some degree of fluctuation in the layer thicknesses.

Non-wave-vector conserving recombination

In some semiconductors, electrons in the conduction band can recombine with holes in the valence band without conserving wave-vector. There are a number of mechanisms which can relax the wave-vector conservation. If the carrier concentration is sufficiently high, carrier-carrier scattering can relax the conservation. In alloy materials like $Hg_{1-x}Cd_xTe$, scattering from disorder in the crystal can also cause relaxation of wave-vector conservation. However, it is difficult to find a mechanism to relax wave-vector conservation in HgTe-CdTe superlattices. Such recombination is not common in other superlattices, and the superlattice should not exhibit the large degree of disorder present in the alloys. Also, the luminescence lineshape showed no dependence on pump power, indicating the carrier concentration is too low to relax wave-vector conservation.

Even though this mechanism is not justifiable for the HgTe-CdTe superlattices studied here, it is instructive to compare this case with the luminescence, since there is evidence for this process in $Hg_{1-x}Cd_xTe$ alloys.[25]

In this non-wave-vector conservating scheme, an electron in the conduction band can recombine with any hole in the valence band. The intensity of the luminescence can be written as

$$I(h\nu) = A \int P_e(\epsilon) P_h(\epsilon) D_e(\epsilon) D_e(\epsilon) d\epsilon, \tag{2.7}$$

where $D_e(\epsilon), D_h(\epsilon)$ are the density of states in the conduction and valence bands, respectively. If the energy origin is chosen according to Fig. 2.13, the result is

$$I(h\nu) = A \int_0^{h\nu - E_g} \frac{\epsilon^{1/2}(h\nu - \epsilon - E_g)^{1/2}}{\left[1 + e^{(h\nu - \epsilon - E_g + \mu_j)/k_B T}\right]\left[1 + e^{(\epsilon - \mu_e)/k_B T}\right]} d\epsilon, \tag{2.8}$$

where k_B is the Boltzmann constant, and T is the sample temperature.[25] Again, μ_e and μ_h are the electron and hole chemical potentials, respectively. It has been assumed that the conduction and valence bands are parabolic. This lineshape simplifies greatly in the limit of low carrier density and high temperatures (non-degenerate limit). The Fermi-Dirac functions in the denominator then come out of the integral, resulting in

$$I(h\nu) = C(h\nu - E_g)^2 e^{(E_g - h\nu)/k_B T}. \tag{2.9}$$

Again, the carrier concentration affects only the magnitude, not the width of the lineshape. The luminescence peak position as a function of temperature is given by

$$h\nu_{peak} = E_g(T) + 2k_B T, \tag{2.10}$$

where $E_g(T)$ is the band-gap energy at the temperature T. Thus, the luminescence peak position will shift to higher energy at a rate of $2k_B$ greater than the band-gap energy.

The least-squares fit of the non-degenerate limit lineshape to the 270 K spectrum from HgTe-CdTe sample 1 is shown in Fig. 2.14 on page 53 as the short-dashed line. The band-gap value determined from the fit was 116 meV. Similar fits were obtained from the spectra at other temperatures. The agreement between the data and the fit might look good, however it is too wide. The full-width at half-maximum intensity of the observed luminescence at 270 K is 65 meV, while the width of the fit is 79 meV. This extra width is significant, and it occurs for fits to spectra at other temperatures. It is very difficult to find a mechanism for narrowing the observed superlattice luminescence linewidth, especially since any fluctuations in the layer thicknesses would increase the observed linewidth. Therefore it is very unlikely that the luminescence from HgTe-CdTe superlattice sample 1 is due to non-wave-vector conserving recombination.

Wave-vector conserving processes

As mentioned above, there are two important wave-vector conserving processes which have been observed in GaAs-$Ga_{1-x}Al_xAs$ superlattices. Given the limited range of temperatures for which luminescence spectra are available, it is difficult to make a definitive determination of the luminescence process. It is much easier to determine luminescence process with data at low temperatures, where thermal effects are minimized. However, there is much to be learned from the high temperature luminescence data. The temperature dependence of the peak position of the luminescence is quite linear, and only a single peak is visible at all the temperatures studied. This indicates that only one process is responsible for the luminescence in this temperature range. If either the electron or hole is in a bound state before recombination, the binding energies of the states must be at least 23 meV for it to produce luminescence at 270 K. Given the absence of a peak due to a second process, the binding energy would have to be even greater. (If it is assumed that a second process would be visible if it were 10% as probable as the main process, then the binding energy of bound state would have to be at least 46 meV.)

In most III-V compounds the free exciton binding energy is usually a few millivolts. It has been shown that the free exciton binding energy in III-V superlattices can be increased by two-dimensional confinement effects, and free excitons have been observed in room temperature absorption data.[26] This increase in the binding energy is caused by an increase in the electron effective mass in the superlattices. The electron effective mass for HgTe-CdTe superlattice sample 1 is 0.02 m_e parallel to the layers and 0.009 m_e normal to the layers, while the heavy hole effective mass is expected to be about 0.5 m_e.[27] This suggests a binding energy of only a few meV, which would not be large enough to allow free excitons to be observed at these high temperatures. Therefore, free exciton luminescence is probably not the source of the luminescence from sample 1. This conclusion could be confirmed if luminescence data were available at low temperatures, which should show the presence of free exciton recombination.

There are other processes leading to near-band-gap luminescence. It is possible for excitons to bind to neutral impurities (bound excitons). The binding energy for bound excitons is typically 2-3 meV in low Cd concentration $Hg_{1-x}Cd_xTe$ alloys.[25] This luminescence would disappear at temperatures above 30–40 K. There is no evidence to suggest that the binding energies of bound excitons in superlattices are significantly larger than those in the constituent materials. Therefore, it is unlikely that the luminescence from HgTe-CdTe sample 1 is due to bound excitons.

In bulk semiconductors, it is possible to have recombination where either the electron or hole, or both, are bound to impurities. Such impurity luminescence has been reported in GaAs-$Ga_{1-x}Al_xAs$ superlattices.[28] The luminescence was observed only at low temperatures, and exhibited different behavior than impurity luminescence in bulk semiconductors. This effect is expected for superlattices, since the binding energies for impurities depend on the position of the impurities within the layers.[29] A simple model for impurity luminescence is given in Ref. 30. Given the high temperatures studied for sample 1, it is unlikely that the luminescence is impurity related.

The luminescence spectra from sample 1, taken over a range of 100 to 200 K, show only a single peak, whose position is a linear function of the temperature. This indicates that a single process is responsible for the luminescence over the entire temperature range. The high sample temperatures imply that neither the electron nor hole are in bound states proir to the recombination. This is compatible with high temperature luminescence data from GaAs-$Ga_{1-x}Al_xAs$ superlattices, where processes involving bound electrons or holes are observed only at lower temperatures. Analysis of the lineshape fits agrees with this conclusion, and indicates that the luminescence process conserves wave-vector. Therefore it may be concluded that the luminescence from HgTe-CdTe sample 1 is due to wave-vector conserving band-to-band recombination.

HgTe-CdTe sample 2 luminescence

As can be seen from Figs. 2.8 and 2.9, the luminescence linewidths of sample 2 are much broader than those from sample 1 at all temperatures. The observed signal strength from sample 2 was lower than that from sample 1 as well. The temperature dependence of the peak positions indicates that this sample is a superlattice. The luminescence peak position occurs at significantly lower energy than that of a 50% Cd $Hg_{1-x}Cd_xTe$ alloy, and shifts to higher energy with increasing temperature at a rate of 0.59 meV/K. This shift is much larger than that of $Hg_{1-x}Cd_xTe$ alloys, even those whose band-gap energies are similar to those of sample 2.

There are a number of possibilities for the increased linewidth and lower signal strength from sample 2. As mentioned above for sample 1, it is possible that there are spatial fluctuations in the layer thicknesses of this sample. Given the large widths of the luminescence peaks (74 meV at 170 K), this possibility seems quite likely. Although the linewidth fluctuates from scan to scan, a comparison of the observed linewidths with those expected for wave-vector conserving recombination shows the luminescence to be roughly a factor of 2 to 3 wider than predicted by the theory. These widths compare favorably with those observed in some GaAs-$Ga_{1-x}Al_xAs$ superlattices, indicating that layer thickness fluctuations are the probable source of the increased widths. There are other possibilities which may account for the lower signal strength. The small thickness of the superlattice ($\sim 7500\,Å$) might be expected to produce less luminescence than sample 1. If the carrier lifetime were sufficiently long to allow the carriers to diffuse a significant fraction of the superlattice thickness before recombining, then the integrated luminescence intensity would depend upon the total thickness of the sample. Also, it is possible that the layer thickness fluctuations play a greater role in the luminescence from this sample, perhaps lowering the luminescence efficiency as well as increasing the linewidth.

2.5.2 Comparison with theory

A simple theory for calculating the band-gap energies of HgTe-CdTe superlattices is presented in Refs. 11 and 30. This theory is more complicated than the Kronig-Penney model discussed in Chapter 1. The Kronig-Penney model is essentially a one-band approximation, where the superlattice conduction band energy is determined by considering only the spatial variations in the conduction band energy from one material to the other. This method works satisfactorily for GaAs-$Ga_{1-x}Al_xAs$ superlattices, but the situation for HgTe-CdTe superlattices is more complicated. In CdTe, the conduction band has s-like symmetry and the valence band has p-like symmetry, which is common for most wide-gap semiconductors. In HgTe, however, both the conduction and valence bands have p-like symmetry. It is this difference in the symmetries of the HgTe and CdTe conduction bands that precludes the use of a simple one-band approximation for the superlattice states. The model developed by G. Bastard in Refs. 11 and 30 is a two-band approximation, which includes effects due to mixing of the s-like and p-like states which make up the bands. This model makes simple calculations of the band-gap energies possible for a wide range of superlattice parameters, and agrees well with more involved calculations.[27] However, this model only predicts the band-gap energies of superlattices at 0 K.

Guldner et al. introduced temperature dependence into the model by using the temperature-dependent band-gap energies for HgTe and CdTe.[31] The band-gap energies for HgTe and CdTe at the chosen temperature are used as the paramters for use in the model developed by Bastard. The end result is an approximation to the temperature dependence of the superlattice band gap. This model is sensitive to the band-gap values used for the constituent materials. Unfortunately, there are discrepancies in the literature on the temperature-dependent band gaps of HgTe and CdTe. These differences can change the predicted superlattice band-gap energies by up to 10 meV, as well as changing the temperature dependence. For this study, the temperature-dependent band-gap values used for HgTe and CdTe were obtained from the empirical $Hg_{1-x}Cd_xTe$ temperature dependent model of Ref. 16, applied for the cases of $x = 0$ and $x = 1$. While the model was stated to be valid for these values, it predicted the 0 K band gap of CdTe to be 1.645 eV, while the more commonly accepted value is 1.608 eV.[32,33] The use of these values was not ideal, but it provided a good enough approximation for comparison with the data.

Theoretical predictions for sample 1

Figure 2.15 shows how the luminescence data from sample 1 compare with the predictions of this theoretical model. An offset of 40 meV between the valence-band maxima of HgTe and CdTe, with HgTe higher, was used for the calculations. This seems to be the most commonly accepted value,[34,35] although the evidence is not conclusive. Since both superlattices were grown on (111)-oriented substrates, the actual layer thicknesses should be discrete multiples of the lattice constant along this direction (3.73 Å). For both samples, it was assumed that the total layer thickness and the total number of layers were known. Given the stated layer thicknesses for sample 1 (40 Å HgTe and 20 Å CdTe), the nearest layer numbers are 11 layers of HgTe (41 Å) and 5 (18.7 Å) layers of CdTe. If the luminescence were due to a wave-vector conserving band-to-band process, then the actual band gap would be near the low energy threshold of the luminescence peak. However, as Table 2.4 and Fig. 2.15 show, the temperature-dependent Bastard theory for these layer thicknesses predicts too large a band gap. The luminescence lies between the energies predicted for 12/4 layers of HgTe/CdTe and for 13/3 layers of HgTe/CdTe. Assuming the luminescence is due to band-to-band recombination, the best fit to the data from sample 1 is provided by 13 layers of HgTe (48.5 Å) and 3 layers of CdTe (11.2 Å), and is plotted in Fig. 2.15. For these layer thicknesses, the theory gives values of 68.3 meV for the band gap at 100 K, and 114 meV at 240 K. Experimentally, the low energy threshold at 100 K is about 75 meV, and at 240 K the threshold is at 110 meV, so the observed band-gap energy is somewhat greater than that predicted by the theory for these layer thicknesses. If a linear fit is made to the peak positions for the IRPL from sample 1, the slope obtained is 0.42 meV/K. The theory predicts a slope of

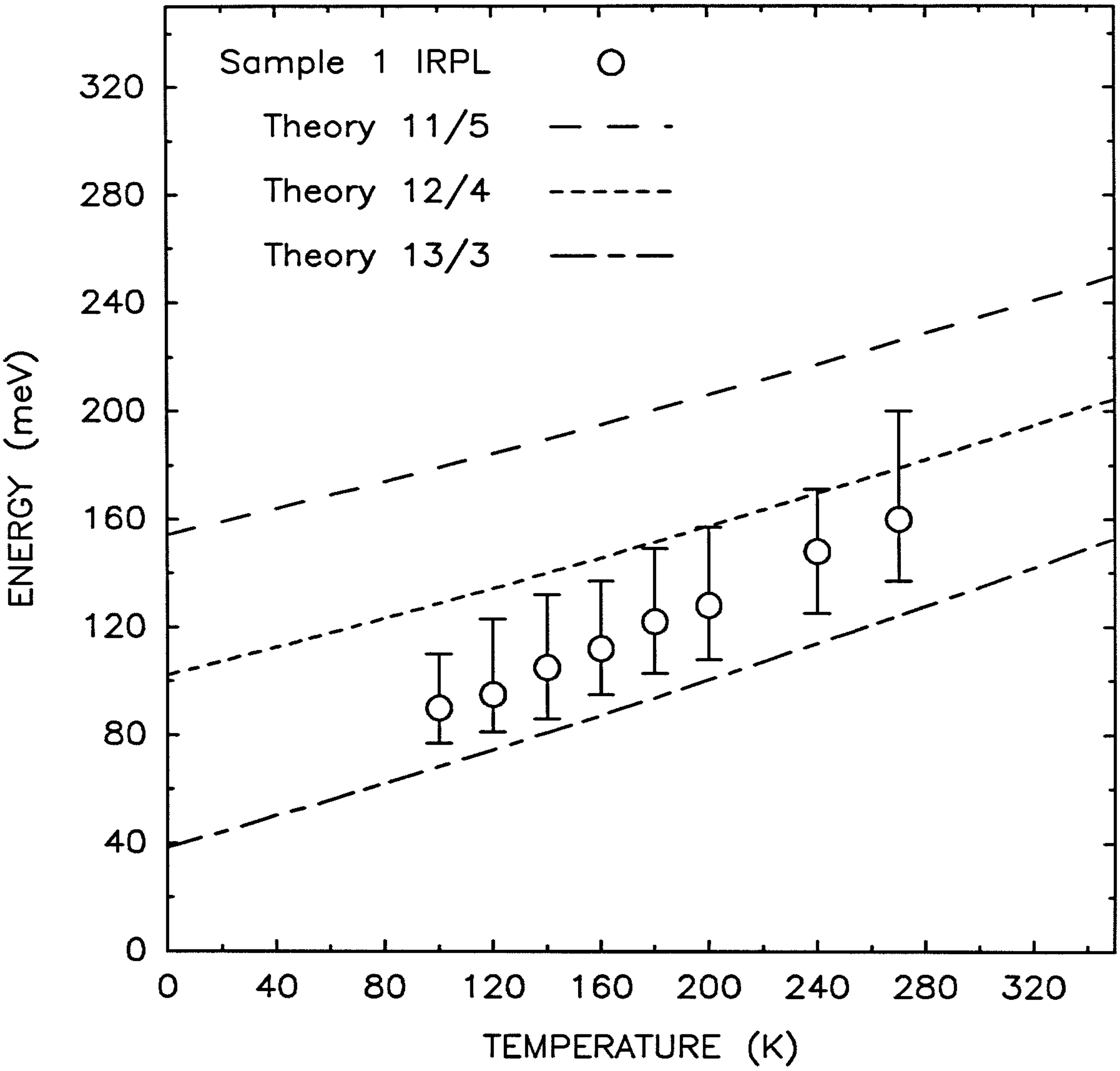

Figure 2.15: Comparison of the HgTe-CdTe superlattice sample 1 data with the temperature-dependent Bastard model. The circles represent the IRPL peak positions for sample 1. The bars represent the full-widths at half-maximum intensity. The dashed lines are theoretical curves, where the number of HgTe/CdTe atomic layers is given in each case.

0.33 meV/K, which is $1k_B$ less than the shift of the peak. This is greater than the value expected for wave-vector conserving band-to-band recombination. The agreement is fairly good given that the temperature-dependent band gaps used for HgTe and CdTe are not precise. Using different estimates of the HgTe and CdTe band gaps from the literature, the predicted superlattice band gaps can be changed by up to 10 meV. Therefore, it is best to conclude only that the observed superlattice band gap falls between those predicted by the theory for 12/4 and 13/3 layers of HgTe/CdTe. If the theory is accurate, this implies an error of 24 to 40% in the measurment of the CdTe concentration. Such an error is possible given that the individual layer thicknesses were measured only by calibrated values of the source fluxes.

Theoretical predictions for sample 2

Figure 2.16 shows how the luminescence data from sample 2 compare with the predictions of this theoretical model. Given the stated layer thicknesses for sample 2 (50 Å HgTe and 50 Å CdTe), the closest number of atomic layers are 13 each of HgTe and CdTe (48.5 Å). The theoretical predicition for this combination of layer thicknesses is plotted in Fig. 2.16 as the long-dashed line. Note that the slope of the luminescence data is much steeper than that predicted by the theory. Theoretical curves for two other compositions, 15/11 (56 Å/41 Å) and 17/9 (63.4 Å/33.6 Å) layers of HgTe/CdTe, are also plotted in Fig. 2.16. None of the curves seems to match the data very well, although they are all in the right energy range at some temperatures. In each case, the slope of the luminescence peak position is $4k_B$ greater than that predicted by the theory. (It is possible that this discrepancy is caused by the HgTe and CdTe band-gap values used in the theory.) The 0 K band gap for 17/9 layers of HgTe/CdTe is very close to the extrapolation of the luminescence peak position to 0 K. However,

Table 2.4: HgTe-CdTe Superlattice Results.

		Sample 1	Sample 2	Units
stated comp.[a]		40/20	50/50	Å
ave. Cd conc.[b]		33%	50%	
IRPL peak position vs. T[c]	0K intercept	46	102	meV
	slope	0.42	0.59	meV/K
equivalent HgCdTe alloy[d]	0K band gap	296	592	meV
	slope	0.17	0	meV/K
— theory — stated layer thicknesses[e]	comp.	11/5	13/13	# layers
	0K band gap	154	172	meV
	slope	0.27	0.24	meV/K
— theory — best fit to the data[f]	comp.	13/3	17/9	# layers
	0K band gap	38	101	meV
	slope	0.33	0.24	meV/K

a. The HgTe/CdTe layer thicknesses given by the crystal growers.

b. The average cadmium concentration in the superlattice.

c. These values are from linear fits to the IRPL data.

d. An alloy with the same average Cd concentration as the superlattice.

e. The values for the HgTe/CdTe layer numbers closest to the stated thicknesses, from the Bastard model discussed in the text.

f. These values are the best fit of the Bastard model to the data.

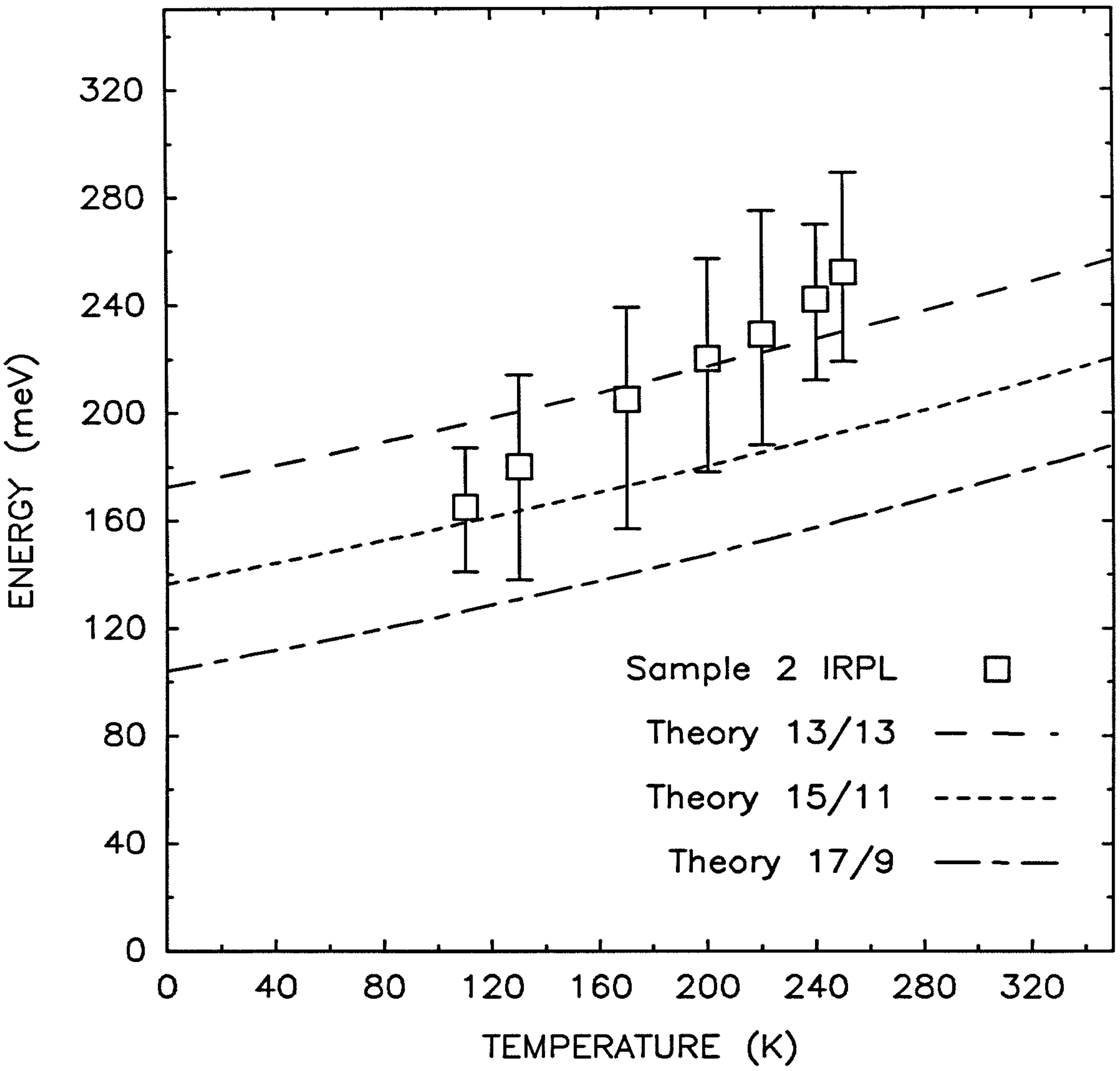

Figure 2.16: Comparison of the HgTe-CdTe superlattice sample 2 data with the temperature-dependent Bastard model. The squares represent the IRPL peak positions for sample 2. The bars represent the full-widths at half-maximum intensity. The dashed lines are theoretical curves, where the number of HgTe/CdTe atomic layers is given in each case.

it seems that any curve between 15/11 and 17/9 layers of HgTe/CdTe would provide a reasonable fit to the data. This would imply an error of 16 to 30% in the measurement of the average Cd concentration. It is also possible that associating the superlattice band-gap energy with the low energy threshold for the luminescence is not valid for this sample, since the lineshapes do not really resemble band-to-band recombination.

Limitations of the temperature-dependent Bastard model

There are a number of parameters which can affect the predictions of the temperature-dependent Bastard model. As discussed above, the band-gap values used for HgTe and CdTe can significantly affect the predictions of this model. Unfortunately, thare are no universally accepted values for either material. Given the range of data present in the literature, the choice of values can lead to a slight change in both the predicted band gaps, and the temperature dependence. Therefore, care should be exercised when comparing actual band-gap values and temperature dependences.

Another parameter which can change the theoretical predictions is the value of the energy offset between the valence band of HgTe and the valence band of CdTe. The band offset for this system has widely been assumed to be small, usually 40 meV.[34,35] Schottky barrier height measurements of HgTe-CdTe heterojunctions place an upper limit of roughly 500 meV on the value of the band offset. The band-gap energies predicted by the theory decrease with increasing band offset. In order to draw any conclusions about the band offset from IRPL measurements of HgTe-CdTe superlattices, it will be necessary to perform a systematic study of a number of superlattices configurations whose compositional properties are more well known.

It is also possible that strain effects play a major role in determining the band structure. The lattice constant of HgTe is 0.3% larger than that of CdTe, which means that HgTe-CdTe superlattices are always strained. Sample 1 was grown on a CdZnTe substrate whose lattice constant was between HgTe and CdTe, spreading the strain out between the CdTe and HgTe layers. Therefore, strain should not be very important in sample 1. Sample 2 was grown on CdTe; therefore, the strain would be contained in the HgTe layers. The effects of strain on HgTe-CdTe superlattices grown on CdTe have been investigated, and it does change the band structure.[38] The calculations have been performed only for a limited number superlattice configurations at 0 K, making it difficult to compare the results with the samples used here. However, the results indicate that strain may play an important role in the behavior of sample 2.

Finally, it is possible that there is some interdiffusion between the HgTe and CdTe layers. The effects of interdiffusion on the band gaps of HgTe-CdTe superlattices have been investigated, and the general result is an increase in the band gap over the value expected without interdiffusion.[35] It is not clear from the data that any interdiffusion has occured. Such a determination might be made possible by annealing a sample in stages, and observing the changes in the luminescence.

2.6 Conclusions

The results of the first infrared photoluminescence measurements of HgTe-CdTe superlattices were presented here. The temperature dependence of the IRPL spectra of two different superlattices from different sources was measured. In each case the luminescence was shown to occur at significantly lower energies than that for $Hg_{1-x}Cd_xTe$ alloys with Cd concentrations equivalent to the average Cd concentration of the respective superlattices. The luminescence lineshapes from one of the samples were asymmetrical, and were also narrower at lower temperatures. Analysis of the lineshape led to the conclusion that the process producing the luminescence was wave-vector conserving band-to-band recombination. The band-gap energy of the superlattice would then be near the low energy threshold of the luminescence peak. A comparison of the data with photoluminescence measurements on III-V superlatices indicated the presence of small fluctuations in the superlattice layer thicknesses.

A comparison of the data with a temperature-dependent model of the band-gap energies showed good qualitative agreement with the theory. As predicted by the theory, the sample with the thicker CdTe layers had the large band gap. The direction of the temperature dependence was also predicted; however, in one case the magnitude of the change predicted was too small. This discrepancy may not be significant given the uncertainties in the parameters used in the theory. Good quantitative agreement between the theory and experiment was possible if the assumption of errors in the layer thickness measurements was made. Given the uncertainties in the parameters used in the theory and in the sample characterizations, the agreement between the theory and experiment was actually quite good.

The differences between the optical properties of the two superlattices prove that it is possible to tailor the properties of HgTe-CdTe superlattices. This is an important result, since it shows that the properties of superlattices are more adjustable than those of $Hg_{1-x}Cd_xTe$ alloys. The luminescence from the superlattice samples did not seem to show the impurity-related luminescence common to $Hg_{1-x}Cd_xTe$ alloys. This is typical of III-V superlattices as well, where the strength of impurity-related luminescence is much weaker than in the alloy compounds. This could mean that HgTe-CdTe superlattices will have electrical characteristics superior to those of $Hg_{1-x}Cd_xTe$ alloys. These reuslts indicate that HgTe-CdTe superlattices will become a very important infrared material.

After the IRPL experiments involving the two original superlattice samples were completed, similar experiments were performed on five other superlattice samples. No luminescence was observed from any of these samples, from 12 to 300 K. Some of the structures were grown with thick HgTe layers and thin CdTe layers (e.g. 27 layers of HgTe and 13 layers of CdTe). The temperature-dependent Bastard model predicted very small band gaps for these particular configurations. Therefore, it is possible that the luminescence from these samples occured at wavelengths longer than 17 μm, and were beyond the cutoff of the optical system. It would be useful to extend the range of the optical system to longer wavelengths, but as Table 2.2 shows, such materials are very difficult to work with and hard to obtain. It is possible that the other samples were not of sufficient quality to luminesce, although one of the samples showed signs of damage due to heating by the laser (probably the result of poor sample mounting.)

IR transmission and photoconductivty measurements were made on sample 1 using the FTIR. These experiments confirmed the soft absorption edge predicted for this sample. The absorption and photoconductivity did not become significant until well above the band gap obtained from the IRPL experiment, which is reasonable given the small thickness of this sample.

In order to obtain a better understanding of the photoluminescence and absorption in HgTe-CdTe superlattices, a systematic study of a number of superlattice configurations is necessary. This should help resolve questions concerning the theory as well. It would be better if the total superlattice thicknesses were greater than 2 μm, since this would increase the IR absorption to more managable levels. The thin samples studied here presented problems due to the low total absorption, and possibly also due to carrier diffusion. While superlattice thicknesses aproaching 2 μm have been reported,[9] greater thicknesses may not be easily attained. At the growth rates used for the superlattices studied here, the growth time for 2 μm of material is about 2 hours. At the growth temperatures used, about 180 °C, interdiffusion of the bottom layers during growth may present a limitation on the total thickness which can be obtained.

The current experimental results on HgTe-CdTe superlattices indicate that they should be well suited for work as infrared detectors. Aside from actually fabricating detectors, there are a number of useful optical experiments yet to be performed on the superlattices. Time resolved IRPL would be helpful in indentifying the luminescence process, and measuring the free carrier lifetimes. Raman scattering experiments should provide information on band offsets, layer thicknesses and carrier effective masses. HgTe-CdTe superlattices should prove to be rich field for research in the near future.

References

1. R. Dornhaus and G. Nimtz, in *Narrow Band Gap Semiconductors*, Springer Tracts in Modern Physics Vol. 98, (Springer-Verlag, Berlin, 1983).

2. M. B. Reine, A. K. Sood and T. J. Tredwell, in *Semiconductors and Semimetals*, edited by R. K. Willardson and A. C. Beer, Vol. 18 (Academic Press, New York, 1981).

3. See for example the articles in *Semiconductors and Semimetals*, edited by R. K. Willadrson and A. C. Beer, Vol. 18 (Academic Press, New York, 1981).

4. J. N. Schulman and T. C. McGill, *Appl. Phys. Lett.* **34**, 663 (1979).

5. D. L. Smith, T. C. McGill and J. N. Schulman, *Appl. Phys. Lett.* **43**, 180 (1983).

6. T. C. McGill, *Proceedings of the 17th International Conference on the Physics of Semiconductors*, San Francisco, 1984 (Springer-Verlag, Berlin, 1985) p. 375.

7. J. P. Faurie, M. Boukereche, J. Reno, S. Sivananthan and C. Hsu, *J. Vac. Sci. Technol.* **A3**, 55 (1985).

8. P. P. Chow and D. Johnson, *J. Vac. Sci. Technol.* **A3**, 67 (1985).

9. J. M. Ballingall, F. A. Ponce, G. B. Anderson, B. J. Feldman and W. J. Takei, *27th Electronic Materials Conference*, Boulder, Co. 1985.

10. C. E. Jones, T. N. Casselman, J. P. Faurie, S. Perkowitz and J. N. Schulman, *Appl. Phys. Lett.* **47**, 141 (1985).

11. G. Bastard, *Phys. Rev.* **B25**, 7584 (1982).

12. This sample was provided by Peter Bratt of the Santa Barbara Research Center. The anneal was also performed at SBRC.

13. For a good explanation of signal to noise in solid state detectors, see: S. M. Sze, *Physics of Semiconductor Devices*, (John Wiley and Sons, New York, 1981) pp. 743–748, or A. Yariv, *Introduction to Optical Electronics* (Holt, Rinehart and Winston, New York, 1976) pp. 309–314.

14. The SDL 2410-C laser diodes were chosen for their high CW output power, and their ability to be pulsed at high frequencies at a 50% duty cycle. They were designed to operate at room temperature, with a maximum CW output power of 100 mW. It was found that by cooling them to 77 K that the CW output power could be increased to near 500 mW.

15. A. V. Nurmikko and B. D. Schwartz, *J. Vac. Sci. Technol.* **21**, 229 (1982).

16. J. Chu, S. Xu and D. Tang, *Appl. Phys. Lett.* **43**, 1064 (1983).

17. J. P. Noblanc and G. Duraffourg, *Phys. Stat. Sol. (b)* **46**, 705 (1971).

18. N. V. Agrinskaya, G. I. Aleksandrova, E. N. Arkad′eve, B. A. Atabekov, O. A. Matveev, G. B. Perepelova, S. V. Prokof′ev and G. I. Shmanenkova, *Sov. Phys. Semicond.* **8**, 202 (1974).

19. There have been a large number of studies on this luminescence feature. See for example: T. Taguchi, J. Shirafuji and Y. Inuishi, *Osaka University Technical Report* **23**, 195 (1973).

20. C. Weisbuch, R. Dingle, P. M. Petroff, A. C. Gossard and W. Weigmann, *Appl. Phys. Lett.* **38**, 840 (1981).

21. D. C. Reynolds, K. K. Bajaj, C. W. Litton, P. W. Yu, W. T. Masselink, R. Fischer and H. Morkoç, *J. Vac. Sci. Technol. B* **3**, 694 (1985).

22. L. Goldstein, Y. Horikoshi, S. Tarucha and H. Okamoto, *Jpn. J. Appl. Phys.* **22**, 1489 (1983).

23. O. Madelung, *Introduction to Solid State Theory*, (Springer, Berlin, 1978) p. 269.

24. J. Singh, K. K. Bajaj and S. Chaudhuri, *Appl. Phys. Lett.* **44**, 805 (1984).

25. A. T. Hunter and T. C. McGill, *J. Appl. Phys.* **52**, 5779 (1982).

26. See for example: D. S. Chemla, D. A. B. Miller, P. W. Smith, A. C. Gossard and W. Wiegmann, *IEEE J. Q. E.*, **QE-20**, 265 (1984), or R. C. Miller, D. A. Kleiman, W. T. Tsang and A. C. Gossard, *Phys. Rev.* **B24**, 1134 (1981).

27. G. Y. Wu and T. C. McGill, private communication.

28. B. Lambert, B. Deveaud, A. Regreny and G. Talalaeff, *Solid State Commun.* **43**, 443 (1982).

29. C. Mailhoit, Y. C. Chang and T. C. McGill, *Phys Rev.* **B26**, 4449 (1982).

30. G. Bastard, *Phys. Rev.* **B24**, 4714 (1981).

31. Y. Guldner, G. Bastard and M. Voos, *J. Appl. Phys.* **57**, 1403 (1985).

32. M. H. Weiler, in *Semiconductors and Semimetals*, edited by R. K. Willardson and A. C. Beer, Vol. 16 (Academic Press, New York, 1981).

33. The value of 1608 meV agrees quite well with the value obtained from photoluminescence measurements on the substrate of sample 2 in this study. The temperature dependence given for CdTe in Ref. 32 was not used since it predicted the 300 K band gap of CdTe to be 1425 meV, while the majority of other references give a value closer to 1500 meV. This illustrates the problems associated with determining the band gaps of HgTe-CdTe superlattices.

34. Y. Guldner, G. Bastard, J. P. Vieren, M. Voos, J. P. Faurie and A. Million, *Phys. Rev. Lett.* **51**, 907 (1983).

35. J. N. Schulman and Y. C. Chang, *Appl. Phys. Lett.* **46**, 571 (1985).

36. T. F. Kuech and J. O. McCaldin, *J. Appl. Phys.* **53**, 3125 (1982).

37. M. B. Johnson, A. Zur, J. O. McCaldin and T. C. McGill, *J. Vac. Sci. Technol. B* **3**, 1260 (1985).

38. G. Y. Wu and T. C. McGill, *Appl. Phys. Lett.* **47**, 635 (1985).

Chapter 3

The 78-meV acceptor in GaAs

3.1 Introduction

3.1.1 Background

Recently, there has been considerable interest in using semi-insulating (SI) GaAs as a substrate for device fabrication. Devices are usually fabricated on GaAs by ion-implantation of dopant layers into a substrate. Ion-implantation produces damage in the material which must be annealed out before defining the device structures. Therefore it is necessary for the substrate to remain semi-insulating during the anneal.

In the past, GaAs was grown by the horizontal Bridgman technique in quartz crucibles. During growth, the material would incorporate silicon atoms from the crucible. Silicon is usually a donor in GaAs, and the material was made SI by compensating the silicon with chromium, which is a deep acceptor. Such material is not thermally stable, however, since the chromium can diffuse out of the substrate during annealing.

This problem led to the development of the liquid encapsulated Czochralski (LEC) growth method, which produces thermally stable, SI material.[1] The LEC method uses pyrolytic boron-nitride crucibles to eliminate the problem caused by silicon incorporation during growth. The semi-insulating behavior is due to a near mid-gap donor state which compensates the shallow acceptors (carbon is the most common) usually present in GaAs. However, it had been observed that if the melt stoichiometry became gallium rich during the growth process, the material turned out *p*-type.[2] This material lacked the deep donor level, so the conductivity was dominated by the shallow acceptors. Understanding the process producing this change is an important step in learning how to control the properties of LEC GaAs.

Studies of the *p*-type material have revealed that it posesses an acceptor level at 78 meV above the valence band, which is not present in the SI material.[3,4] Temperature-dependent Hall effect and photoluminescence measurements showed similar concentrations of the 78-meV acceptor and another acceptor at 200 meV above the valence band in the *p*-type material, while neither acceptor was present in appreciable quantities in the SI material.[5,6] While these measurements do not prove that a relationship exsists between the two levels, it has been suggested that this center is a double acceptor, with first and second ionization energies of 78 and 200 meV, respectively.[5–7] Given the dependence on stoichiometry, the anti-site Ga_{As} (a gallium atom occupying an arsenic site), or a complex involving this center and boron have been advanced as possible explanations.

3.1.2 Results of this work

This study is the first observation of the *s*-like excited states of a double acceptor in a semiconductor. The excited states of the 78-meV acceptor were measured using two different techniques: selective excitation luminescence (SEL) and electronic Raman scattering (ERS). Both of these techniques are sensitive to the detection of s-like excited states of acceptors, and are useful for identifying acceptors in bulk-grown semiconductors. The measurements made in this study showed that the $1s^1 2s^1$ excited state of the 78-meV acceptor in GaAs is split into two levels separated by 4.0 meV. An effective mass-like theory for a double acceptor in a semiconductor was proposed to account for the observed splitting. A comparison of the experiments with the double acceptor theory developed here and theoretical predictions for a single acceptor led to the conclusion that the 78-meV acceptor in GaAs is due to the first ionization of a double acceptor. This is the first direct evidence that the 78-meV level in GaAs is caused by a double acceptor.

The theory presented here is the first to predict the s-like energy levels of a double acceptor, including the splitting of the first s-like excited state. The theory predicts the s-like states of a double acceptor to be highly degenerate. It should then be possible to distinguish low-symmetry centers producing double acceptors by their s-like excited state spectra. The experimental techniques employed in this study are useful for identifying double acceptors in semiconductors, and should be applicable to many materials with band gaps in the near-infrared and visible. The application of novel tunable optical sources such as F-center lasers should extend the usefulness of these techniques to smaller-band gap materials like Si, and some III-V and II-VI compounds.

3.2 Experimental techniques

The p-like excited states of the 78-meV acceptor have been measured by infrared absorption.[4] However, p-like excited states do not give a strong indication of the valency of an acceptor. The binding energies of the p-like excited states relative to the valence band edge are nearly identical for simple single and double acceptors, since p-like excited states have little probability of being near the acceptor core. Thus, the hole binding energies for p-like excited states of single and double acceptors are nearly identical, as is the case in germanium.[8] The s-like excited states are expected to provide a better indication of the nature of an acceptor, since they experience the central part of the potential. The experimental techniques used in this study were chosen for their ability to detect transitions between s-like initial states and s-like final states.

3.2.1 Electronic Raman scattering

Electronic Raman scattering is useful for studying the excited states of acceptors in p-type material. It is therefore well suited to studying the 78-meV acceptor, which occurs predominately in p-type material. In such material, the acceptors are occupied by holes, and the donors are ionized (empty of electrons).

In the ERS experiment, a below band-gap photon in the crystal can decay into a virtual electron-hole pair. Either the electron or hole can interact with a hole bound to an acceptor. The bound hole can then be raised to an excited state of the acceptor. The virtual electron-hole pair can then recombine, emitting a photon. The energy of the scattered photon is given by

$$\hbar\omega_{scattered} = \hbar\omega_{laser} - (E_A - E_{A^*}), \tag{3.1}$$

where $\hbar\omega_{laser}$ is the incident photon energy. E_A is the binding energy of the acceptor ground state relative to the valence band, and E_{A^*} is the binding energy of the acceptor excited state relative to the valence band. Thus, the difference between the incident and emitted photon energies is the ground state to excited state energy difference of the acceptor. The donors are all ionized in p-type material; therefore, the ERS experiment will not detect donor excited states. The process of raising the bound hole to an excited state does not involve either the emission or absorption of a photon; therefore, transitions between s-like intial statesa and s-like final states are allowed.

3.2.2 Selective excitation luminescence

Selective excitation luminescence is useful for studying the excited states of acceptors in compensated material.[9,10] Compensated material has roughly equal numbers of donors and acceptors. In this case, the donors and acceptors are ionized — i.e., the donor states are occupied by holes and the acceptor states are empty of holes (Fig. 3.1a). It is easiest to understand this experiment by considering the behavior of the holes.

The SEL experiment involves using below band-gap radiation to promote a hole from a donor state to one of the excited states of an acceptor (Fig. 3.1b). The hole can then relax to the acceptor ground state (Fig. 3.1c). The relaxation process does not necessarily involve the emission of a photon. It could also be done via phonon emission or other non-radiative decay. It is therefore possible for the hole to relax from a $2S$ excited state to the $1S$ ground state. Finally, the hole relaxes back to the donor ground state, emitting a photon (Fig. 3.1d).

The energy required to excite a hole from a donor to one of the excited states of an acceptor is given by

$$\hbar\omega_{laser} = E_{gap} - E_D - E_{A^*} + \frac{e^2}{\epsilon R} + J^*(R), \tag{3.2}$$

where $\hbar\omega_{laser}$ is the energy of the incident photon, and E_{gap} is the band-gap energy. E_D is the donor binding energy relative to the conduction band edge and E_{A^*} is the binding energy of the acceptor excited state relative to the valence band edge. R is the distance between the donor and the acceptor, and ϵ is the static dielectric constant. The term

$$\frac{e^2}{\epsilon R}$$

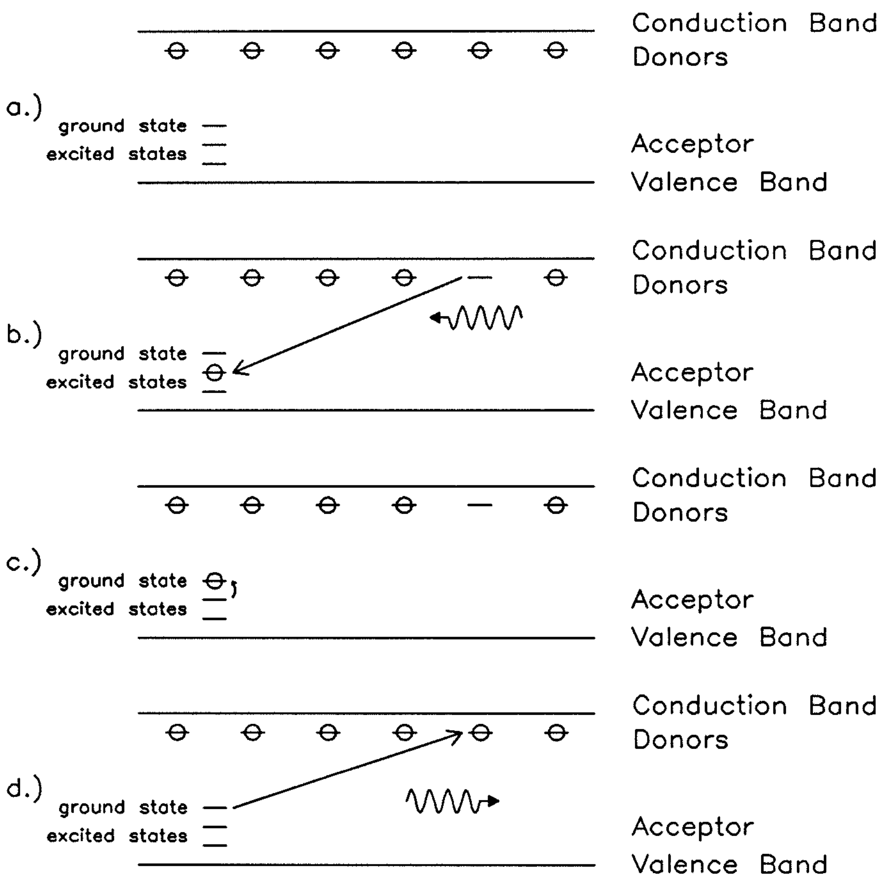

Figure 3.1: Schematic diagram of the processes involved in the SEL experiment. The locations of the holes are indicated by the circles. Only one acceptor is shown for clarity. The coulombic interaction between the donor and acceptor is not shown here.

a.) The initial configuration of the compensated material. All the donors are occupied with holes, and the acceptor is empty.

b.) Here an incident photon of the proper energy is absorbed, promoting the hole from a donor at distance R from the acceptor to an excited state of the acceptor.

c.) The hole relaxes to the acceptor ground state.

d.) The hole falls back to the donor, emitting a photon.

represents the coulomb interaction between the donor and the acceptor, screened by the static dielectric constant. The term $J^*(R)$ represents the non-coulombic interaction caused by overlap of the donor ground state and the acceptor excited state wave functions. When the hole relaxes back to the donor ground state, the energy of the emitted photon is given by

$$\hbar\omega_{emitted} = E_{gap} - E_D - E_A + \frac{e^2}{\epsilon R} + J(R). \tag{3.3}$$

E_{gap}, E_D, ϵ and R are the same as for eqn. 3.2. E_A is the binding energy of the acceptor ground state relative to the valence band edge. The term $J(R)$ represents the non-coulombic interaction between the donor and acceptor ground state wave functions.

If we ignore the non-coulombic interactions — these terms should be small at large pair separations — then the difference between the energies of the incident and emitted photons is

$$\Delta\hbar\omega = \hbar\omega_{laser} - \hbar\omega_{emitted} = E_A - E_{A^*}. \tag{3.4}$$

This is just the acceptor ground state to excited state energy difference. If a number of different laser energies are used for the spectra, then the photons from SEL processes will occur at fixed energy loss from the laser photon energy. This provides a means of distinguishing SEL processes from background luminescence processes, which would occur at fixed energy.

3.2.3 Applications

Both ERS and SEL have proved to be useful for identifying single acceptors in bulk-grown semiconductors.[11,12] In many semiconductors, the binding energy of an acceptor depends on the center producing it. For example, in GaAs the hole binding energy for a carbon acceptor is 26.0 meV, while that for germanium is 40.4 meV.[13] This breakdown of the effective mass approximation is called the central-cell shift.

In the effective mass approximation, the acceptor core is treated as a point charge in a dielectric medium. All acceptors would therefore have the same binding energy. In GaAs, the effective mass binding energy for an acceptor is 25.7 meV. In an actual semiconductor, this approximation is only valid far from the impurity center — the local potential near the center can deviate appreciably from coulombic. The heavy hole effective mass in GaAs is roughly $0.5m_e$, giving a Bohr radius for an acceptor of 13 Å in the effective mass approximation. The lattice constant of GaAs is 5.65 Å; therefore, a hole bound to an acceptor is easily affected by the short range perturbations of the lattice. The short range terms in the potential depend upon the actual center involved. In GaAs, for example, both carbon and germanium form acceptors if they occupy an arsenic site. One major difference between these two atoms is their size. A carbon atom is substantially smaller than a germanium atom. The difference in size will cause different local perturbations of the lattice, giving rise to different short range potentials. The short range potentials also depend on the site occupied by an acceptor. Zinc acceptors in GaAs on a gallium site have a binding energy of 30.7 meV,[13] which is quite different from the binding energy for a germanium acceptor on an arsenic site even though the atomic sizes are similar. The difference between the observed binding energy of an acceptor and that predicted by the effective mass approximation is called the central cell shift.

It is possible to identify the center responsible for producing an acceptor level by measuring the central cell shift. The higher-lying excited states of an acceptor have a much lower probability of being at the impurity center, therefore experiencing only the screened coulombic potential. The central cell shift can be determined experimentally by measuring the binding energies of the excited states relative to the acceptor ground state. Techniques such as the two-hole shift can be used to identify acceptors in selectively-doped, high-purity material.[14] The values from ERS and SEL experiments in bulk-grown material can then be compared to these results.

3.2.4 Experimental setup

The setup for both experiments is nearly identical (see Fig. 3.2). The 6471 Å line of a Coherent model CR-3000K krypton ion laser was used to optically pump a Coherent model 590 tunable dye laser. The below band-gap light was produced by either one of two carbo-cyanine dyes. DOTC was used for working near the GaAs band gap in the SEL experiment, and HITC was used for working beyond 8500 Å in the ERS experiment. The dyes were dissolved in DMSO (dimethyl sulfoxide), and ethylene glycol was added to increase the viscosity of the dye stream.[15] Tuning the dye laser was accomplished via a three-plate quartz birefringent filter which had been optimized for use in the 8500 – 9500 Å range. The tuning range for DOTC is given in the literature as 7500 – 8700 Å,[16] although only 7800 – 8400 Å was achieved in practice. The tuning range for HITC is given as 8300 – 9100 Å, but only 8400 – 8900 Å was obtained. One factor limiting the attainable tuning range was the selectivity of the birefringent filter, which had transmission orders roughly 700 Å apart. This, coupled with the gain curves for the dyes, limited the tuning ranges to about 600 Å. A different set of optimized optics was used for each dye. A resolution of 1.2 Å or better was usually achieved within the tuning ranges. The maximum tuned output power from the dye laser was frequently only 100 mW with an input pump power of 5 W.

The laser light was then directed onto the sample, which was mounted in a Janis model DT-8 cryogenic dewar. The sample was immersed in liquid helium pumped below the lambda point. There are a number of advantages to this: it

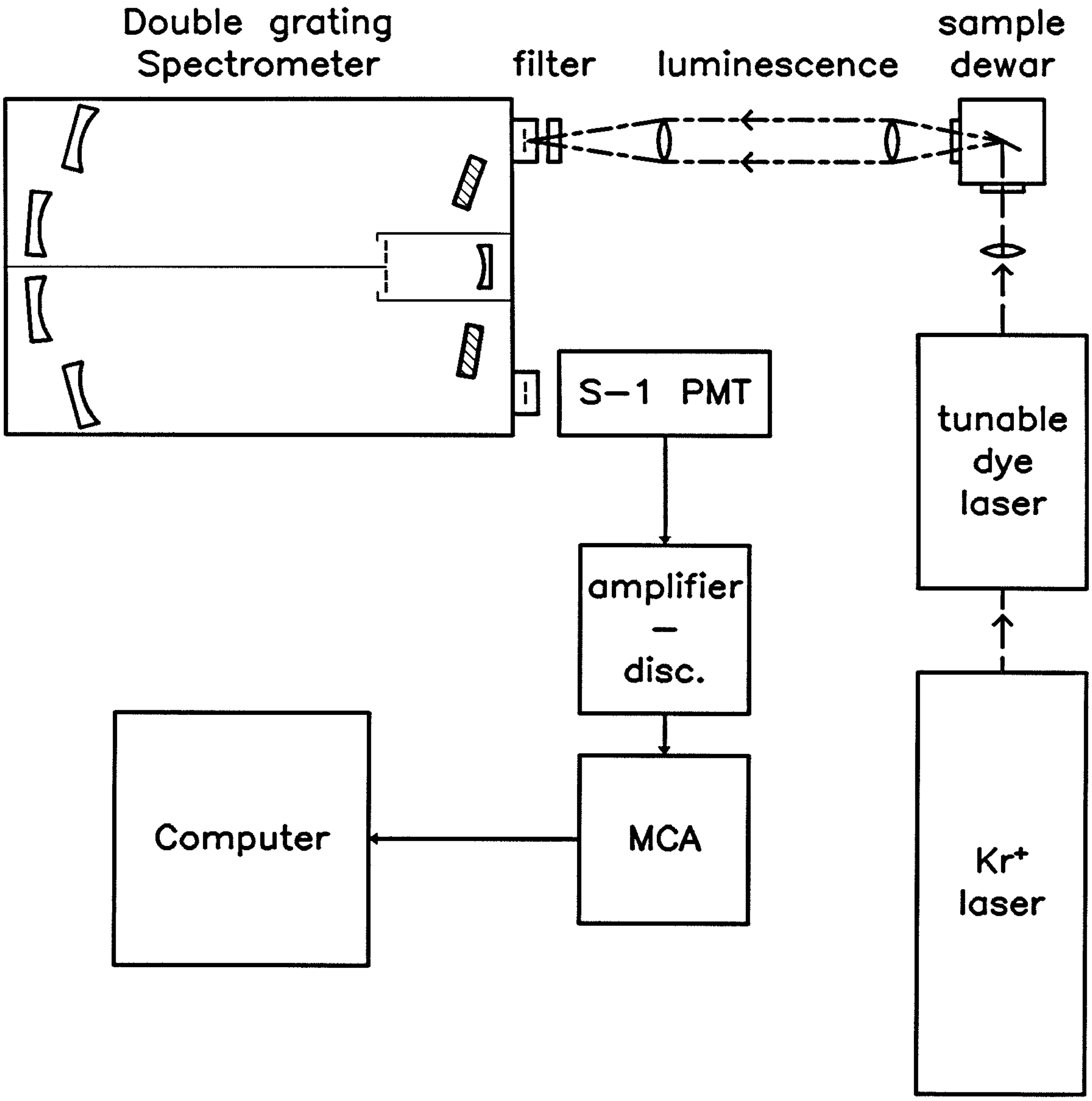

Figure 3.2: Schematic diagram of the setup for the SEL and ERS experiments. The infrared laser dyes used were DOTC for SEL, and HITC for ERS.

achieves a very low temperature (typically 1.8 K), the temperature is easily regulated by controlling the pumping speed, and there is very little optical scattering since the fluid does not boil.

The luminesence from the sample was directed into a Spex 1404 double grating spectrometer for spectral analysis. The gratings were blazed for 1.6 μm, and used in second order for maximum effeciency at 8000 Å. A long-wavelength pass filter was sometimes inserted before the spectrometer to eliminate stray room light. The collection optics consisted of a short focal length lens matched to the f-number of the dewar, and a second lens matched to the f-number of the spectrometer.

An S-1 curve photomultiplier tube cooled to 77 K was used as the detector. The long-wavelength response limit of the photomultiplier was about 1.2 μm, eliminating the need to filter out first-order light entering the spectrometer. The output from the photomultiplier was sent through a PAR model 1120 amplifier-discriminator and to a multi-channel analyzer for photon counting. The data from the multi-channel analyzer was then sent to a digital computer for analysis.

3.3 Sample descriptions

Two different liquid encapsulated Czochralski GaAs samples were used for this study. Both samples were grown *p*-type from As-deficient melts. Temperature-dependent Hall effect (TDH) measurements on sample 1 indicated $1.1 \times 10^{15}\,\mathrm{cm}^{-3}$ donor, $5.3 \times 10^{15}\,\mathrm{cm}^{-3}$ carbon and $8.1 \times 10^{15}\,\mathrm{cm}^{-3}$ 78-meV acceptor concentrations, making it ideally suited for the ERS experiment.

The SEL experiment required compensated material, which was achieved by neutron transmutation doping sample 2. In neutron transmutation doping the sample is bombarded with thermal neutrons, causing the reactions:

$$\begin{aligned} n + Ga &\rightarrow Ge^{+} + \gamma + e \\ n + As &\rightarrow Se^{+} + \gamma + e. \end{aligned} \tag{3.5}$$

Selenium will always be a donor, and germanium will usually be a donor unless it sits on an arsenic site (Ge_{As}). The neutron filtering during the transmutation doping was not perfect, and it allowed some hot neutrons to hit the sample. This, along with the γ emission, caused damage to the sample.

Neutron transmutation doping of sample 2 added $3.8 \times 10^{15}\,\mathrm{cm}^{-3}$ Se and Ge donors, plus additional damage related donors. The concentrations of the transmuted atoms were calculated from the neutron flux incident on the sample and the respective neutron capture cross sections for gallium and arsenic. The sample was given a partial anneal at 580 °C for 1 hour. Temperature-dependent Hall effect measurements on a non-irradiated sample adjacent to sample 2 and given the same anneal gave concentrations of $2.6 \times 10^{15}\,\mathrm{cm}^{-3}$ donors, $7.4 \times 10^{15}\,\mathrm{cm}^{-3}$ carbon, and $3.6 \times 10^{16}\,\mathrm{cm}^{-3}$ 78-meV acceptors. The measurements on the non-irradiated sample showed the slope for carbon below 4.2 K, indicating that the 78-meV level was fully occupied at this temperature.[17] TDH measurements on a sample transmutation doped and annealed in a manner identical to sample 2 showed an 0.07 eV slope at 4.2 K, indicating that the 78-meV acceptor was partially compensated. There was a tradeoff here between annealing out the damage and compensating the 78-meV level. The damage lowers the luminescence efficiency, but annealing makes the material more *p*-type, which hinders the SEL experiment.

3.4 Results

3.4.1 Photoluminescence

The presence of the 78-meV acceptor was identified in samples 1 and 2 by photoluminescence and by temperature-dependent Hall effect measurements. Photoluminescence curves for both samples are shown in Fig. 3.3. The lower curve shows the photoluminescence from sample 1. At 1.9 K, the band gap of GaAs is 1520 meV.[18] The near-gap region around 1510 meV shows quite a bit of structure. Most of the lines in this region are believed to be excitonic in nature. The line at 1512.4 meV is due to an exciton bound to a carbon acceptor.[13] The line at 1507 meV is thought to be due to an exciton bound to the 78-meV acceptor, since it only occurs in material containing the 78-meV aceptor.[3] This assignment is in agreement with the rough estimate of the expected acceptor bound excition binding energy, which can be made as follows. The ratio of the acceptor bound exciton binding energy to the acceptor binding energy should be roughly constant, since they both should experience the central cell shift, although the exciton is affected to a lesser degree. The free exciton luminescence in GaAs occurs at 1515.5 meV at 4.2 K.[13] Thus, the binding energy of the carbon bound exciton is 3.1 meV. The acceptor binding energy for carbon in GaAs is 26 meV, thus the 78-meV acceptor is bound 3 times as strongly as carbon. A rough estimate of the 78-meV exciton binding energy is then 9.3 meV, giving a luminescence peak position of 1506.2 meV, which is close the the 1507 meV line observed in the photoluminescence.

The large feature at 1490 meV is related to the presence of carbon. The main peak is due to donor-acceptor luminescence, where a hole bound to a carbon acceptor recombines with an electron bound to a donor. The high energy shoulder is band-acceptor luminescence, where a hole bound to a carbon acceptor recombines

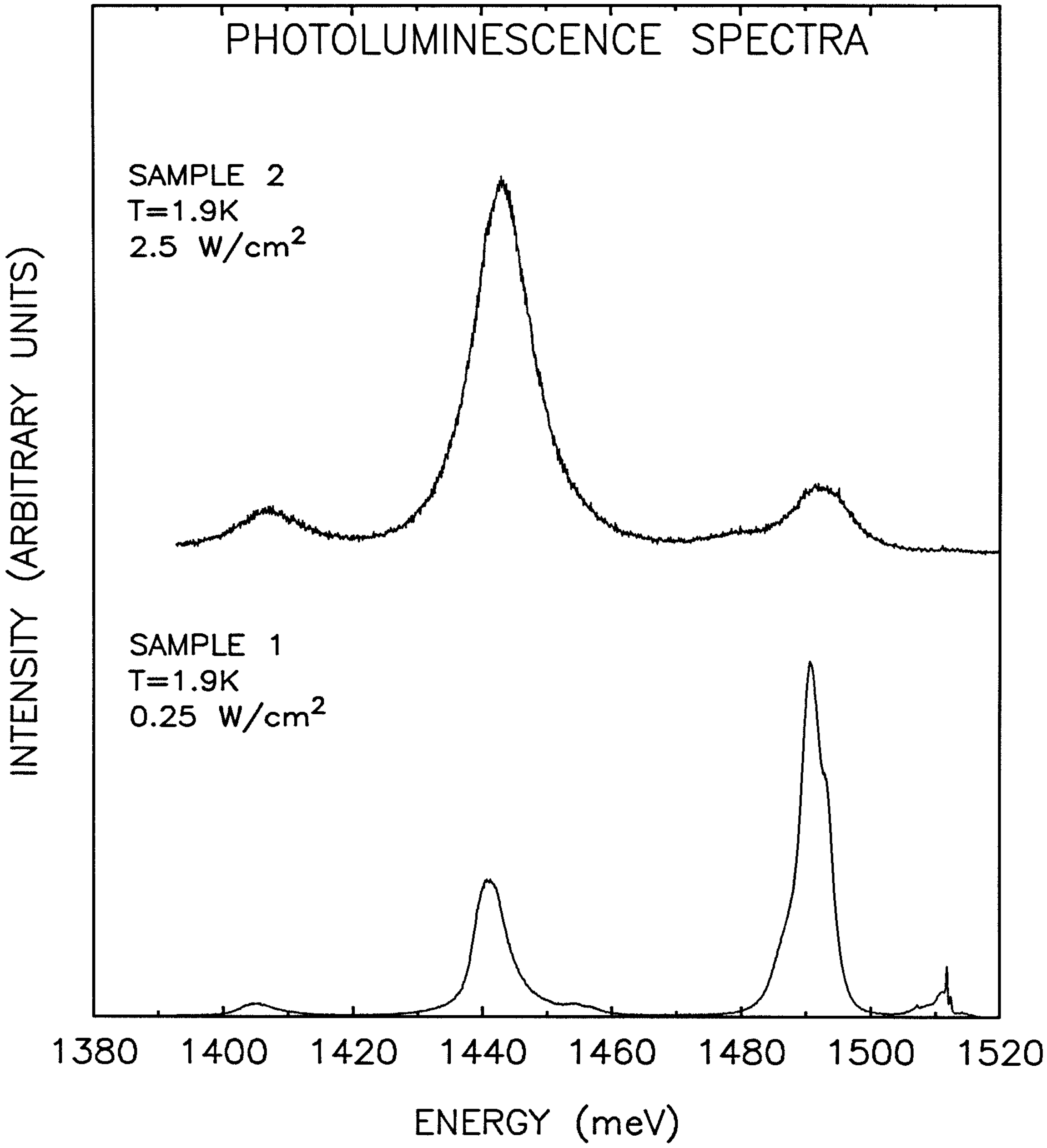

Figure 3.3: Photoluminescence spectra from samples 1 and 2. The photon energy for the luminescence is plotted against the intensity of the luminescence. The lower curve is from sample 1, and the upper is from sample 2. The two curves are not plotted on the same vertical scale. The excitation source was the 6471 Å line of a Kr$^+$ ion laser.

with an electron in the conduction band. The low energy shoulder has not been conclusively identified, although there is evidence suggesting it is due to donor-acceptor luminescence, where the acceptor is zinc. The photoluminescence peak energy for this shoulder is near that expected for zinc — 1488.8 meV.[13] There is also evidence in SEL and ERS data from sample 1 indicating the presence of zinc.

The weak feature at about 1457 meV is an LO phonon replica of the carbon donor-acceptor luminescence. In GaAs, the LO phonon energy is 36.5 meV;[19] thus, the LO phonon replica of a luminescence feature occurs at 36.5 meV toward lower energy than the main feature. The peak near 1441 meV is the donor-acceptor luminescence involving the 78-meV acceptor. The weak line near 1405 meV is the LO phonon replica of the 78-meV donor-acceptor luminescence. The relative intensities of the 1 LO phonon replicas of the donor-acceptor luminescence for the 78-meV acceptor and carbon, and their respective no-phonon lines indicate that the electronic transition of the 78-meV acceptor is more strongly coupled to the LO phonons.[3]

The upper curve in Fig. 3.3 shows the photoluminescence from sample 2. There is no evidence of the near-gap luminescence seen in sample 1, even though the optical pump power was 10 times that used for sample 1. This reflects the damage done to the crystal by neutron transmutation doping, which lowers the luminescence efficiency by providing paths for non-radiative transitions. The peak near 1494 meV is due to carbon donor-acceptor luminescence. The weak peak at 1480 meV may be donor-acceptor luminescence involving Ge acceptors — the expected peak photoluminescence peak energy is 1497 meV[13] — which could be produced by transmuting gallium atoms, with the resulting germanium atom occupying an arsenic site. This could be caused either by the transmutation of Ga anti-site defects (a suspected source of the 78-meV acceptor), or by displacement of the Ge atoms during transmutation doping. The peak at 1442 meV is due to donor-acceptor luminescence from the 78-meV acceptor. The peak near 1405 meV is the LO phonon replica of the 78-meV donor-acceptor luminescence.

The peak position of the 78-meV donor-acceptor luminescence occurs at slightly different energies in the two samples. This is indicative of the problems associated with identifying acceptors by photoluminescence in bulk-grown GaAs. A measurement of the excited state binding energies provides a more precise identification.

3.4.2 SEL and ERS

The SEL results for sample 2 for three different laser excitation energies are shown in Fig. 3.4. Two transitions are evident in the SEL data, one at 62.5 meV (line A) and one at 66.5 meV (line B). The broad background in the spectra is due to donor-acceptor luminescence from the 78-meV acceptor. The ERS results for sample 1 for two different exciting laser energies are shown in Fig 3.5. Three peaks are visible in the ERS data: line A at 62.9 meV, line B at 66.9 meV and line C at 72.9 meV. Lines A and B appear shifted about 0.4 meV toward greater energy loss in the ERS data than in the SEL data. This may be expected since any non-coulombic interaction between the donor and acceptor wave functions in the SEL experiment would tend to shift the measured energies from the actual binding energies. The energies obtained in ERS; however, are a direct measurement of the actual binding energies. Line C was not seen in the SEL experiment.

The two lines, A and B, occur only in material containing the 78-meV acceptor. Figure 3.6 compares ERS spectra from sample 3, which does not contain the 78-meV acceptor, with that from sample 1. There is no in indication of lines A or B in sample 3, which does not contain the 78-meV acceptor. This suggests

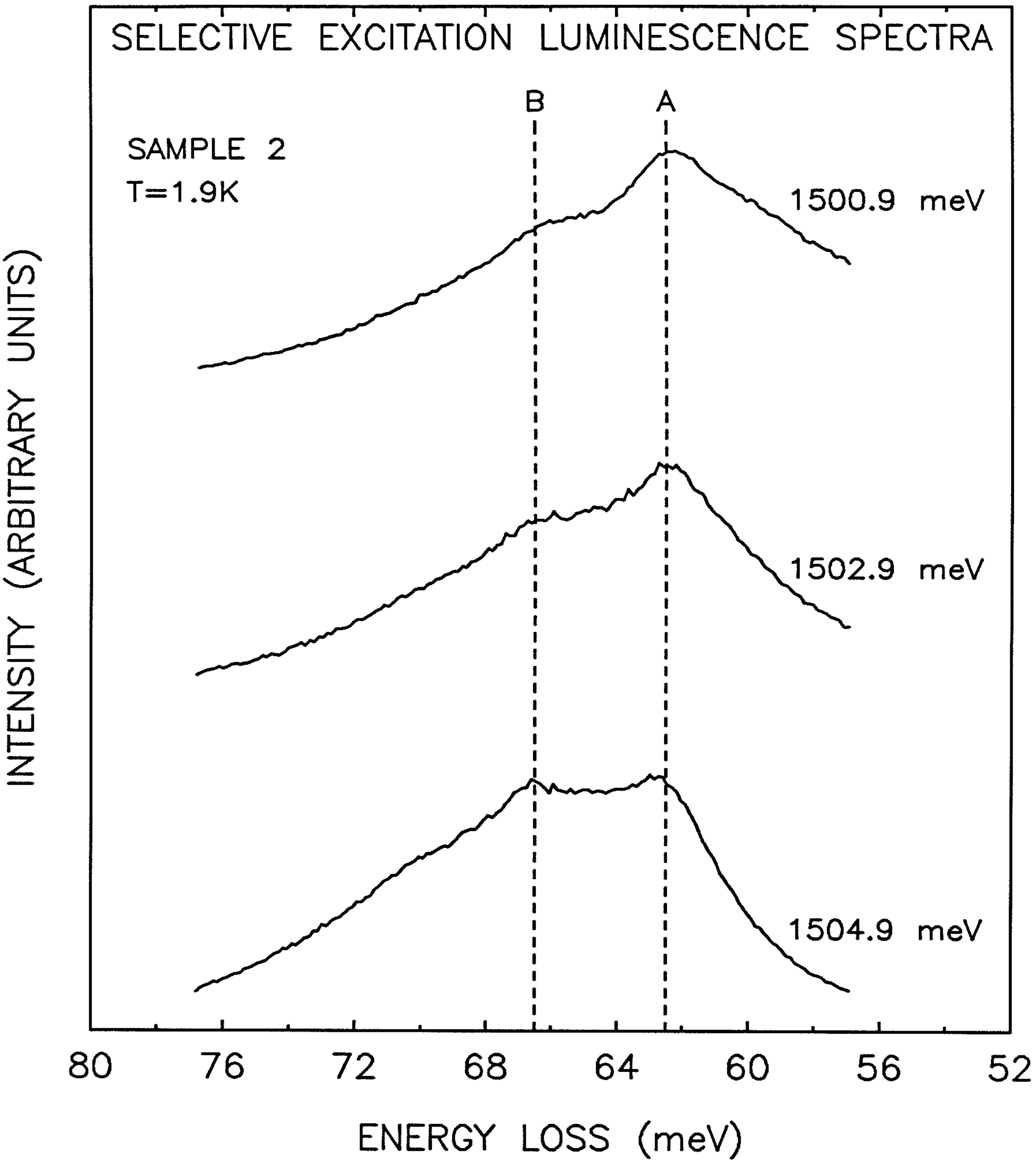

Figure 3.4: Selective excitation luminescence spectra from sample 2. Intensity of the emitted light is plotted against the difference between the emitted photon energy and that of the laser. Three different laser energies were used to distinguish between SEL features and background processes. The laser photon energy for each spectrum is at the right.

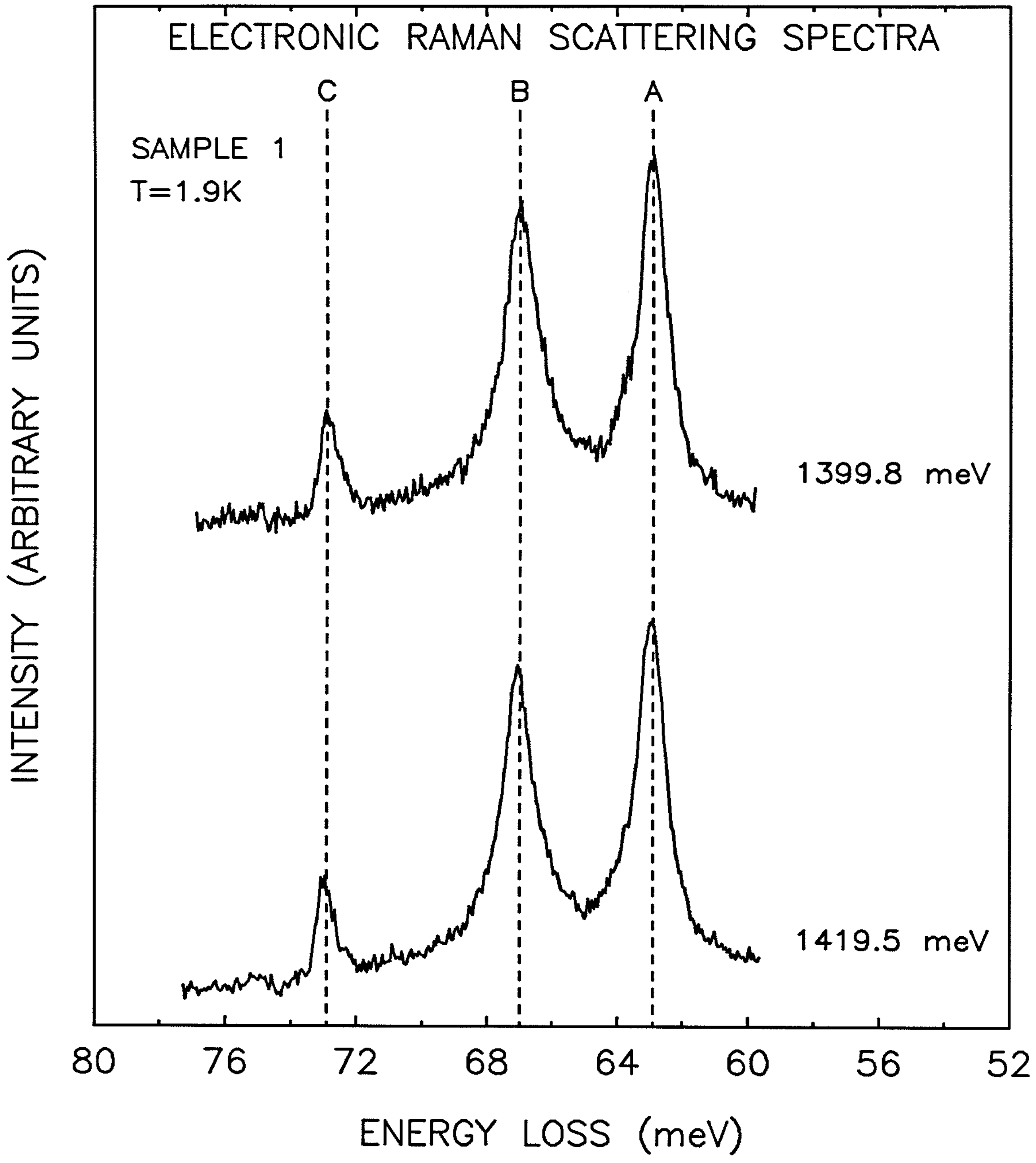

Figure 3.5: Electronic Raman scattering spectra from sample 1. Intensity of the emitted light is plotted against the difference between the emitted photon energy and that of the laser. Two different laser energies were used to distinguish between ERS features and background processes. The laser photon energy for each spectrum is at the right.

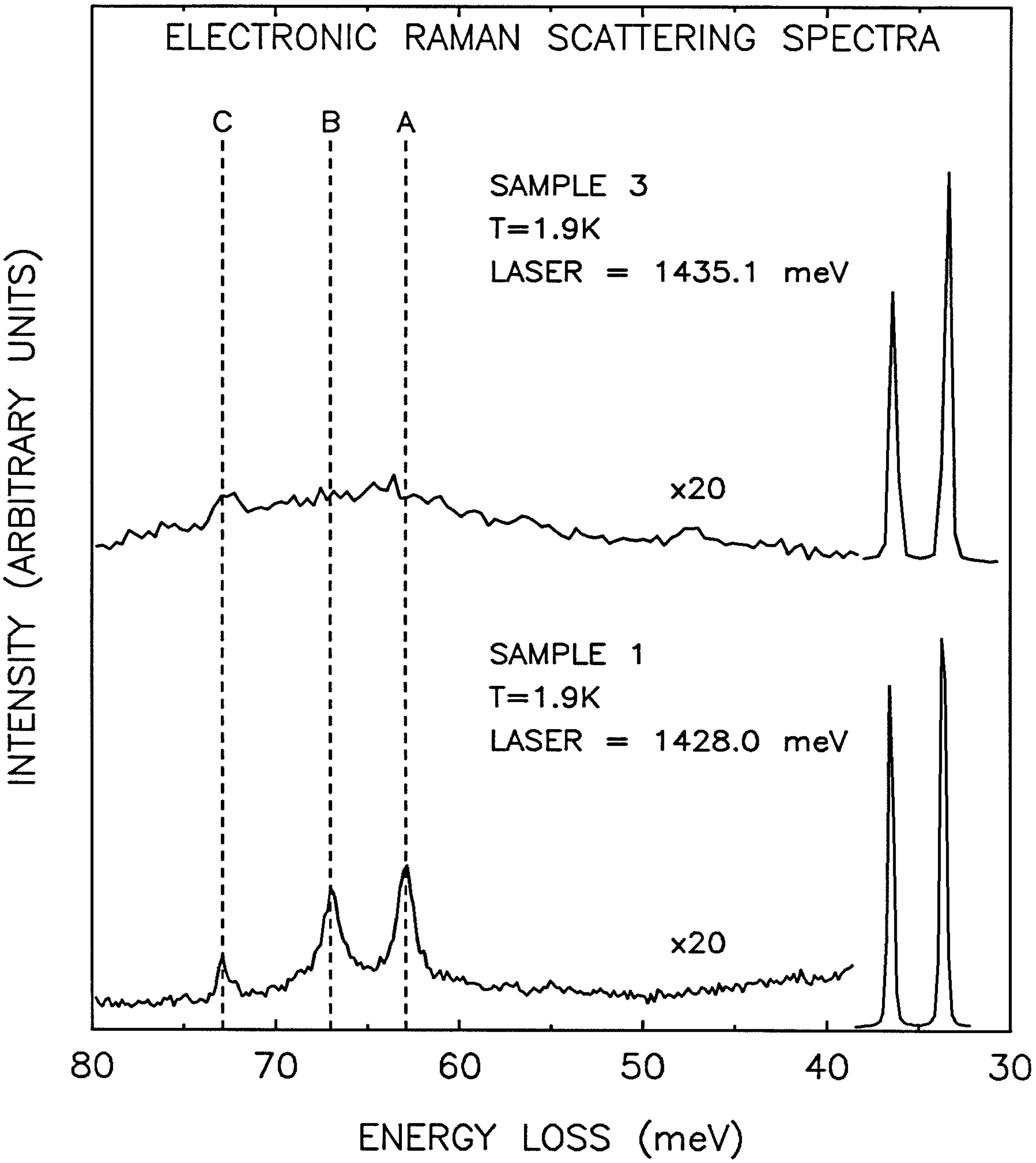

Figure 3.6: Electronic Raman scattering spectra from samples 1 and 3. Intensity of the emitted light is plotted against the difference between the emitted photon energy and that of the laser. Narrow lines at 36.5 and 33.6meV are due to Raman scattering from LO (Γ) and TO (Γ) phonons, respectively. The laser photon energy for each spectrum is given in the center.

that they both are due to the presence of the 78-meV acceptor. Although they lie in the energy region for two-phonon Raman scattering, we can be sure that they are electronic in nature since the excitation intensity in the SEL experiment is too low to observe even single-phonon Raman scattering. There is some evidence for a line at 73 meV in sample 3, which may be related to line C in sample 1. Since we do not observe line C in the SEL experiment, and it appears to be present in sample 3, it may be due to Raman scattering from 2 LO (Γ) phonons (room temperature Raman scattering measurments give a value of 72.9 meV for this transition[20]), and not related to the 78-meV acceptor. However, given the intensity of line C relative to the other two lines, it probably would not be visible above the background in the SEL experiment. Thus, the relationship between this line and the 78-meV acceptor is not firmly established by these experiments.

3.5 Interpretation

The results of both the SEL and ERS experiments indicate that lines A and B are both due to transitions from s-like excited states. The relative intensities of the two lines are nearly identical, while those due to s-like states are usually a factor of 5–10 times more intense than those of p-like excited states when observed by these techniques.[11,12] A single acceptor would not produce such an excited state spectrum. However, the $1s^1 2s^1$ (using atomic single particle notation) excited state of a double acceptor will be split into two s-like states by the exchange interaction between the two holes. This splitting might give rise to such a spectrum.

3.5.1 Double acceptor effective mass theory

A simple model of a double acceptor in a semiconductor can be obtained by analogy to the effective mass approximation. The holes are considered to be $j = 3/2$ particles, with mass equal to the heavy hole effective mass, m_h. The electric fields will be screened by the static dielectric constant. The acceptor can then be treated like a helium atom in a uniform dielectric medium. This will result in a two-fold splitting of the $1s^1 2s^1$ state to first order: a 10-fold degenerate $({}^3S, {}^7S)$ state, which is spatially anti-symmetric and has symmetric spins, and a 6-fold degenerate $({}^1S, {}^5S)$ state, which is spatially symmetric and has anti-symmetric spins. The energy of the splitting is given by

$$\Delta E = 2\langle 1:2s; 2:1s \left| \frac{e^2}{\epsilon \left|\mathbf{R}_2 - \mathbf{R}_1\right|} \right| 1:1s; 2:2s \rangle, \tag{3.6}$$

where ϵ is the static dielectric constant. This is just the exchange splitting due to the coulomb interaction between the two holes. For the purposes of this approximation, single acceptor hydrogenic wave functions can be used as a first-order approximation to this integral. In this case, the value for the splitting can be obtained by scaling the observed exchange splitting in helium. This is done by multiplying the energy for helium by the ratio of the Bohr radii divided by the static dielectric constant:

$$\Delta E_{semiconductor} = \frac{m_h}{m\epsilon^2}\Delta E_{He}. \tag{3.7}$$

The observed splitting in He is 0.79 eV,[21] which scales to 2.6 meV in GaAs. The data shows a splitting of 4.0 meV, which is in good agreement with the data. Including the effects of the crystal field and the spin-orbit interaction with the valence band will not change the splitting to first order, since they will affect the wave functions used, not the potential.

The energy level diagram for a double acceptor in GaAs is plotted in Fig. 3.7. The state assignments are given on the right, and the theoretical estimates of the hole binding energies relative to the valence band are given in the center column. The experimentally observed values for the binding energies are given in the left column. These values were obtained by subtracting the observed transition energies from the ground state energy (78 meV). Both of the experimental values for the $1s^2$ and $1s^*$ (the first and second ionization energies, respectively) states were determined by photoluminescence. While there has been some discussion as to whether the second ionization energy was 200 or 230 meV,[6,7] recent time resolved photoluminescence measurements favor 200 meV.[22] The values predicted by the simple effective mass model agree quite well with the observed values for the ionization energies, as well as with the $1s^1 2s^1$ states. This strongly indicates that the 78-meV acceptor is an effective mass double acceptor.

It is interesting to compare the calculated binding energies for the $1s^1 3s^1$ states to the observed value for line C. Line C occurs at 72.9 meV, while the average energy of the $1s^1 3s^1$ states is 72.5 meV. The theory predicts a splitting of only 0.6 meV between the two states, which would not be resolved in the ERS experiment. Thus it is possible that line C corresponds to the combination of

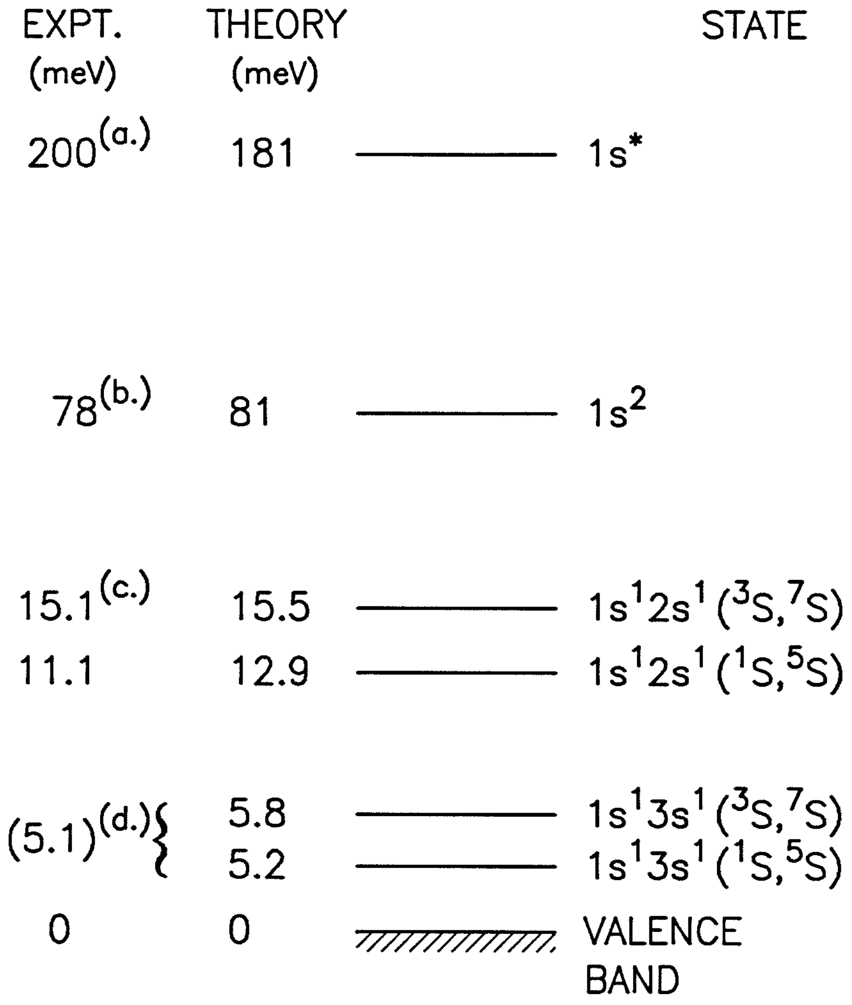

Figure 3.7: Energy level diagram for a double acceptor in GaAs (not drawn to scale). The state assignments are given in the column on the right. The values obtained from the double acceptor effective mass calculation are given under the theory column. The energies are binding energies measured relative to the valence band. The column on the left gives the experimental values.

a.) See Ref. 22.

b.) From photoluminescence measurements.

c.) Calculated by subtracting observed energies from the $1s^2$ energy (78 meV).

d.) This assignment is tentative — see the text.

both $1s^13s^1$ states. However, given the proximity of line C to the 2 LO (Γ) phonon Raman scattering line, and its absence in the SEL data, it is likely that line C is not related to the 78-meV acceptor.

3.5.2 Single acceptor model

The experimental results should also be compared with those expected for a single acceptor with a 78-meV ground state binding energy. In this case, the 78-meV line observed in photoluminescence would indicate a central cell shift of 52.3 meV (the effective mass binding energy for a single acceptor in GaAs is 25.7 meV).[23] The theory for shallow acceptors in semiconductors has been worked out in great detail by Baldereschi and Lipari.[23,24] The effect of the central cell shift must be included to correct the energy estimate for the $2S_{3/2}$ binding energy. The probability of finding the hole at the impurity site has been calculated in Ref. 24. Using the value $\mu = 0.767$ given there, the $2S_{3/2}$ state would experience a central-cell shift of 0.133 times that of the $1S_{3/2}$ state. Here that yields a shift of 7.0 meV for the $2S_{3/2}$ state binding energy. Reference 24 gives a value of 70.4 meV for the $1S_{3/2} \to 2S_{3/2}$ transition in GaAs, using 78 meV for the $1S_{3/2}$ binding energy. After adding the central cell correction, a value of 63.4 meV is obtained. The $1S_{3/2} \to 2P_{3/2}$ transition energy would be 66.6 meV. This would lead to the following assignments: line A could be the $1S_{3/2} \to 2S_{3/2}$ transition, and line B could be the $1S_{3/2} \to 2P_{3/2}$ transition of such a single acceptor. Line C could then correspond to the $1S_{3/2} \to 2P_{5/2}(\Gamma_7^-)$ transition, which should occur at 72.2 meV. While the observed energies seem to agree fairly well with this model, other evidence strongly favors the double acceptor model.

3.5.3 Comparison of theories

A comparison of the possible assignments is given in Table 3.1. As mentioned previously, both SEL and ERS are sensitive to transitions between *s*-like states. Given the nearly identical intensities for lines A and B, they must both be due to *s*-like states. If line C were due to the $1S_{3/2} \rightarrow 2P_{5/2}(\Gamma_7^-)$ transition, then the $1S_{3/2} \rightarrow 2P_{5/2}(\Gamma_8^-)$ transition should be visible at 70.95 meV, where it was observed in the IR absorption experiment,[4] since both SEL and ERS show *p*-like states with roughly the same intensity. Finally, IR absorption measurements heavily favor *p*-like states over *s*-like states, since the latter are forbidden to first order. Thus one would not expect to see *s*-like states in IR absorption. If line B were actually *p*-like, it should have been observed in the IR absorption experiment of Ref. 4. This leads to the conclusion that lines A and B are both *s*-like, and therefore that the 78-meV acceptor is a double acceptor.

3.6 Conclusion

This study represents the first observation of the *s*-like excited states of a double acceptor in a semiconductor. The observation of these states was made possible by the experimental techniques of selective excitation luminescence and electronic Raman scattering. These techniques should prove useful for identifying other double acceptors in semiconductors. This work also shows that the $1s^1 2s^1$ state of a double acceptor in a semiconductor is split by the exchange interaction between the two holes, and that the magnitude of the splitting is large enough to be observed by current techniques. This splitting provides a means of distinguishing single and double acceptors. The key to the identification is the determination of the symmetries of the excited states. SEL and ERS are both good techniques for observing *s*-like states, while infrared absorption can be used

Table 3.1: Observed line positions and interpretations.

	A	B	C[a]	ΔE[b]
SEL	62.5 meV	66.5 meV	···	4.0 meV
ERS	62.9 meV	66.9 meV	72.9 meV	4.0 meV
Double	62.5 meV	65.1 meV	72.5 meV[d]	2.6 meV
Acceptor[c]	$1s^2 \rightarrow 1s^1 2s^1$	$1s^2 \rightarrow 1s^1 2s^1$	$1s^2 \rightarrow 1s^1 3s^1$	
	$(^3S, {}^7S)$	$(^1S, {}^5S)$		
Single	63.4 meV[f]	66.6 meV	72.7 meV	3.2 meV
Acceptor[e]	$1S_{3/2} \rightarrow 2S_{3/2}$	$1S_{3/2} \rightarrow 2P_{3/2}$	$1S_{3/2} \rightarrow 2P_{5/2}(\Gamma_7^-)$	

a. The evidence suggests that line C is actually due to 2 LO (Γ) phonon Raman scattering and not related to the 78-meV acceptor. The assignments are included for reference to the text.

b. The energy separation of lines A and B.

c. Based on the effective mass like calculation discussed in the text.

d. This was obtained assuming that the experiment could not resolve the splitting between the two $1s^1 3s^1$ states. The value here is the average energy of the two states.

e. Based on the work done in Refs. 23 and 24.

f. This estimate was obtained by including the observed central cell shift of 78-meV.

to study *p*-like excited states. This study proved that 78-meV acceptor in GaAs is produced by the first ionization of an effective mass double acceptor. The line observed at 62.9 meV is due to the $1s^2 \rightarrow 1s^1 2s^1$ $(^3S, ^7S)$ transition, and the line at 66.9 meV line is due to the $1s^2 \rightarrow 1s^1 2s^1$ $(^1S, ^5S)$ transition. While the line at 72.9 meV may be due to the $1s^2 \rightarrow 1s^1 3s^1$ transition, there is also evidence supporting the assignment of this line to 2 LO (Γ) Raman scattering. It was difficult to make a positive identification of this line due to its low intensity and proximity to the multiple phonon Raman scattering processes in GaAs.

While it was shown that the center responsible for the 78-meV acceptor in GaAs is a double acceptor, the results of this study do not identify the source. Given the similarity of the observed levels to those predicted by the double acceptor effective mass theory, it may be reasonable to assume that the center is not very complex. If the center had very low symmetry, it probably would lead to further splitting of the highly degenerate $1s^1 2s^1$ states. Thus, the anti-site defect Ga_{As} is still a possible source for this acceptor.

Note added in proof

Recent work by Bishop et al.[22] has shown a that there is a connection between the 200-meV level observed in GaAs and the 78-meV level. They conclude that the 200-meV level is the second ionization of the 78-meV double acceptor. They believe that the 230-meV acceptor is due to a different center, and is a single acceptor. However, they were not able to identify the center responsible for the 78-meV acceptor.

Another interesting experiment has been performed on $Ga_{1-x}In_xAs$ by A. T. Hunter.[25] An acceptor at ~ 78-meV was observed in low (a few percent) In concentration $Ga_{1-x}In_xAs$ alloys. An ERS study of this acceptor showed two lines corresponding to lines A and B of this study. Alloy broadening of the lines was observed, indicating that they are indeed related to the 78-meV acceptor. (This is expected since there will be a distribution of possible sites for the 78-meV acceptor in the alloy, causing slight variations in the ground state binding energy.) A line similar to line C was also observed, but it did not exhibit broadening. This favors the identification of line C as 2 LO (Γ) phonon Raman scattering.

References

1. An excellent overview of GaAs growth techniques may be found in: H. Winston, *Solid State Technology* **26**, 145 (1983).
2. D. E. Holmes, R. T. Chen, K. R. Elliott and C. G. Kirkpatrick, *Appl. Phys. Lett.* **40**, 46 (1982).
3. P. W. Yu and D. C. Reynolds, *J. Appl. Phys.* **53**, 1263 (1982).
4. K. R. Elliott, D. E. Holmes, R. T. Chen and C. G. Kirkpatrick, *Appl. Phys. Lett.* **40**, 898 (1982).
5. A. T. Hunter, R. Baron, J. P. Baukus, H. Kimura, M. H. Young, H. Winston and O. J. Marsh, in *Semi-insulating III-V Materials*, Evain 1982, edited by S. Makram-Ebeid and B. Tuck (Shiva, Cheshire, England, 1982), p. 396.
6. P. W. Yu, W. C. Mitchel, M. C. Meir, S. S. Li and W. L. Wang, *Appl. Phys. Lett.* **41**, 532 (1982).
7. K. R. Elliott, *Appl. Phys. Lett.* **42**, 274 (1983).
8. R. A. Chapman, W. G. Hutchinson and T. L. Estle, *Phys. Rev. Lett.* **17**, 132 (1966).
9. H. Tews, H. Venghaus and P. J. Dean, *Phys. Rev.* **B19**, 5178 (1979).

10. P. J. Dean, D. J. Robbins and S. G. Bishop, *J. Phys. C* **12**, 5567 (1979).

11. A. T. Hunter, Ph. D. Thesis, California Institute of Technology, 1981.

12. A. T. Hunter and T. C. McGill, *Appl. Phys. Lett.* **40**, 169 (1982).

13. D. J. Ashen, P. J. Dean, D. T. J. Hurle, J. B. Mullin and A. M. White, *J. Phys. Chem. Solids* **36**, 1041 (1975).

14. W. Schairer and. T. O. Yep, *Solid State Commun.* **9**, 421 (1971).

15. The dye recipes used were:
DOTC - 250 ml DMSO, 750 ml ethylene glycol, 500 mg DOTC
HITC - 250 ml DMSO, 750 ml ethylene glycol, 500 mg HITC
Both of these dyes can now be replaced by Oxazine 750 using the following recipe:
625 mg Oxazine 750, 53 ml propylene glycol, 947 ml ethylene glycol.

16. See the Exciton Chemical Co. (Overlook Station, Dayton OH 45431) laser dye catalog and the references contained therein.

17. A. T. Hunter, M. H. Young and R. Baron, Hughes Research Laboratories (unpublished).

18. J. I. Pankove, *Optical Processes in Semiconductors* (Dover, New York, 1971), Appendix II, p. 412.

19. J. S. Blamkemore, *J. Appl. Phys.* **53**, R123 (1982).

20. T. Sekine, K. Uchinokura, and E. Matsuura, *J. Phys. Chem. Solids* **38**, 1091 (1977).

21. A. R. Strigonov and N. S. Sventitskii,*Tables of Spectral Lines of Neutral and Ionized Atoms* (IFI/Plenum, New York, 1968), Vol. I., p. 79.

22. S. G. Bishop, B. V. Shanabrook, and W. J. Moore, *J. Appl. Phys.* **56**, 1785 (1984).

23. A. Baldereschi and N. O. Lipari, *Phys. Rev.* **B9**, 1525 (1974).

24. A. Baldereschi and N. O. Lipari, *Phys. Rev.* **B8**, 2697 (1973).

25. A. T. Hunter, Hughes Research Laboratories, private communication.

Appendix A

Photoluminescence using an FTIR

A.1 Introduction

The majority of photoluminescence measurements on semiconductors are performed using dispersive spectrometers to analyze the wavelength dependence of the signal. Dispersive spectrometers are best suited to operation in the visible and near infrared regions. There is a wide variety of sensitive detectors available in this wavelength range, allowing good signal-to-noise ratios to be obtained in fairly short accumulation times. However, dispersive spectrometers are not well suited to studies of broad wavelength ranges in the mid- to far-infrared. The detectors available for the range beyond $10\,\mu$m are not very sensitive (see Table 2.1 on page 21), necessitating long integration times. Grating efficiency also poses a problem. While gratings can approach 90% efficiency near the blaze wavelength, the efficiency can drop dramatically toward shorter and longer wavelengths. The usual remedy for this problem is to have a number of different gratings for each wavelength range to be studied. This problem is exacerbated in optical studies of semiconductors by the inverse dependence of the wavelength of light on energy. Thus at small energies, a small shift in absolute energy results in a large shift in wavelength in the infrared. The study of even a small energy range requires the ability to cover a large wavelength range. Finally, there is a tradeoff between throughput and resolution in a dispersive spectrometer. This makes high-resolution studies over large wavelength ranges difficult with a dispersive spectrometer. A Fourier transform infrared spectrophotometer (FTIR) is an instrument which can overcome many of these problems. However, a standard FTIR is not well suited for studying weak externally generated signals in the $10\,\mu$m range, due to the presence of a large background of 300 K blackbody radiation. This appendix is a description of a novel technique for performing photoluminescence with an FTIR, which overcomes the problems associated with background blackbody radiation.

A.2 FTIR principles

There is a wealth of information in the literature describing the theory and operation of FTIRs,[1] and the details will not be discussed here. An FTIR basically operates as a Michelson interferometer (see Fig. A.1). Either light from an internal source, or external light entering through a viewport, is directed onto a beam splitter. One beam is directed onto a fixed mirror, which returns it to the beamsplitter and onto the detector. The second beam strikes a moving mirror, and is directed back to the beamsplitter and onto the detector as well. The intensity of the light falling on the detector is modulated at a frequency dependent upon both the wavelength of the incident light and the speed of the moving mirror. The signal out of the detector represents the Fourier transform of the input signal. The signal is then amplified, filtered, and sent to an analog-

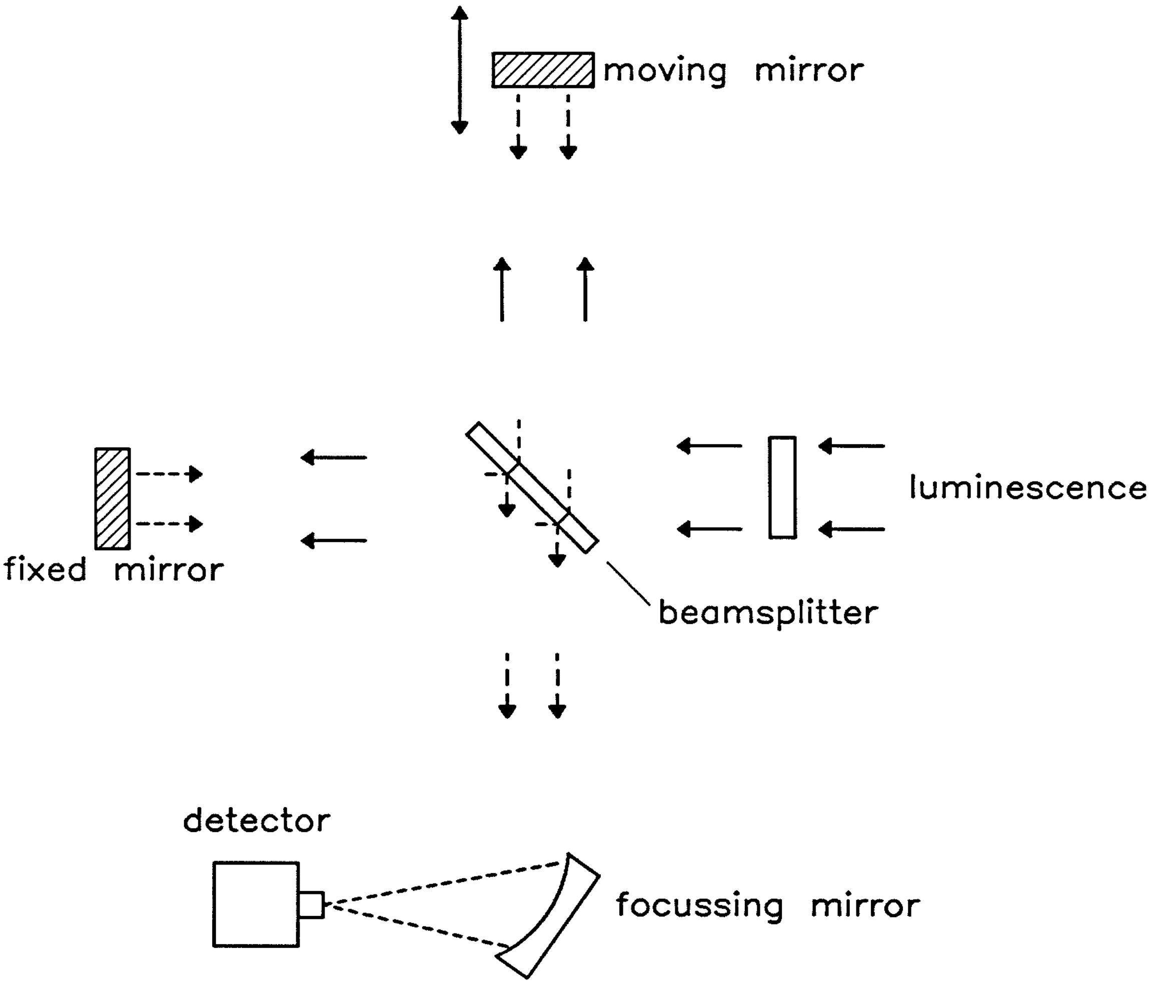

Figure A.1: Schematic diagram of a Fourier transform infrared spectrophotometer.

to-digital converter and on to a vector processor. The vector processor takes the Fourier transform of the signal, and sends it on to a computer for analysis.

The advantage of using an FTIR instrument for studying signals in the infrared comes from its ability to collect light over a broad spectral region in a short time period, and allowing nearly all the light from the source to be incident on the detector throughout the scan. As discussed in Chapter 2, the signal-to-noise ratios of most solid state detectors used in the infrared increase as the signal strength increases. Since dispersive instruments trade off the signal strength falling on the detector for resolution, they suffer from lower signal to noise ratios than FTIR instruments. These advantages are usually used for performing infrared transmission measurements. For such measurements, an internal broadband source is directed onto the beam splitter. The sample is placed just before the detector, transmitting the modulated light as a function of wavelength. A high-pass filter on the detector output removes any d.c. components of the signal. This eliminates any unmodulated light from appearing as a signal after the Fourier transform is performed. The output will then show the transmission of the sample as a function of wavelength, but no signal from the blackbody radiation of the spectrometer housing or the sample. While this makes the FTIR well suited for transmission experiments, experiments involving external sources are more complicated.

A.3 Photoluminescence measurements with an FTIR

Blackbody background

When analyzing photoluminescence, or any an external signal, the presence of 300 K blackbody radiation poses a real problem, since the FTIR will modulate all the light incident on the beamsplitter. When using the external viewport, the beamsplitter will "see" the entire optical path, including the external viewport. While the optics may be transparent in the infrared, they are also sources of infrared radiation since they are at room temperature. This large thermal signal can easily mask the weak signals generated by photoluminescence measurements. While cooling the optics might limit this problem, it would be very impractical. In regions where the background blackbody signal is fairly weak, $\lesssim 3\,\mu$m in the near infrared and $\gtrsim 30\,\mu$m in the far infrared, simple digital subtraction of the background signal may be sufficient to observe external signals. Digital subtraction involves subtracting a background scan (where the signal of interest is absent) from the signal scan. This subtraction is performed after digitization, but before the Fourier transform is performed. This technique is less than ideal — the background signal may change during a long scan; it is limited by the resolution of the digitization, and a large change in the signal strength falling on the detector between the scans might change the detector response characteristics. These problems confine this technique to regions where the signal is fairly strong relative to the background. The solution arrived at for the HgTe-CdTe study in Chapter 2 of this thesis allows the detection of very weak signals obscured by a large background, and is much more sensitive than digital subtraction.

A.3.1 Double-modulation technique

This section describes a double-modulation technique used to convert the desired emission signal from d.c. to a relatively high frequency a.c. signal. When using a dispersive spectrometer in the presence of a large background, the usual method for the detection of weak signals is to modulate the signal of interest to an a.c. frequency. This allows for synchronous detection of the emission signal, and lowers the 1/f-noise added to the signal by the detector. There are a number of considerations when adapting this technique to FTIR spectroscopy. The FTIR itself modulates the external signal to a set of a.c. frequencies, where the frequency depends on the wavelength of the light. This waveform must be preserved if the vector processor is to produce the correct Fourier transform of the signal. This requires modulating the signal before it enters the spectrometer, and demodulating the signal just before the analog-to-digital converter. The basic setup is shown in Fig. A.2. The system must be designed to block all the fundamental FTIR frequencies, since these will correspond to the unwanted unmodulated external signal. Therefore, the external modulation frequency should be greater than the highest frequency produced by the FTIR to allow for filtering. It is best to use as high a modulation frequency as the system will allow, since this will ensure differentiation between the doubly-modulated signal and the singly-modulated background signal, and narrow the bandwidth of the doubly-modulated signal.

As shown in Fig. A.2, the photoluminescence is modulated by a pulsed laser source. It is also possible to use a mechanical beam chopper to modulate the luminescence, but pulsed lasers can operate at much higher frequencies. The luminescence is collected by a set of infrared optics. The collection lens is chosen to match the f-number of the output window on the dewar, and the transfer lens is chosen to match the input f-number of the FTIR. A Ge filter may be placed before the FTIR external viewport to prevent specularly scattered laser light from entering the spectrometer. It is possible that the intense laser light could change the properties of the detector; therefore, it should be blocked. A solid state infrared detector is used (Ge:Zn was used in Chapter 2). The output from the detector is amplified, and sent to a filter. The filter is designed to remove the strong, singly-modulated background signal which could overload the following amplifier stages or the mixer. This filter consists of a high-pass or band-pass

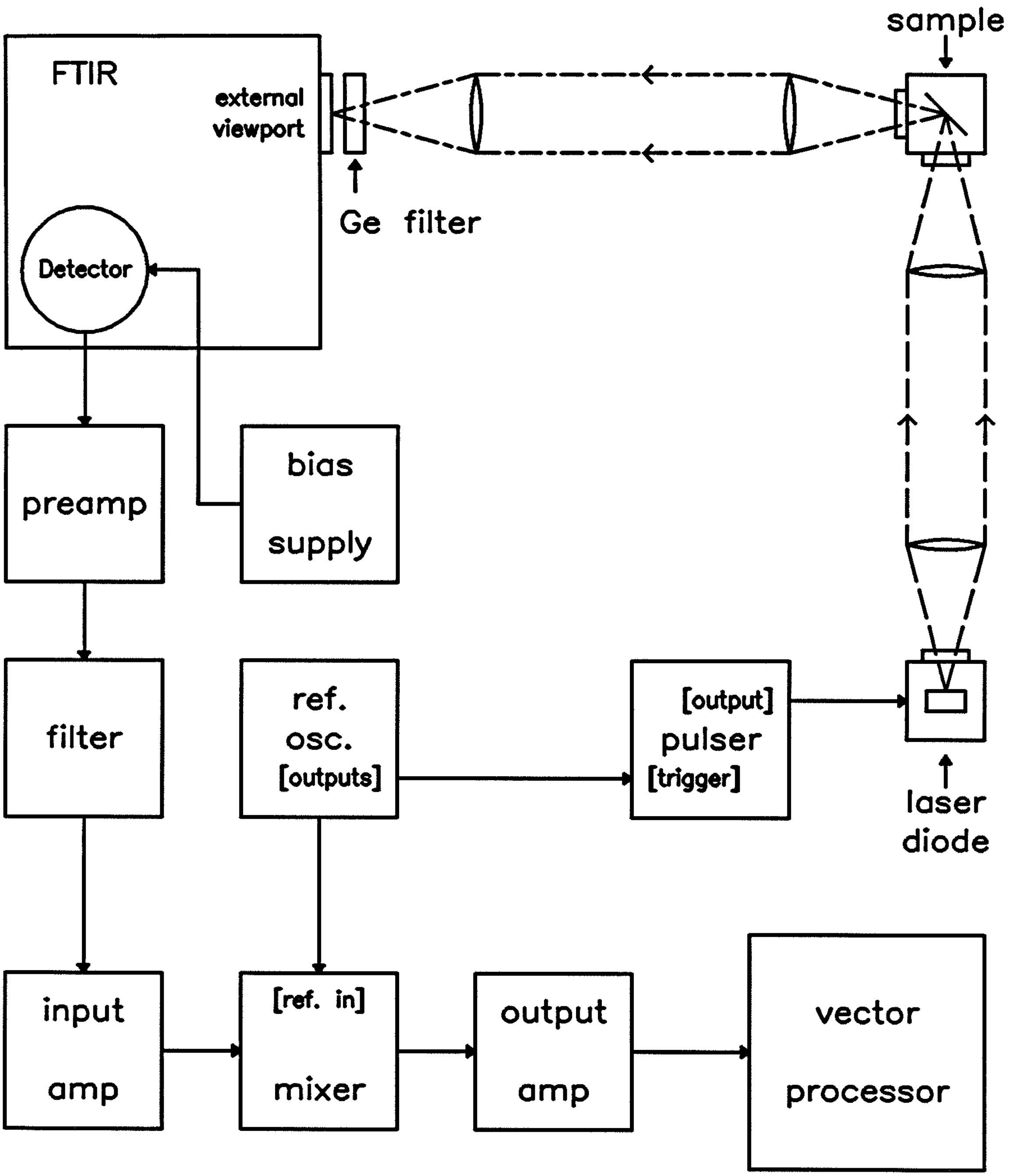

Figure A.2: Schematic diagram of the FTIR experimental setup.

filter, set to pass the bandwidth of the doubly-modulated signal. The filtered signal is then amplified more, since it now consists of only the weak doubly-modulated signal, and sent to a mixer for demodulation. The demodulated signal is amplified so that the maximum signal strength corresponds to the full scale input of the analog-to-digital converter. The signal now appears as if it had only the spectrophotometer modulation and can then be fed into the standard signal processing electronics of the FTIR. The end result is the elimination of the background blackbody signal. Figure A.3 shows two photoluminescence spectra of a $Hg_{1-x}Cd_xTe$ alloy sample, one taken using the double-modulation technique, and one taken using only the instrument's standard electronics. The lower trace (double-modulation setup) shows a broad doublet structure, corresponding to luminescence from near the band gap of this sample. The upper trace (non-modulated) shows a wide continuum characteristic of 300 K blackbody radiation dominating the signal from the sample. The peak intensity of the upper trace is about 200 times that of the lower trace. The photoluminescence signal could not be observed, even by digitally subtracting a background scan from the upper scan. This figure illustrates that a large improvement in the signal-to-noise ratio can be obtained even for very small signals by using this technique.

A.3.2 Actual experimental setup

The actual experimental setup was based on a PAR model 124A lock-in amplifier, which contained the mixer, an input preamplifier, an input filter and an output amplifier. This system worked quite well, and the full-scale output of the lock-in matched the full-scale input of the analog-to-digital converter. A schematic diagram of the actual system setup is shown in Fig. 2.3 on page 30. The actual settings used for the experiment are described in Section 2.3.4. The input high-pass filter frequency and Q were chosen to provide the maximum fil-

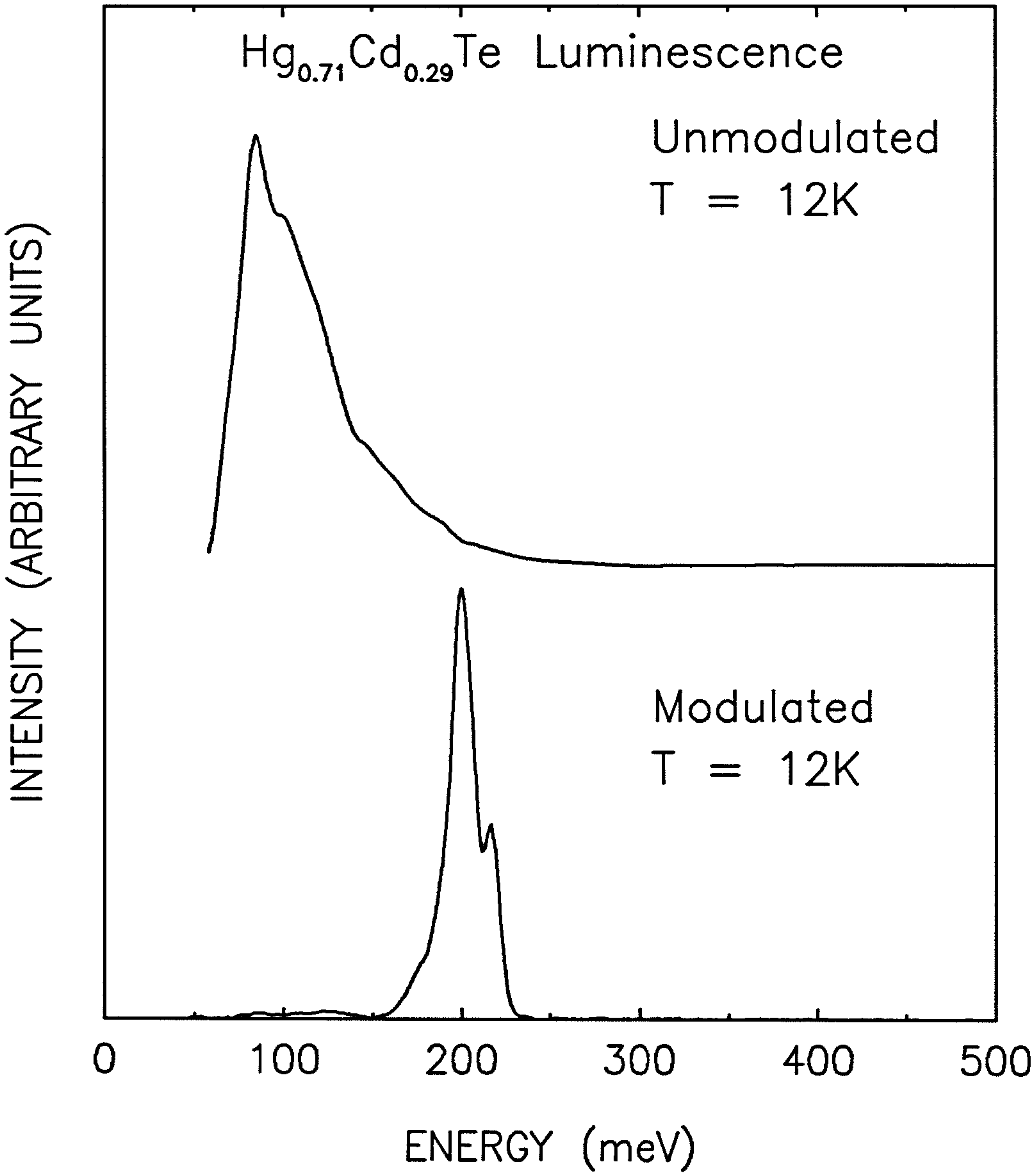

Figure A.3: A comparison of the two FTIR measurement techniques. Both scans are measurements of the photoluminesence spectrum of a $Hg_{1-x}Cd_xTe$ alloy sample. The conditions of each measurement are identical, except for the measurement scheme. The upper scan is a conventional FTIR scan, while the lower scan was obtained using the double-modulation scheme described in the text. The vertical signal on the lower trace is roughly 200 times that of the upper trace.

tering of the singly-modulated signal without introducing phase shifts into the signal. Unfortunately, this necessitated using a fairly low filter frequency, and a low Q, which provided a relatively shallow rolloff. A filter with a sharper turnoff would probably have improved the signal-to-noise ratio. The lock-in amplifier mixer had an output time constant, which was set to the minimum value of about 600 μs, causing attenuation of freqencies above 265 Hz. This output low-pass filtering turned out to be useful. While the time constant limited the data collection speed (the FTIR modulation frequencies are determined by the speed of the moving mirror), using the direct mixer output and higher mirror speeds resulted in a lower signal-to-noise ratio. This effect was not expected, but may be due to high-frequency noise in the electronics.

A.4 Possible pitfalls

There are a few possible problems associated with the FTIR double modulation technique. Given the high modulation frequencies used (40 kHz was used for the study in Chapter 2), obtaining a system response curve is fairly difficult due to the shortage of broadband infrared sources which can be modulated to such high frequencies. The attenuation due to the electronic filtering can be measured or estimated, but the optical response is difficult to determine. The response of components such as the beam splitter and optics can be measured without resorting to double modulation, but the response of solid-state infrared detectors is a function of the modulation frequency of the incident radiation. This effect can not be measured in an easy manner using this setup. Therefore, one must take care analyzing the output, since there may be some system response effects. The photoluminescence spectra of $Hg_{1-x}Cd_xTe$ alloys taken with the doubly-modulated FTIR setup was compared with luminescence of similar samples taken with a dispersive spectrometer, and no large system response effects were noticed.

This system is very sensitive to any signal modulated at the reference frequency. When performing photoluminescence experiments in the infrared, the sample is frequently placed on a cold finger in a vacuum, since many infrared optical materials can not withstand the thermal expansion and temperature shock present in immersion dewars. Vacuum is a very poor heat conductor, therefore it is possible to heat up a sample very rapidly with only modest laser powers, if the sample is not mounted well. With poor mounting, samples were observed to heat up from 12 K to over room temperature in less than 2 minutes for 200 mW average incident power. However, even if the sample is mounted fairly well, it is possible to modulate the temperature of the sample slightly at the laser frequency. This temperature change could show up either as a change in the blackbody radiation, or a change in the luminescence of the sample. It is also possible to modulate the reflectivity of a sample (see Section 2.3.5). In this case, the sample will reflect room temperature blackbody radiation into the FTIR, modulated at the laser frequency. This effect was observed, although the actual process responsible for the change in reflectivity was not identified; it was probably due to changes in the carrier concentration.

In conclusion, a novel double-modulation technique has been developed for performing photoluminescence using a Fourier transform infrared spectrophotometer in the presence of a large background signal. This technique produces a dramatic improvement in the signal-to-noise ratio for weak signals over standard FTIR experiments. The technique allows the advantages of FTIR spectrometers over dispersive spectrometers for emission experiments to be used in previously inaccessible wavelength regions. The resulting system is much more sensitive than conventional dispersive spectrometers over a wide wavelength range, so sensitive that photoluminescence from $Hg_{1-x}Cd_xTe$ alloys with Cd concentrations of ~ 30% was observed at room temperature. A standard system based on a dispersive spectrometer was limited to sample temperatures below 60 K. This technique should find wide applications studying infrared emissions from a variety of sources.

References

1. There are many good references on the principles of Fourier transform infrared spectroscopy. The following is a partial list of sources, but it should provide a good starting point.

    - W. Demtröder, in *Laser Spectroscopy* (Springer-Verlag, Berlin, 1982) pp. 139–190.
    - R. C. Milward, in *Far-infrared Properties of Solids* (Plenum, New York, 1970) pp. 1–34.
    - R. G. Bell, *Introductory Fourier Transform Spectroscopy* (Academic Press, New York, 1972).
    - J. Chamberlain, *The Principles of Interferometric Spectroscopy* (John Wiley and Sons, New York, 1979).